Design and Fabrication of Origami Elements for use in a Folding Robot Structure

By
Akeel Abdulkareem Abtan

Submitted in accordance with the requirements for the degree of
Doctor of Philosophy

The University of Leeds
Institute of Design, Robotics and Optimisation
School of Mechanical Engineering

July, 2019

The candidate confirms that the work submitted is his own and that appropriate credit has been given where reference has been made to the work of others.

Acknowledgements

I would like to thank my supervisors, Professor Robert Richardson and Dr. Briony Thomas for their support, guidance, and encouragement during the research and preparation of this thesis. I am deeply grateful to Tony Wiese for his invaluable support and advice during this work.

I am deeply indebted to Graham Brown and Rhys Moore for their support and for always being on hand for their skills with 3D printing. I would like to express my gratitude to all members of the School of Mechanical Engineering who aided my course of study.

I must here express my deep thanks and appreciation to my sponsor (The Ministry of Higher Education and Scientific research in Iraq) and the Department of Electromechanical Engineering, the University of Technology, for granting the opportunity to do my PhD at the University of Leeds. A special word of thanks is given to all members of the Iraqi Cultural Attache for their support during my study.

I would like to thank my family for their support especially my wife Alyaa Alrubaye who worked so hard with a lot of patience to take care of me and the family. It is truly a blessing to be surrounded by a loving and supportive family that never ceases to believe in you even when you start to doubt yourself.

Furthermore, I would like to thank all the friends I made throughout my period of study; especially, Aimen Zeiny, and Karrar Al-Dirawi, for making these years so memorable.

Abstract

The aim of the research is to investigate the methodology of the design and fabrication of folding robots that depend on the origami structures. The use of origami structures as a foundation to build reconfigurable and morphing robots that could assist in search and rescue (SAR) tasks are investigated. The design of the origami folding structures divided into three stages: consideration of the geometry of the origami structure, the hinge design, and the actuation system.

The result of investigating three origami structures shows the ability to use the unit cell of the origami ball structure as a self-folding element. Furthermore, the novel type of origami structure for manipulation was created according to this result. This novel structure was designed to be a soft manipulation robot arm.

Two approaches are used to design and fabricate flexure hinge. The first is by using a 3D printed multi-material technique. By this technique, the hinge printed using soft and solid material at the same time, which is Tango plus flx930 for soft material and Vero for solid material. The soft material act as a flexure hinge. Therefore, three tests were operated for it to calculate the tensile force, fatigue limit, and the required bend force. The second approach is by using acrylic and Kapton materials.

Two types of actuation systems were studied: the external actuation system and embedded actuation system. The external actuation system was used for the Origami structure for manipulation, while the embedded actuation system was used for the self-folding structure. The shape memory alloy wires in torsion (TSW) and bending (BSW) was used in an embedded actuation system.

A unit cell of origami ball was fabricated as a self-folding element by using three approaches: manually, acrylic, and Kapton and 3D printing. It is actuated by using shape memory alloy wire. Furthermore, an origami structure for manipulation was fabricated and actuated using an external actuation system. This novel type of origami structure provided an excellent bend motion ability.

Table of Contents

List of Tables

List of Figures

List of Abbreviations

SAR	Search and rescue
USAR	Urban search and rescue
UHMwPE	Ultra-High molecular weight polyethylene
SMP	Smart memory polymers
SMA	Shape memory alloys
NiTi	Nickel titanium
SMW	Shape memory wires
BSW	Bending Shape memory wires
TSW	Torsion Shape memory wires
OSM	Origami Structure for manipulation
DOF	Degree of freedom
FEA	Finite element analysis

Chapter 1 INTRODUCTION

1.1 Introduction

Robots take their place in many aspects of modern life. They can be found in manufacturing, education, medicine, and many other fields. The major advantage that robots can offer is the ability to accomplish tasks that could not be achieved by humans. One example of these tasks is the exploration task. Many exploration tasks required a robotic assistant. Some of these tasks have very small and limited access. These tasks require operating robots with less damage to access. There are two examples of these situations which are the search and rescue of people from collapsed buildings and the surgery for difficult places in the body.

The idea of using the robots in search and rescue tasks was proposed in 1980, but the search and rescue robots (SAR) were not used practically until the 11 September terrorist attack on the World Trade Centre. This regrettable event provided an opportunity to test the urban search and rescue robots (USAR) in real rubble piles [1]. It seems that using (USAR) robots decrease the civilian casualties with less effort.

However, the using of (USAR) robots practically reveals issues in the robot platform. The common challenges facing the robots are the limited access and risks of these accesses. These obstacles happened because most buildings are constructed of bricks and concrete, and these materials can turn into grains when they crash. Therefore, sometimes the rubble piles of these buildings are not providing an appropriate access for (USAR) robot. Moreover, these accesses are risky because they can collapse when the robot hits an unexpected obstacle. These causes lead to thinking about using the minimally invasive technique for the above situation.

The minimally invasive technique is the procedure of using a robot with small size to reduce or element any damage that can happen due to the operation of the task. The size of the robot is the main issue that will facing the researchers

when they design a robot according to minimally invasive technique. The problem is the size of the robot should be small enough to be inserted from a narrow access, and it should have an appropriate size for locomotion system. This situation leads to thinking of morphing structure which can reconfigurable and change its structure from small size to a big size. Some researchers design small units that could connect to configuration a big size shape of a robot. These robots are known as a modular robot [2]. Another solution is building a three-dimensional structure from the two-dimensional sheet by using the folding technique.

In the last few years, some researchers consider the origami robots and self-folding sheet to be potential solutions for the applications that require a morphing structure [3], [4]. The ambition of these researchers is to reach the design of a robot with a high degree of freedom which is simple manufacturing and inexpensive. In addition, it can be self-folding, and self-assembly and it can be used to operate a minimally invasion task because it is folded from a 2D sheet into a 3D structure.

Origami is a Japanese word that continued two sections “ori” meaning folding and “kami” meaning paper, which is mean the art of paper folding. Origami fabrication is an important design principle in nature [5]. For example, flowers and leaves of many plants are folded within the bud, insect wings often exhibit a folded morphology inside the cocoons and carapaces [6], and the function of many proteins is dependent on the way they fold from chains of amino acids [7]. In engineering, origami is associated with folding processes in which a structure is created from a sequence of spatially organized folds, similar to an umbrella. The concept of origami can also be explored as a design tool in engineering. Starting with a single sheet of paper or even a linear string, complex 3D objects with distinct mechanical properties can be constructed by folding.

Therefore, concepts borrowed from the art of origami and from nature can be applied to create a new type of robots called origami robots. Origami robots are autonomous machines, whose shape and function are created by folding. Their bodies are made of several dynamic folds that perform together to actuate the machine. The origami robot is made of a single planar sheet that is folded into a complex 3D structure. Origami robots have built- in compliance because of the geometry of the folds and the creases in the material, and they are semi-soft, that is, they exhibit the properties of both rigid and soft robots [8]. At the same time, rigid structures and spatial linkage mechanisms can be created owing to the tiling structure and origami folding pattern.

The origami approach to making robots can be considered a top-down approach. This is in contrast to the conventional bottom-up approach for making robots, that is, independent components such as nuts and bolts are manually assembled in an incremental way, requiring time, effort and expertise. Origami robots provide an opportunity to simplify and accelerate the design and fabrication of robots. However, fabrication of origami robots has several technique issues starting from the origami structure, the type of material used, to the actuation system. Until now there is no clear vision about origami structure behaviour and many research still study various kinds of origami structures. Most of the origami robots are made from paper or card papers reinforcement with a layer from other material. There are some origami robots fabricated using plastic or other rubber-like material but the researchers still looking for a suitable material that could replace the paper in the origami robot.

1.2 Motivation

The motivation for this research is to undertake research and development into fabrication approaches of origami structure. Fabrication the robots by using the origami-inspired structures is a simplified method for the design and fabrication of complex mechanisms that are required to build complicated reconfiguration robots. Origami-inspired fabrication approaches have the potential to enable novel prompt fabrication and customization of robots.

Origami robots have many advantages compared with traditional robots, including the ability to achieve autonomous locomotion, manipulation, and performance by morphing the shape of their structures, by actuating continuously along with their bodies and by deforming to adapt their bodies to the task and environment. Origami robots can change their shape to specific tasks and environments, and achieve agility of motion by using folding, unfolding and new folding technique. Origami robots can be fabricated from a variety of materials (for example, plastics, metal, and paper).

This thesis discusses the approaches of fabrication origami robots to put a clear path that could be followed to analysis and experimentation origami shape design, materials, and actuators that used to fabricate origami robots.

1.3 Aim and objectives

The overall aim of this study is to undertake research into the methodology of the design of folding robots that could simplify fabrication and actuation using modern fabrication approaches. To fulfil the project aim, the following objectives should be achieved:

1. Explore the geometry of origami structures and their ability to carry out operating tasks.
2. Explore the material properties of 3D printed structures to find suitable structures and materials for create fluctuation hinges.
3. Investigate actuation systems for folding structures.
4. Explore the behaviour of the Shape Memory Alloy (SMA) actuators.
5. Design and fabricate an origami robot arm.

1.4 Statement of Contribution

The main areas of original work carried out during this research are highlighted below.

1. Investigated 3D printed fluctuation hinges that was fabricated using 3D printing with multi-materials, and found that the material Tango Plus FLX930 is a suitable hinge material.
2. Investigated the behaviour of the shape memory alloy (SMA) actuators and calculate their ability and limitations.
3. Designed and fabricated a novel type of origami robot arm.

1.5 Published Documents (Appendix A)

Abtan, A. A., Richardson, R. C., & Thomas, B. (2016, October). Analyzing the 3D printed material Tango plus FLX930 for using in self-folding structure. In 2016 International Conference for Students on Applied Engineering (ICSAE) (pp. 114-118). IEEE.

1.6 Structure of Thesis

The main body of this thesis consists of seven chapters. A breakdown of each chapter is given below.

Chapter 1: Introduction

This chapter describes the background, aim & objectives and methodology of the research.

Chapter 2: Literature review

This chapter reviews research into the applications of robot such as exploration and search and rescue robots to address the points that could be improved when using folding robots. Furthermore, the chapter reviews the research into self-folding and origami robots to obtain further understanding to the design and fabrication technique that are used for creating these robots.

Chapter 3: Geometry

In this chapter the origami structure is described and explained. And some types of origami structures are analyzed, and the ability to use in mechanical engineering is discussed. In addition, the geometric parameters and mathematical models are defined for these origami structures. The chapter also contains some practical examples of origami structures. The differences between these origami structures are explained in this chapter. The self-folding ability is described with the ability of locomotion. Furthermore, a novel type of origami structure for manipulation is illustrated.

Chapter 4: Hinge Design

In this chapter, the behaviour of the hinge is analysed and the parameters that affect the folding structures during the folding process are calculated. A 3D printed soft material is tested for use as a hinge material and the results are discussed. In addition, the hinge in folding structures fabrication by laser cutting is described. Finally, the properties of the Kapton film material, which it is used as a hinge in the folding structures fabrication , are compared with the other approaches.

Chapter 5: Actuation

In this chapter, the external actuation is described and two types of force transmission tools are analysed, force transmission using string, and force transmission using 3D printed materials. After that, the embedded actuation is described. The smart materials are investigated and the shape memory wire actuators are examined and tested.

Chapter 6: Design and fabrication folding structure

In this chapter, the fabrication of self-folding samples by using three different methods and materials are illustrated. The fabrication of OSM-Bot is demonstrating in this chapter. Furthermore, OSM-Bot behaviour and motions are examined, and the results are shown.

Chapter 7: Conclusion and Future work

This chapter presents and discusses the five research objectives were outlined in section 1.3 and identifies the extent to which they have been fulfilled during this study. And summarised the conclusions and future work of design and fabrication the origami folding robots.

Chapter 2 LITERATURE REVIEW

2.1 Introduction

The design and fabrication of the folding robots require to study and review of the origami structures. The study contains the modelling, the algorithm, and the computational design of origami structures during the last decades to make a clear view of the development of origami. Furthermore, it is important to understand the ability to fabricate these origami structures and the approaches that were used for fabrication them. It is also important to review existing work on the fabrication of the folding robot to understand how other researches have chosen the materials and the actuators that built these folding robots, and the reason behind these selections. But the first point is to study the application fields that can use folding robots and compare the traditional robots that were used in these applications with the folding structures. The applications such as search and rescue; minimally invasive technique and exploration are the most fields that can make huge progress when using folding robots in their applications.

In this chapter, the traditional exploration and search and rescue robots are presented with the explanation of the development for these robots. Furthermore, the two recently robotics types that use in exploration and search and rescue fields are investigated which are the modular robots and the snake robot. After that, the technique of minimally invasive is explained with some examples. Folding robots are discussed in section 2.3 and research on self-folding structures with the novel actuators, which are used in a self-folding structure, are demonstrated. Finally, there is a brief conclusion.

2.2 Exploration and Search and Rescue Robots

The first practical use of robotics in search and rescue operation was during the 11 September which was the World Trade Centre disaster. In that event, many types of rescue robots were used to search for victims such as the PackBot from I-Robot, Solem, and Talon from Foster-Miller and Micro VGTV from Inuktun [9], see Figure 2.1. All these robots are a tracking robot that can move with a suitable average speed, but the main issues are the size and weight, especially when the task required to insert the robot from a small void in a rubble with the concern of the secondary collapses. Table 2.1 shows the size and weight of some rescue robots [10]. From the table, you can see that the smallest one is the Micro VGTV robot, and it can adjust its height from 25.39 to 6.35 cm, but that lead to extending its length from 19 to 31.75 cm [11]. Therefore, the extending in length, which causes by reaching the appropriate height for the access, makes the avoidance of obstacles more difficult.

(a) (b) (c)

Figure 2.1 Types of some rescue robots that used in the World Trade Centre disaster (a) The iRobot Packbot. (b) Foster–Miller Solem. (c) Inuktun MicroVGTV [9].

Table 2.1 The size, weight and speed of some rescue robots.

Robot Type	Length (cm)	Width (cm)	Height (cm)	Weight (Kg)	Speed (m/Sec)
Packbot	68.6-88.9	40.6-52.1	17.8	18	2.5
MicroVGTV	19-31.75	16.5	6.35-25.39	4.5	0.076
Solem	50	35.5	20.3	15	0.5
Talon	86.4	57.2	27.9	15	2.2

The researchers, Who develop these kinds of robots, recommend that using these tracked robots in outdoor missions such as exploration, searching and bombs treatment. For example, The Packbot was used to search for the chemical and nuclear weapons in Iraq [12]. Furthermore, the Telerob company produces two tracked robots that are used for bombs treatment. These robots are called the EOD and the telemax which have dimensions similar to the Packbot dimensions [13].

Moosavian divides the search and rescue robots into three major categories according to its locomotion system which are wheeled, tracked, and legged robots. He fabricated a mobile robot with a tracked locomotion system and called it Resquake [14]. He presented this robot as a search and rescue robot, but Resquake still have the same issues of tracked robots which are the size and weight. Its dimensions are 41-80 cm length, 40 cm width, and 26 cm height, and its weight is 25 Kg.

The limitations of traditional rescue robots make many researchers trying to create a new approach to designing these robots. Researchers start to notice the issues of these robots and developed a new design to overcome these issues. Many researchers maintain that the tracked and wheeled locomotion systems are not appropriate for rescue environment and they propose that the new design of rescue robot should have a new type of locomotion system inspired from the nature such as the locomotion of snake or worm. However, other researchers believe that the rescue task required a high manoeuvrable robot, and the major issue of the traditional rescue robots is the rigidity. In the other side, some researchers declare that to enhance the performance of rescue robots, Its locomotion system should be developed and make it a reconfigurable robot. These opinions lead to many suggestion designs for search and rescue

robots such as modular robots, snake robots, and legged robot. In the following, all these types are discussed.

2.2.1 Modular Robots

The modular self-reconfigurable robot is a composed of many robotic modules that can be connected to form a robot which can autonomously change its shape and functionality. Therefore, self-reconfigurable robots are more versatile comparing with other non-self-reconfigurable robot. It can change its shape to configuration a snake-like robot, a Hexapod robot and more different forms with different locomotion style. This flexibility is very suitable for the robotic system used in rescue operations [15].

Modular robots are classified according to its hardware to homogeneous or heterogeneous design. The homogeneous modular robots contain many modules that have the same design and same control system which connected to build a robot. With this type, the position of the module can define its functionality. The heterogeneous modular robots contain an exact number of modules that have a different shape for a different function. In this type, the function of the module can define its position [16]. In this section, the homogeneous type is discussed because it can be widely used in a search and rescue task.

Based on the design of modules, the homogeneous self-reconfigurable robot can be divided into two categories: lattice-type and chain-type. In lattice-type robots, the self-reconfiguration is achieved by moving the modular, that requiring changing its position on the surface of other modules. The example of this type is A-TRON [17] which is a simple modular robot with one rotational DOF and it has eight connection ports (four male and four female connections). Although, it has one rotational DOF, it can operate locomotion by self-configuration to shape like a car or sink like [18]. See Figure 2.2. However, it has low speed and its size still the main issues to use with limited access.

(a) (b)

Figure 2.2 (a)The ATRON module, 11 cm in diameter. Left: CAD model of the ATRON module with plastic cover. Right: Photo of a fully functional ATRON. (b) Three groups of seven ATRON modules. From left to right, the configurations are snake, cluster-walk and car [18].

In the chain-type, the module can be connected and disconnected with other modules along with the joint motion of chains to different reconfiguration shape. An example of such Robots includes Conor [16], PloyBot [19], M-TRAN I-III [15] [20], SuperBot [21], and UBot [22]. The differences between these modules Robots are the number and the type of connection ports, the number of actuators, the number of DOF and control algorithm of self-configuration procedure. You can see the differences in modular robot designs in the Figure 2.3. All these Robots can be configured a shape that can provide a locomotion movement.

The commonly used modular Robot is the M-TRAN, see Figure 2.4. In 2002, Murata presented a robotic system called modular transformer (M-TRAN). Each one module of (M-TRAN) contains two semi-cylindrical boxed and a link that connects them together.

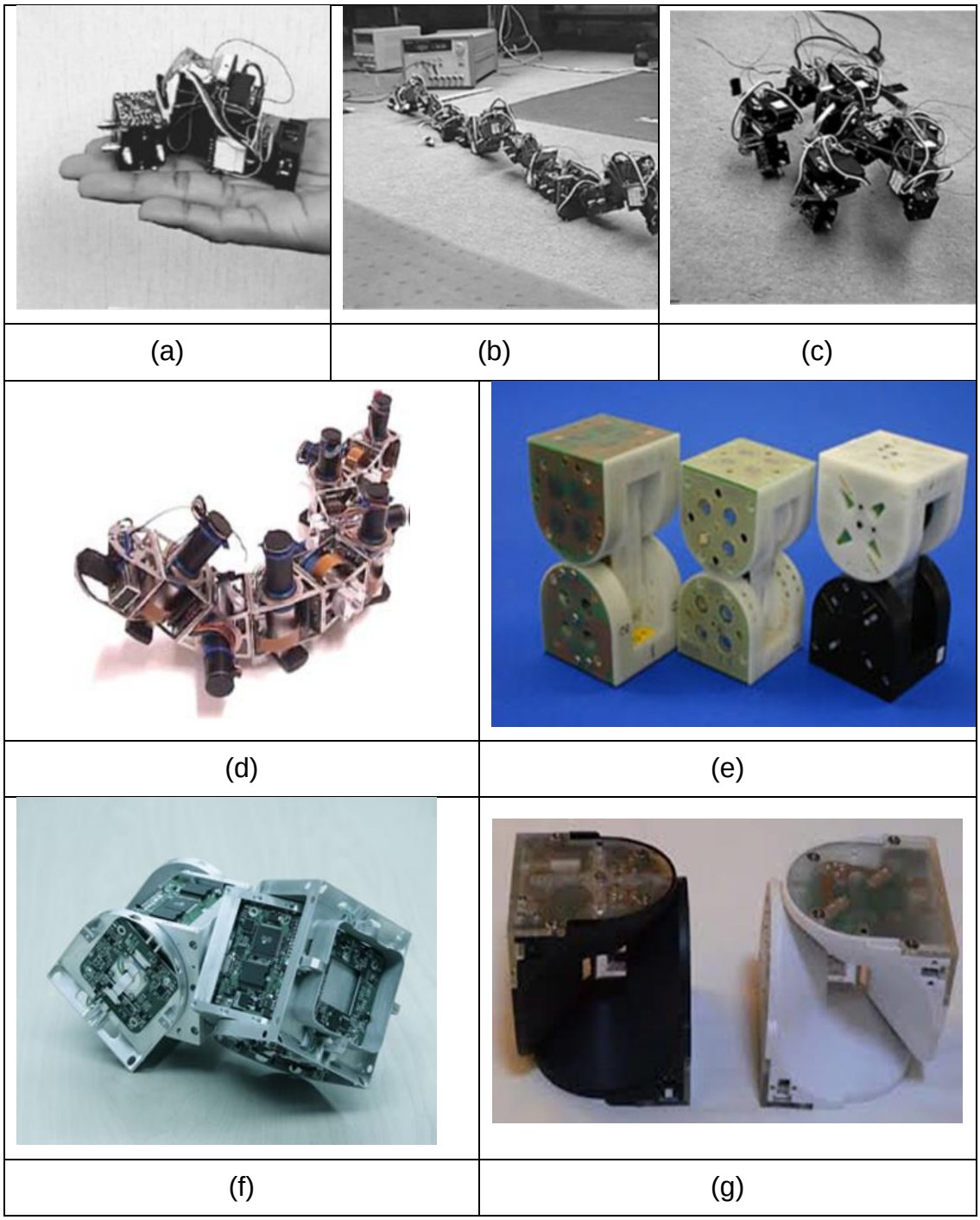

Figure 2.3 (a) Conro module. (b) Conro robot at snake form. (c) Conro robot at quadruped form. [16] (d) Nine PlayBot modules attached together in a snake configuration. [19] (e) M-TRAN Module I (left) II (center) III (right). [20] (f)SuperBot module. [21] (g) UBot modules. Active module (left). Passive module (right). [22]

Every box can rotate from -90º to 90º around the axis at the end of the link from two sides by using two embedded servomotors. Every module has an active and passive box, and every box has three connection surfaces. The connection approaches depend on the permanent magnet in M-TRAN I, but it is changed to mechanical connection driven by servomotor in M-TRAN III [20]. You can see the specification of the M-TRAN III in the Table 2.2.

Table 2.2 M-TRAN III Specifications [20].

Size and weight	65 x 65 x 130 mm, 420 g
Case material	Polyacetal, ABS (link)
Motor	Link: HS-GM21-DSD/KS2 (STL Japan) x2 Connection: HS-GM21-ALG (STL Japan)x3
CPU	Main: HD64F7047 (32 bit, Renesus Corp) Sub: HD64F3687 (16 bit, Renesus Corp)x2; HD64F3694 (16 bit, Renesus Corp)
Network	CAN bus (1 Mbps)
Wireless communication	Bluetooth wireless modem (Zeevo ZV3001Z)
Sensor	10x IR proximity sensors IR diode (Panasonic LNA2801A) x13 IR sensor (TAOS TSL260) x13 Acceleration sensor (analog devices ADXL202E) x2
Battery	Lithium-polymer (K&S Thunder Power 7.4 V, 730 mAh)

Figure 2.4 MTRAN III four legged configuration [20].

You can see from the table that the size and weight still the issues for using this robot in search and rescue mission when the mission required inserting from limited access. The table also shows the many components that are contained in one module such as five motors and 36 sensors. Moreover, the self-reconfiguration process required more space and time which are not available in search and rescue task.

When the modular robots are presented as a solution for search and rescue tasks, they are facing many essential issues. The first issue comes from the advancing of self-reconfiguration which is the connection and disconnection process, this process consumes much time and power, and sometimes the connection port failure. Therefore, Davey introduced a manual connection system for modular robots called ModLock, which is stronger than the other self-configuration connection and he believes that the connection strength is insufficient in many modular robots [2]. Table 2.3 summarizes the weight, dimensions and connector type for some modular robot.

Furthermore, the modular robot has a complex self-reconfiguration planning and control. Some research still studies the self-reconfiguration planning problem to find the least number of reconfiguration steps that are required to transform the modular robot’s configuration [23].

Table 2.3 Physical Characteristics of some self- reconfigurable systems.

System	Weight (g)	Dimensions (cm)	Connector type	Unisex
CONRO	115	10.8 × 5.4 × 4.5	Mech. Pin/Hole, SMA	No
Polybot	200	5 × 5 × 5	Mech. Pin/Hole, SMA	Yes
M-TRAN	400	6 × 6 × 12	(Versions I&II) SMA+Perm Magnets, (version III) Mech. Hooks	No
ATRON	850	ø11	Mech. Hooks	No

In concluding, the self-reconfiguration robot has an advantage of overcoming obstacles by changing its shape, but it still have many issues which prevent it to be a useful rescue robot.

2.2.2 Modular Snake Robots

Many researchers adopted to use a structure of robots which are inspired from snake locomotion, in a search and rescue mission. There are many advantages of using this type of robots. Such as: they have an appropriate flexibility to move in diverse environments, they can change their gaits to overcome different obstacles, and they can access through small holes that cannot be accessed by traditional rescue robots. The snake robots usually consist of segments, which are almost similar in the same robot, but sometimes they have slight differences. These segments have a movement of one DOF or two DOF (in special design they have 3 DOF). When these segments are connected, they give snake robot high DOF and flexibility.

However, the simulation of snake locomotion is a very challenging process that lead to design many different types of robots to achieve this goal. These snake robots, which are used in rescue missions, can be classified into three categories: (a) The snake robots based on undulation using vertical were such as a Modular Snake Robot [24] and a Unified Modular Snake Robot [25]. (b) The snake robots with active wheels such as SOURYU [26] and KAIRO3 [27]. (c) The snake robots with active treads such as KOHGA2 [28] and OmniTread OT-4 [29].

The snake robots that based on undulation using vertical wave consist of segments that have one DOF and connected alternatively. For example, Wright designed the Unified Modular Snake robot that uses 16 modules units (including head and tail). Every module is rigid and contains two half joints of one DOF. Each joint can rotate 180o around the actuated axis. In each module, the actuated axis in its front rotated by 90^{o} from actuated axis in its end. The module dimensions are 5.08 cm in diameter and 5.08 cm between joint axes. These modules give the Unified snake robot 16 degrees of freedom when they connected [25], see Figure 2.5. The Table 2.4 contains all specifications of Unified snake robots.

Another example is the modular snake robot design by Chavan [30]. This snake robot consists of six modules with the head. A servo motor is used to drive each module. The actuated axes of the servo motor for each module is rotated 90o in the next module, i.e., the first module moves in a horizontal motion and the second module moves in a vertical motion.

Table 2.4 Unified snake robot specifications.

Power	36 V, 1.5 A (typical) 8.0 A (theoretical max)
Data	RS-485 Serial
Video	Analog NTSC
Sensors	3-axis Accelerometer, 3-axis Gyroscope, Temperature, Voltage, Motor Current, Joint Angle
Actuators	36 V Brushed DC Motor SMA Wire Parking Brake
Torque	1.3 Nm Continuous
Mass	One Module: 0.16 kg Full 16 Module Robot: 2.9 kg
Dimensions	5.1 cm Diameter x 94 cm Length

Figure 2.5 Photograph of the Unified Snake Robot climbing a tree [25].

SOURYU and KAIRO3 robots are the examples of the second type of snake robot which are using an active wheeled locomotion system. Suzuki presented the development of SOURYU VII to SOURYU IX [26]. Figure 2.6 shows the shapes and specification of them. SOURYU VII has multiple active wheels and an active elastic trunk. It consists of eight rigid segments and seven elastic segments. The rigid segment made from plastic and the elastic segment made from rubber. The locomotion system is driven by eleven actuators, eight for the wheels and three for the trunk. The three trunk actuators operate the pulling and releasing for the three stainless-steel wires, which are passing through the trunk from head to tail, to generate the yaw and binding movement.

At SOURYU VIII, the numbers of trunk segment increased to eight semi-rigid and nine elastic segments. The number of wheels increases to ten, with ten actuators to drive them, changing the mechanism of trunk bending and made it driven by two actuators which are control two stainless-steel wires. While the improvement in SOURYU IX is using the passive elastic trunk connected to the rear of the active elastic trunk. The joint between them can be rotated 90^{o} to make the axis of active eight wheels of the rear trunk perpendicular to the axis of active ten wheels of the front trunk.

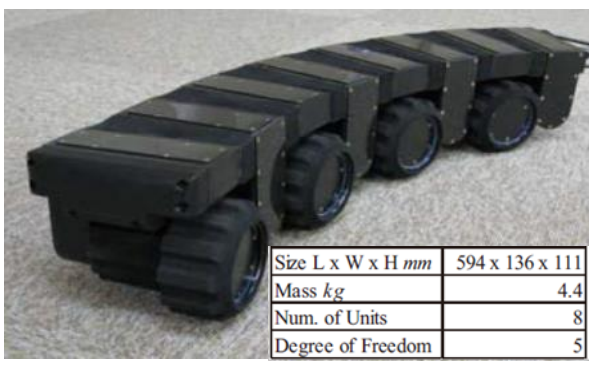

Size L x W x H *mm*	594 x 136 x 111
Mass *kg*	4.4
Num. of Units	8
Degree of Freedom	5

(a)

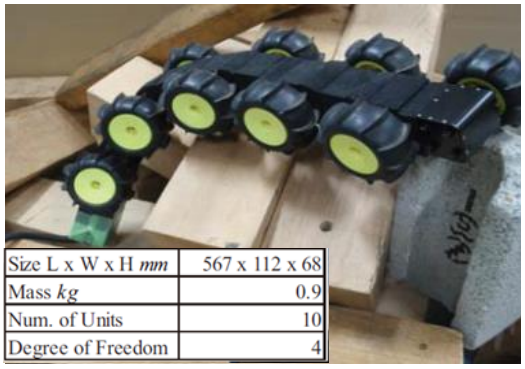

Size L x W x H *mm*	567 x 112 x 68
Mass *kg*	0.9
Num. of Units	10
Degree of Freedom	4

(b)

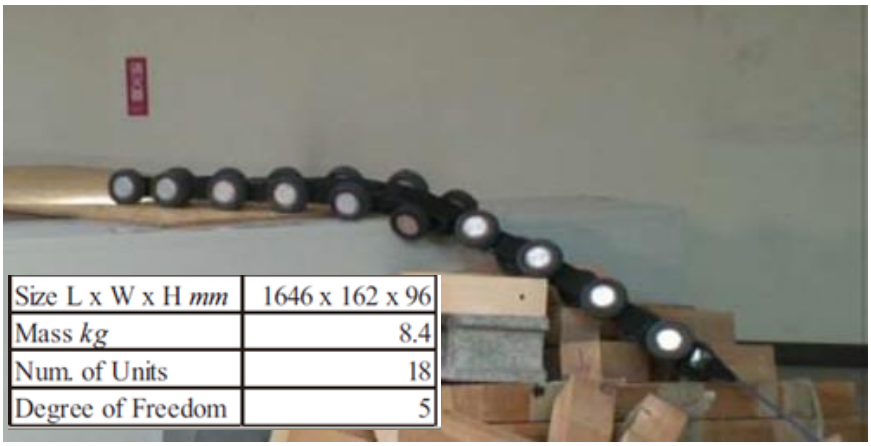

Size L x W x H *mm*	1646 x 162 x 96
Mass *kg*	8.4
Num. of Units	18
Degree of Freedom	5

(c)

Figure 2.6 Overview of the (a) Souryu-VII and its specification. (b) Souryu-VIII and its specification. (c) Souryu-IX and its specification [26].

Another example is the KAIRO3 which can be also classified as a heterogeneous modular robot because it has two types of modules that built it. These two types are the drive modules and the joint modules. The drive modules have three pairs of active wheels. Each joint module has three actuated joints which are located at the front, rear and middle of each joint module. In addition, the axis of the middle actuator is tilted by 45^{o} to the central axis of the joint module. This modular design gave more flexible motion to the KAIRO3. The number of modules that built KAIRO3 is six drive modules and five joint modules. The overall robot specifications are 1.8 m length, 16 cm diameter, and a weight of about 47 kg, See Figure 2.7.

Figure 2.7 The modular snake-like inspection robot KAIRO 3 [27].

The example of active tread snake robots is the OmniTread OT-4, See Figure 2.8. This robot consists of seven segments and six 2 DOF joints. The center segment contains the motor that provides rotary power to each segment through a drive shaft spine. Each segment #2 and #6 contain a miniature air compressor that produces pneumatic power. This pneumatic power is used to operate the 2 DOF joints [29]. The overall specifications are 94 cm length, 8.2 cm width, 8.2 cm thickness and its weight 4 kg. It is a very useful robot for the environment of the search and rescue. Furthermore, it can pass through a 10 cm hole and cannot be staked because the active treads cover all body from four sides.

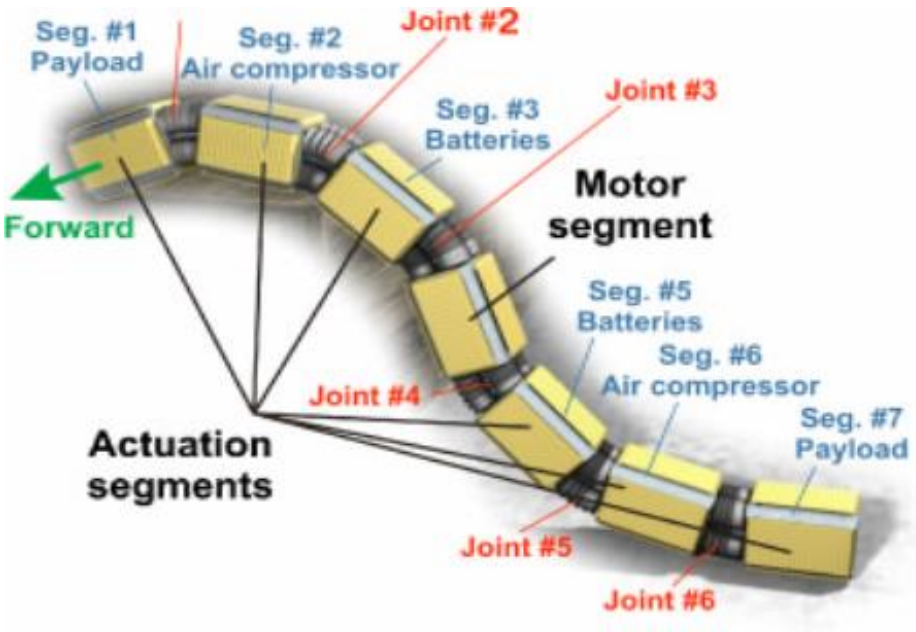

Figure 2.8 Nomenclature and functions for segments and joints in the OT-4 [29].

2.2.3 Legged Robots

Some researches adopt the legs as a locomotion system for robots used in the search and rescue task. They believe that the walking robot can easily overcome many obstacles by producing algorithms in all types of terrain in an advantage. Karakurt design a six-legged Spider robot which called TKSPIDER1 [31], See Figure 2.9. This robot can overcome many obstacles by using different gaits, but it is still having the same issues of traditional rescue robot which are the size and weight.

Daves designed a robot with four legs called Cricket [32], See Figure 2.10. It is very useful to use at complex three-dimensional environment because it has four joint at each leg with the tracked part in the end.

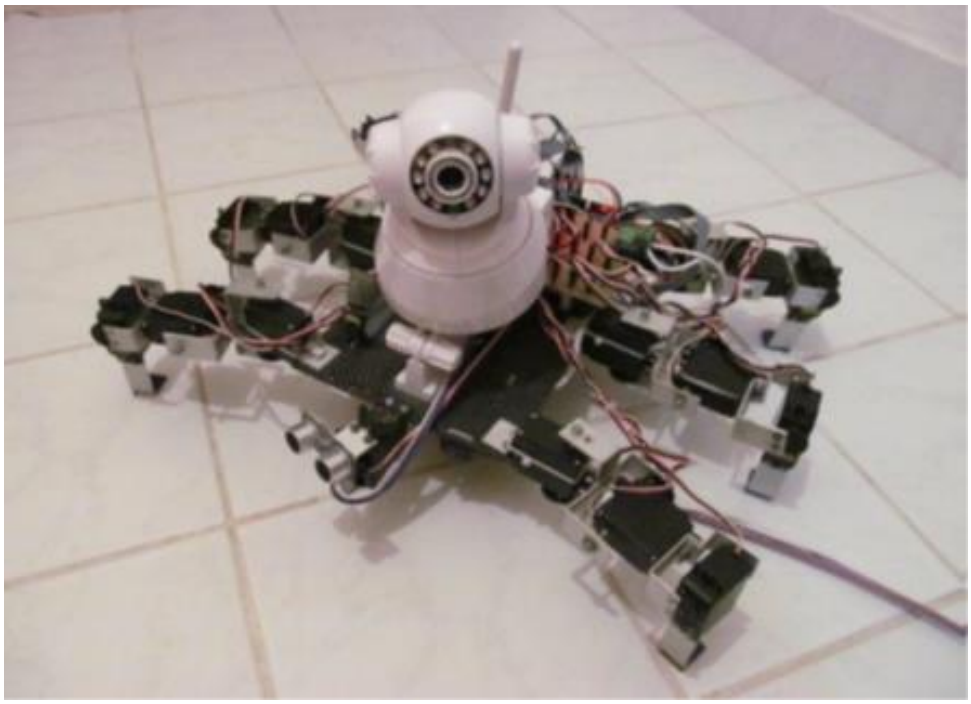

Figure 2.9 TKSPIDER1[31].

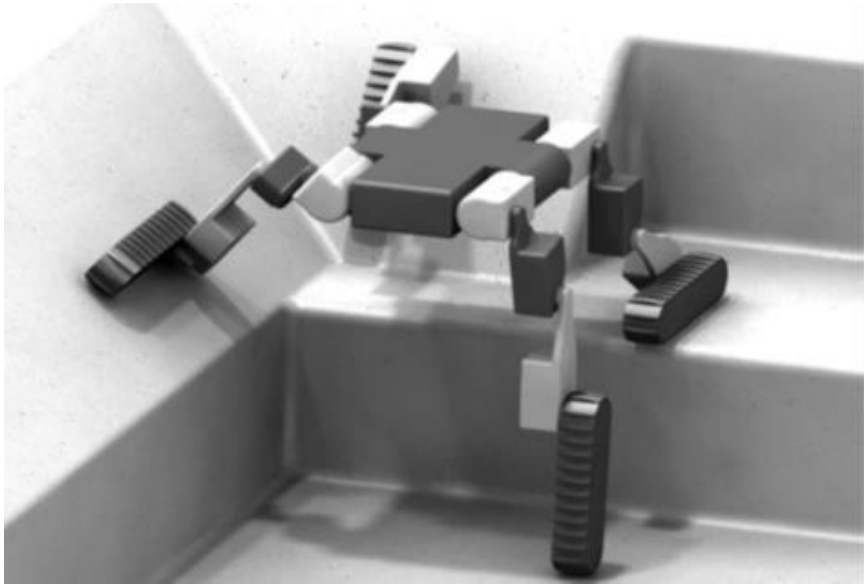

Figure 2.10 Cricket Robot with Joint Indications [32].

2.2.4 Swarm Robots

Swarm robotics is a new approach that recently used for SAR tasks. In this approach, many robots are used to operating tasks individually and as groups. Each robot is an autonomous agent that has actuators and sensors to be capable of searching autonomously. Swarm robots are capable of collaborating to do complex tasks such as transporting objects, moving over a hole, etc. [33].

Nowadays, the swarm robots in SAR means using a group of low-cost robots to perform the task of search and rescue in collaboration [34]. The searchers focused on the control system rather than the structure of the swarm robot. The control system for every robot should have the ability to work autonomously and with the group at the same time [35]. Recently, many control system approaches are used to gives useful behavior of swarm robots during the collaboration to preform SAR tasks and these approaches are still in progress [36]–[38].

2.3 Minimally invasive Robots

The minimally invasive technique is the procedure of using a robot with small size to reduce or eliminate any damage that can happen due to the operation of the task. This technique should be used in the search and rescue missions when the rubble prevents to get sufficient access, and there is a concern of secondary collapses. This technique is commonly used in surgery as ‘ Minimally Invasive Surgery’. The first time it was used by the National Aeronautics and Space

Administration (NASA) in 1972 as a project for producing a remote surgical system for astronauts [39].

After a few years, a new surgical technique was invented in 1980 called " Minimally Invasive Surgery " MIS [40]. Nowadays, many robotic surgery systems are designed according to this technique. For example, the DA Vinci robot [41] which is the minimally invasive system used to operate many types of surgery for the last fifteen years. This system made many benefits to the patients such as they experience less pain, lose less blood, have smaller incisions, have faster recovery, and can quickly return to their normal activities [39]. Furthermore, This system is very accurate, and its arms can be inserted into a small incision in the body, but it requires a bulky system outside the patient's body to provide the high degree of freedom for the end-effector.

This type of design can be useful for the surgery, but it is not useful for other minimally invasive cases. However, The technique of minimally invasive can be used for another robot applications such as search and rescue and exploration and archeology.

2.4 Folding Robots

Using the folding structure is an appropriate way to have a rescue robot that could be inserted from limited access and change its structure to avoid the obstacles of the collapsed rubble. This approach could build a 3D structure from the 2D sheet and could create reconfiguration structures. The folding robots are inspired from the “origami” which is the Japanese’s word that means the art of folding papers. In this section, the recent researches of folding robots are discussed starting from printable manual folding robot reaching for the self-folding structures and robots.

However, there are no real applications of folding robots in search and rescue field except the two papers by Lee that present a prototype of rescue robots using origami wheels. Lee designed a robot with deformable wheels using the origami magic ball pattern to fabricate the wheels, See Figure 2.11. These wheels made from paper that is coated with Kapton film and laser machine was used to make the pattern. The diameter of these wheels is 70 mm, but by deforming them, the robot height decreases to 55 mm [42].

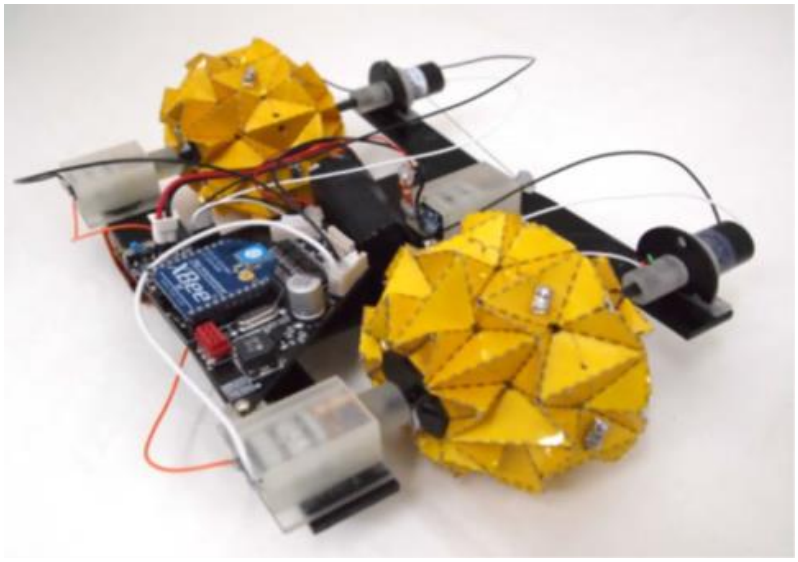

Figure 2.11 The Deformable Wheel Robot [42].

In 2014, Lee designed another robot which can be used on a rescue mission. He used the same wheel design of the previous robot, but he made it from a different material. The wheels are made of fabric, adhesive layer and P.V.C segments. Steel hooks are attached to the outer surface of the wheel to increase the robot's climbing ability, See Figure 2.12. The specification of this robot is 970 g weight, 0.3 m/s maximum speed and 55mm wheel diameter that can be increased to reach 120 mm (with the hooks). DC motor, sliding shaft and cable are used in the wheel deformation mechanisms [43].

The two robots using a folding structure to fabricate a simple part of the robot, but the unique characteristics of folding open the future to many unexpected designs that can be adopted in many robotic fields. For that reason, many researchers start to investigate the folding robot from different aspects in the last few years.

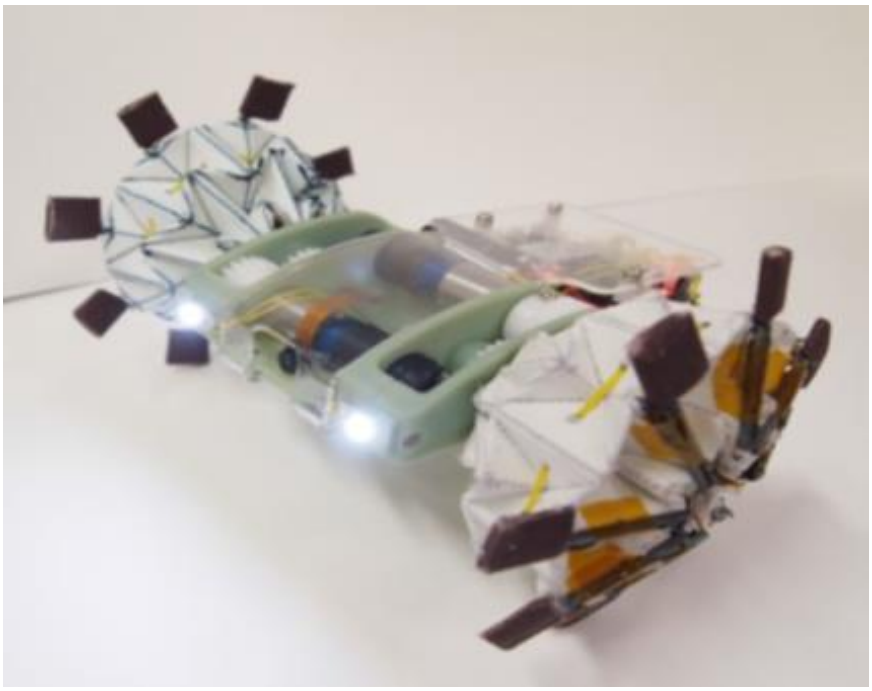

Figure 2.12 Origami Wheel Robot with hooks [43].

The two major categories of folding material depending on the folding process which are the manual folding and self-folding robots. These two categories depend on the same steps to fabricate the folding robots which are: 1.Planner and design the pattern, 2.select materials and fabrication procedure, and 3.choose the actuators that operate the motion or locomotion in manual folding robots or operate the self-folding and locomotion in the self-folding robots. The researchers focus on how to fabricate simple, cheap and fast fabrication robots by using a folding approach. While in self-folding, the researchers focus on morphing the 2D sheet into 3D structure at the operation task or how can build reconfiguration robots by using folding approach.

Some researchers build a printable robot using paper and folding it manually [44] [45]. Hoff used an origami structure, which is called “twisted tower” to create a thread actuated origami robot, see Figure 2.13. He called it Origami Bot-I Robot. This design can generate bending and twisting motions by pushing, pulling or torsional force applied to the origami structure. The origami Bot-I can be used as a manipulating arm and a worm-like crawling robot by using four DC motors. It can move at the speed 0.25 inch/Sec when using the directional passive flaps to prohibit backward movement [44].

Zhang [45] built a worm-like robot, which is inspired by origami, using 0.3 mm thick sheet paper and shape memory alloy (SMA) as an actuator. This robot has a very slow speed because of the long time that's required for cooling the SMA springs before it can be actuated again [45]. Other researchers built a printable robot, but they use a polyester sheet and folding it manually. For example, Agheli use a single sheet of polyester with a laser cutting machine to fabricate a lightweight foldable hexapod robot (42 g) which can be used for swarm applications over rough terrain [46].

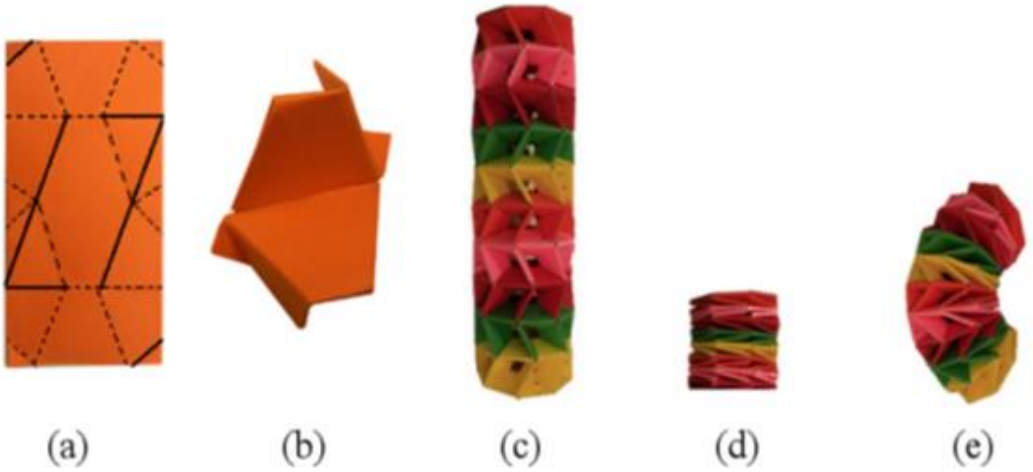

Figure 2.13 Twisted tower: (a) creases to fold an origami segment, (b) folded segment, (c) assembled tower when extended, (d) assembled tower when fully contracted, and (e) assembled tower when bent [44].

Mehta [47] has developed a design environment to quickly and easily fabricate printable robots. He built up a method that could abstract 2D fold patterns using scripted objects which are written in the Python language. This method can generate hierarchical printable-folding mechanical designs [47]. Furthermore, Metha used four ways to fabricate the printable robot and compared these different ways [48]. These ways to fabricate a robot use:

1. Laser cutting machine and a polyester sheet with manual folding.

2. Printed paper with manual cutting and folding.

3. 3D printer to print 3D structure. It does not require folding process (it should be not considered as folding robots because it is printed as a solid object).

4. Three layers that contain a top cardboard, shape memory polymers, and bottom cardboard layer. These layers can be assembled to form a self-folding structure which goes to required design geometry when it is heated.

The aim of Mehta's research is to simplify the design and fabrication process of folding robots to make it easy to use by non-expert persons. The work produces a library of many scripts to design folding robots that can be used in the future for different applications.

2.4.1 Self-folding Structures

Self-folding is the ability of the structure to fold and/or unfold without human intervention or any application of external manipulation. The common approach to reach this capacity is using active materials as an agent to fold generation. The active material is a material that has the capability to convert many types of energy to mechanical work [49]. The examples of it are the shape memory alloys (SMA) and the shape memory polymers (SMP). These active materials can operate folding or sometimes unfolding process for self-folding structures when they are used as actuators. The approach of generating folds using active material can be divided into two categories: hinge type and bending type.

Most hinge-type work as actuators according to these three concepts 'extensional', 'torsional' and 'flexural'. The extension concept means that the length of active material, which is used as a rod or spring form and attached from its ends to the faces connected by hinge, controls the rotation of the hinge, See Figure 2.14 (a). The torsional concept uses spring or a rod, which made from active materials to provide twist at the hinge. The rotation of the hinge depends on the twist angle of the active material [50], See Figure 2.14 (b). In the flexural concept, the active material can be present a folded configuration that has been manufactured to form it, before it is deformed to a flat configuration. This active material bonded to the faces of the passive material and when it returns to its folded configuration, the local hinge take the same form, See Figure 2.14 (c).

All these types can operate folding in both directions by putting an active material that worked opposite to the major one. For example, it can make the torsional concept folding in both directions by using two active materials that have a twist in opposite directions. Furthermore, this can be achieved in extensional and flexural concepts by using two active elements that work one opposite to another. (i.e., have opposite configurations for the flexural or attached on opposite sides of the sheet for the extensional).

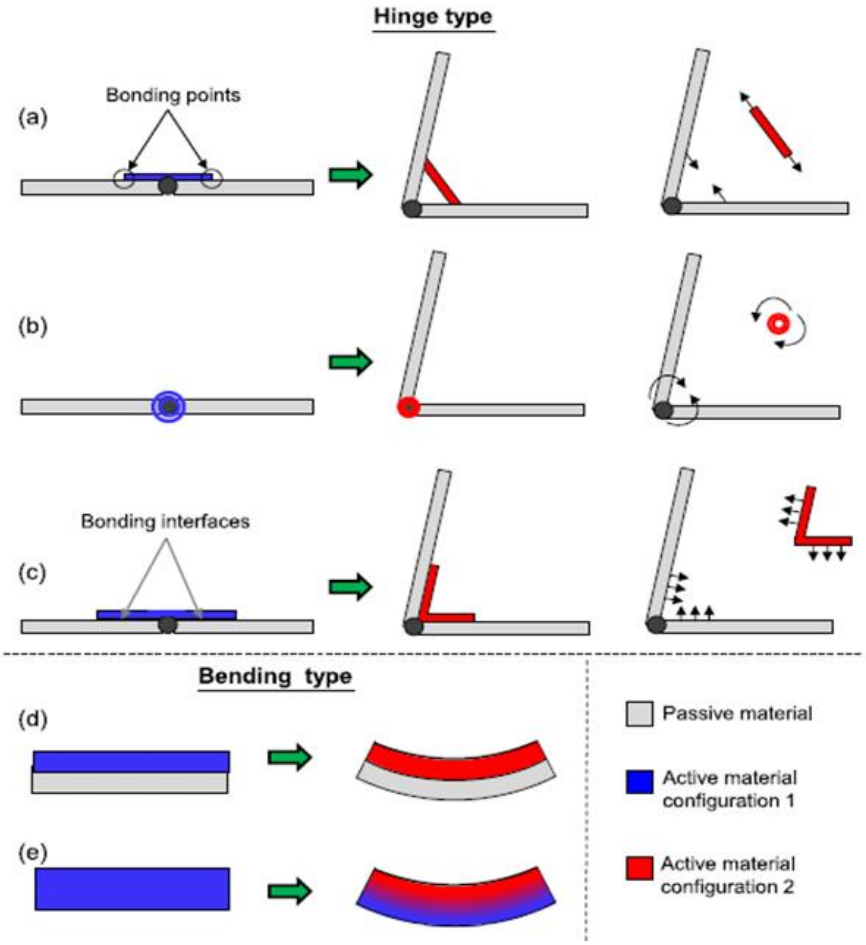

Figure 2.14 Basic active fold concepts. Hinge type: (a) extensional, (b) torsional, and (c) flexural. Individual simplified free body diagrams of the hinge-face structure and the active element are also shown. Bending type: (d) bilayer consisting of an active and a passive layer, and (e) single layer subjected to graded driving field. [51]

The other type of generating folding is the bending. In this type, the active material can directly cause for sheet bending and sometimes without using the hinge mechanism. This type contains two kinds which are the single layer and multi-layer, See Figure 2.14 (d) and (e). The single layer concept is the approach of self-folding via bending by using one active layer without hinges. In this type, the bending in sheet became from the actuation strain distribution through the sheet thickness, which is generated from the gradient of active layer when it is subjected to a graded driving field. However, this type of folding is difficult since it is not effective to maintain gradients at specific locations in some physical fields [52].

In the multi-layer concept, the sheet made from two or more layer laminate with some passive layer and some active layer. If it is made from two layers, it consists of one passive and one active layer. When the active material activated by applying an actuation inducing field (thermal, magnetic, etc.), it is deformed axially (generally shrinkage). While the passive material is not deformed and this difference between the two layers makes the sheet locally bending. This concept can be applied to generate two directional bending by using three layers, which consists of two opposing actuator layers of active material and separated by a passive material [51]. It is noticed that the self-folding structures are not entirely depended on the active material actuators. However, they are the most commonly used, but there is some application of self-folding depend on another actuator, such as a small type of the servo motor [53].

For the clear understanding of active self-folding structures, some examples of self-folding structures are demonstrated here. Most of these structures depend on thermally-activated self-folding. This approach is widely used for self-folding because there are many methods available for localized supply of heat. However, there is a design challenge for controlling the particular distribution of temperature because of the diffusive nature of heat. Most of thermally-activated self-folding using SMAs and SMPs as an actuator.

On the SMA side, Hawkes and Paik [54] [55] developed a concept of self-morphing origami. They designed and fabricated a sheet with repeated triangular tiles, which are connected by actuated hinges to create a universal crease pattern. The actuating hinges, which are used on the edges of triangular tiles, are made from thin (100 μm) Nitinol foil. This sheet provides high flexibility to form many shapes because of the configuration of the repeated triangular tiles that the sheet consists of them. This system achieves to folding many traditional origami shapes such as a plane or a boat from the single planar sheet and it improves that it is successful to be a self-folding origami structures, See Figure 2.15.

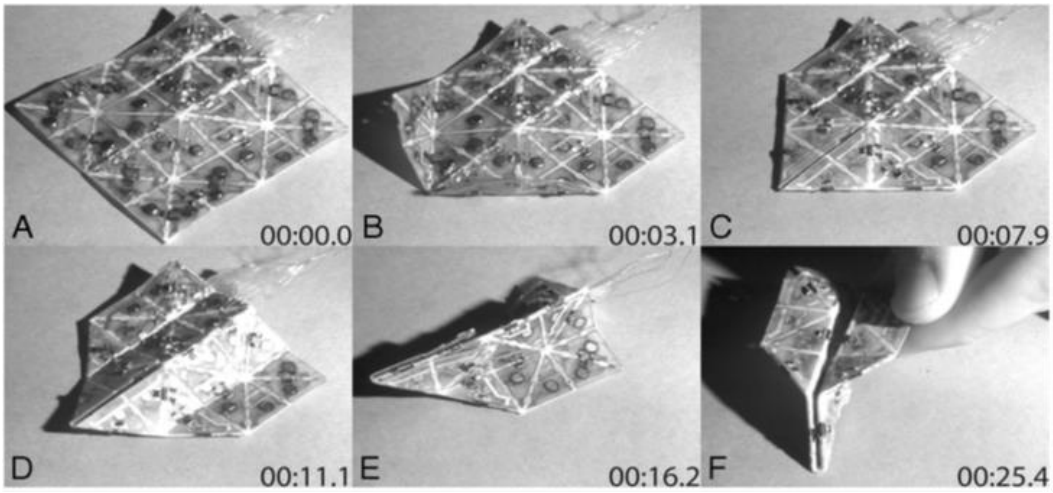

Figure 2.15 Sheet with SMA hinges. A flat sheet maneuvers to fold towards an airplane shape [55].

An and Rus developed this approach to be considered for n×m self-folding sheet. They presented a design and programming guide for this type of self-folding sheet. Furthermore, they described and analyzed the model and the algorithms that create the designs and programs for the self-folding sheets [56].

Moreover, self-folding using SMA are also adopted to design robots. Onel Introduced an origami-inspired strategy that considers the ability to create a three-dimensional robotic system by using two-dimensional fabrication methods [57]. Complicated bodies of origami robots can fabricate by using flat sheet and laser machine. They presented the fabrication and assembly process of a worm-like robot that can undergo peristaltic locomotion [3]. NiTi spring actuators are installed on the body of the worm-like robot to generate the locomotion actions, See Figure 2.16. Firouzeh developed a four-fold robot that can be moved using four folded legs actuated with SMA [58] [59]. This small robot showed promising locomotion characteristics, See Figure 2.17.

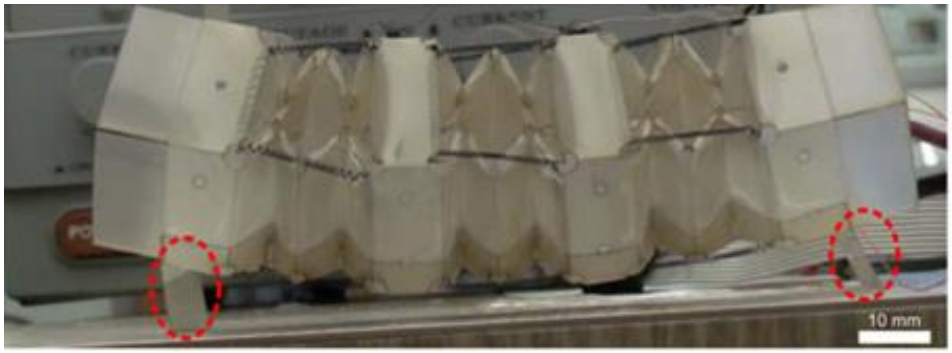

Figure 2.16 The worm-like robot with NiTi spring actuators on the body to generate the locomotion actions [3].

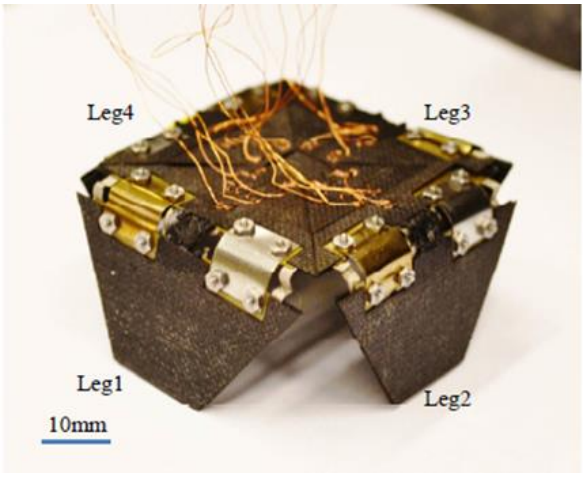

Figure 2.17 Four-fold robot prototype with bidirectional actuators and sensors [58].

The other type of thermally activated actuators is the SMPs which provides actuation at high strain with low force. The researchers have studied different approaches to heating the SMP, such as uniform heating, resistive heaters and light activation [60]. For the uniform heating activation, the self-folding structure consists of three layers of making the SMP layers in the middle of two paperboards or plastic sheet layers. They control the angle of folding by having a difference gap width on the outer layers [61]. The patterns of the self-folding structure can be fabricated using laser machine system [62]. Some examples of self-folding structure that using SMP with a uniformly heated, activated are shown in Figure 2.18.

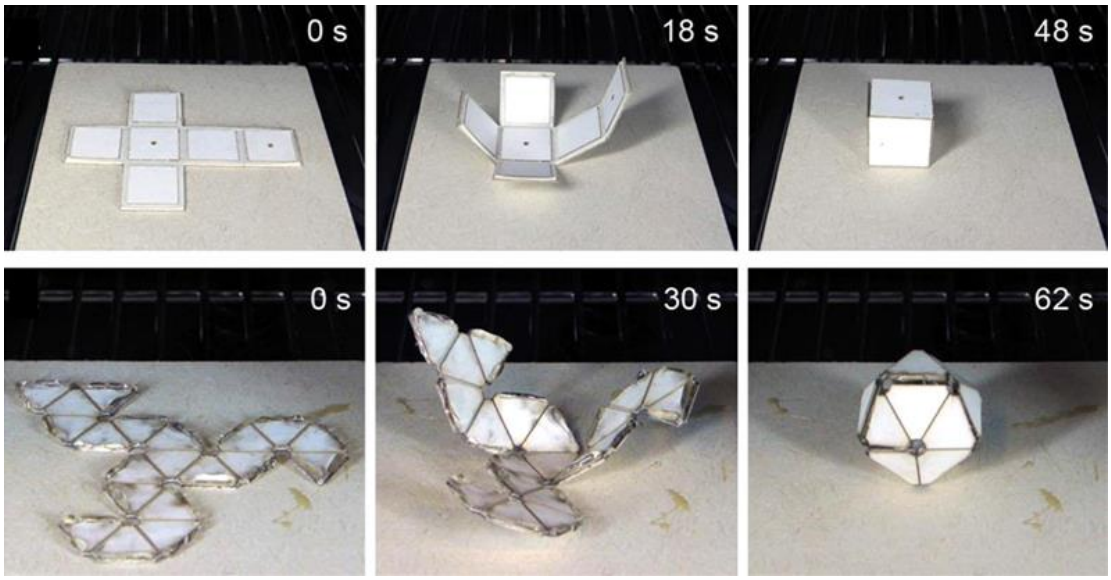

Figure 2.18 SMP-based self-folding structures morphed under uniform heating [62].

The most promising approach is presented by Felton and others from Harvard University [63]. They developed self-folding hinges by using multilayer laminate which consist of SMP, paper or plastic sheet, and resistive circuits [63] [60]. They used an outer layer of SMP from two sides which are the Prestretched polystyrene (PSPS) and commercially known as “shrink-drink”. This Prestretched polymer can exhibit 90% compressive in plane strain when heated to 160^{o} C. This self-folding technique shows the capability of creating complex geometries. They fabricated a printed inchworm robot [63] by using this self-folding approach, See Figure 2.19.

Recently, they developed a crawling robot that folds itself by using five layers. These layers are two outer PSPS layers, two paper layers and the middle layer of the copper-polyimide [4], See Figure 2.20.

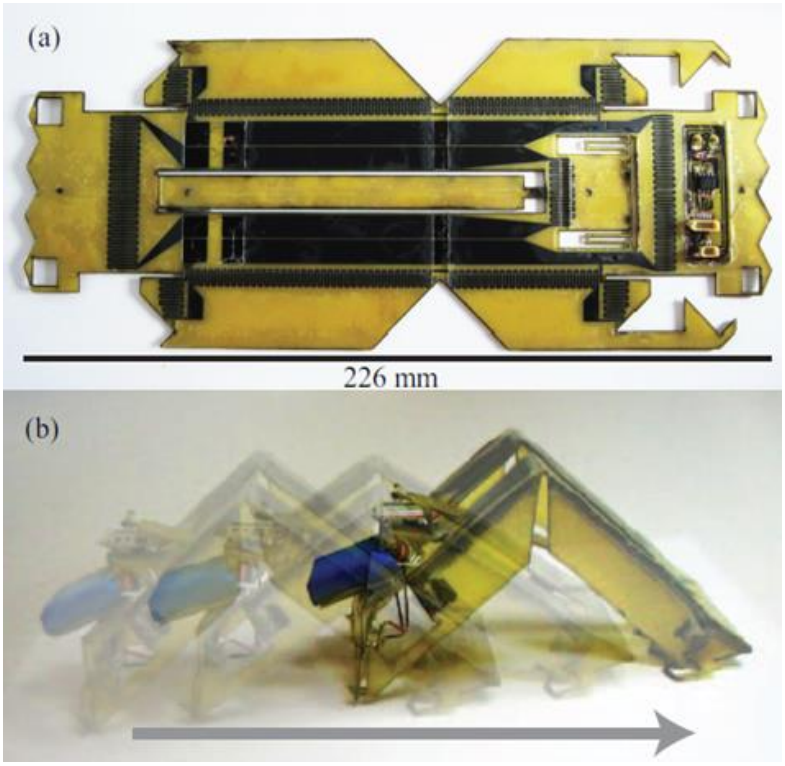

Figure 2.19 (a) The two-dimensional inchworm robot, before it has folded into its functional shape. (b) The folded inchworm, after the servo and battery has been added. This robot weighs 29 g, and moves at a rate of 2 mm/s. [63]

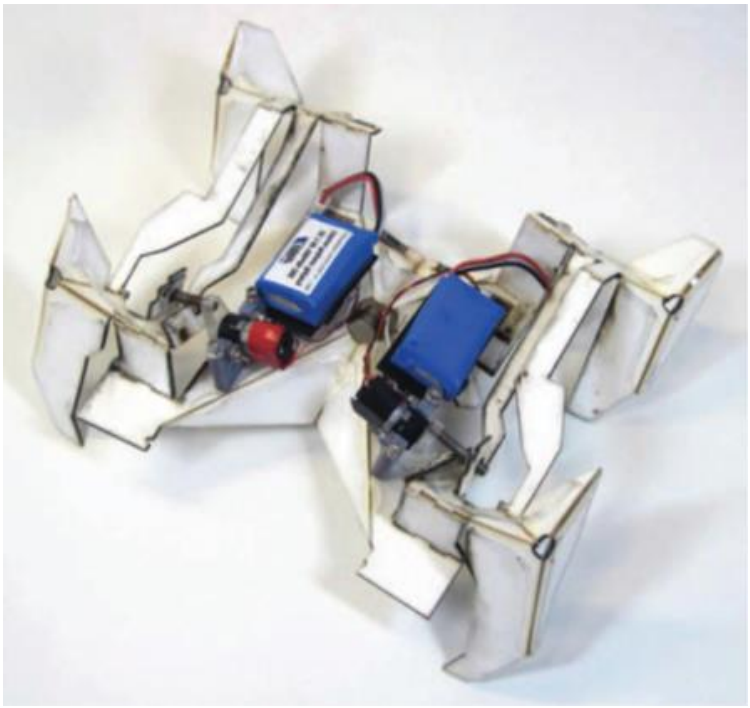

Figure 2.20 A self-folding crawler robot built with the shape-memory composite [4].

Another team from the Massachusetts Institute of Technology (MIT) has success to build a miniature origami robot that self-folds walks, swims and degrades [64]. They fabricate a sheet that can self-fold into a centimetre-sized 3D Robot and actuate immediately for walking, swimming and subsequently dissolve in liquid, See Figure 2.21.

An external magnetic field is used to control the robot. It is exerted by embedded coils underneath the robot, See Figure 2.22. The control system is a huge table that consists of four-square electromagnetic coils. The magnetic flux induced from these electromagnetic coils can be changed depending on the current used to power these coils. the motion of the robot depends on the difference in the magnetic flux that induced from the four electromagnetic coils. The issue of this type of robot is the size of the control system that is used for moving and self-folding [65].

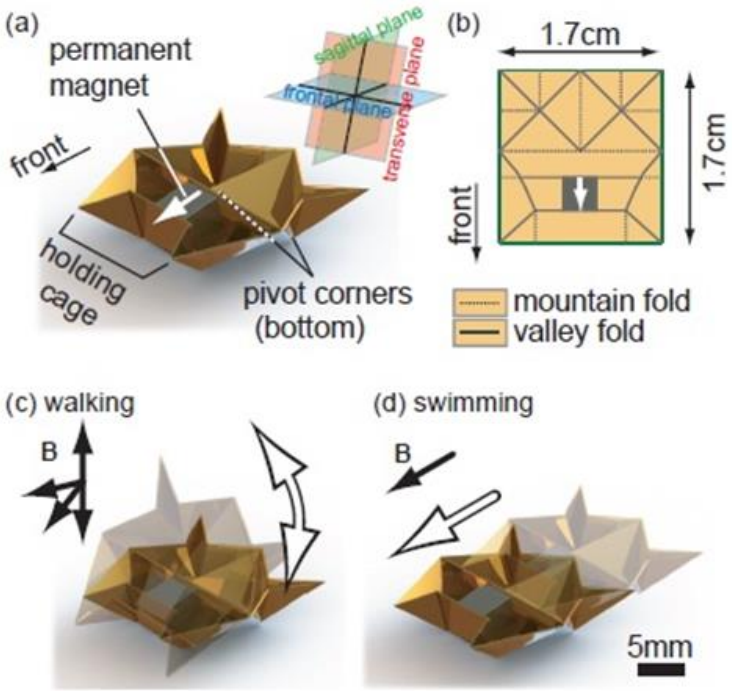

Figure 2.21 The designed mobile robot and the actuation methods. (a)The outlook. (b) The creases pattern. (c) Walking mode by torque-based control. (d) Swimming mode by force-based control.[64]

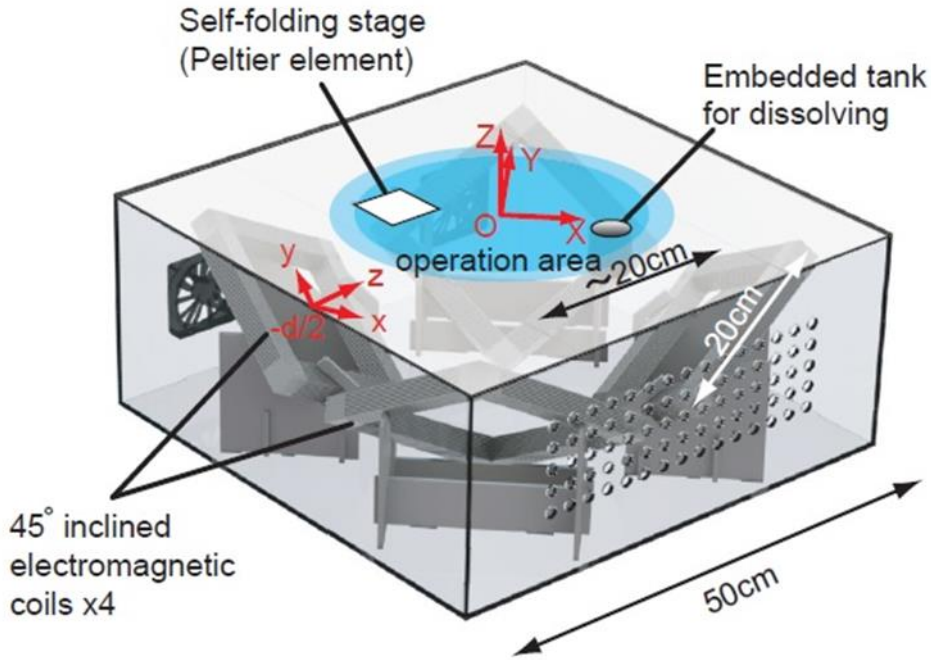

Figure 2.22 The developed electromagnetic coil system. [64]

2.5 Conclusion

In this chapter, many types of robots were demonstrated, which are using in exploration and search and rescue missions, to investigate their specifications and performances. Moreover, the research about folding structures is discussed as a proposed design for robots that can be used in an exploration and search and rescue tasks. From all these research, the following points are concluded:

1. The traditionally tracked rescue robots have many issues which are related to the size and weight. Therefore, they cannot be used in a rescue tasks that have limited access. These robots sometimes stuck between rubble during the operation.
2. The modular robots can operate a rescue task because they can pass over the obstacles by reconfiguration their shape and changing the type of locomotion. However, the process of reconfiguration consumes a lot of power and time and sometimes it is required a plenty space. Furthermore, the connection ports can fail in some modular robots.
3. The snake robots have an appropriate dexterity to insert through the collapsed rubble. They have many design types with different locomotion systems, but many of these designs have a complex control system to simulate the snake locomotion.

4. The legged robots can be programming to change their gait for different terrain in advance, but they still have a big size and heavy weight. Therefore, they are not suitable to use in limited access task.
5. The minimally invasive technique should be used when the rescue robot is designed because always there are concerns of secondary collapses. This technique used in surgery but the surgery system consists of huge robot arms outside patient's body that provide the high degree of freedom to the end effector instruments.
6. Until now, there is no folding exploration or rescue robot except the robot that is fabricated by Lee [42] [43]. This robot is not completely folding structure, but it is used deformable origami wheels.
7. The folding robots are easy to fabricate using many fabrication methods such as print and manually fold, laser cutting, and a 3D printer. All these methods are inexpensive.
8. The self-folding robots give the opportunity to manufacture many types of robots as a plane sheet. This sheet can fold itself during the task operation.
9. The locomotion of folding robots is still dependent on the motors as actuators and the locomotion systems, which depend on SMA actuators, are very slow.

Chapter 3 ORIGAMI STRUCTURES FOR LOCOMOTION AND MANIPULATION

3.1 Introduction

The first step to designing the folding robot is studying the geometry and behaviour of origami structures. The structure, which provides the ability of self-folding behaviour or locomotion behaviour under folding and unfolding process, could be used as a part of a self-folding robot structure. This point leads to study the types of folding structure and their mathematical descriptions.

Therefore, the origami structure is described and explained in this chapter. Moreover, some types of origami structures are analysed, and the ability to use them in mechanical engineering is discussed. In addition, the geometric parameters and mathematical models are defined for these origami structures. The chapter also contains some practical examples of origami structures. The differences between these origami structures are explained in this chapter. The self-folding ability is described with the ability of locomotion. Furthermore, a novel type of origami structure for manipulation is illustrated. Finally, there are conclusions.

3.2 Origami Structure

All folding structures are inspired by origami which is the art of paper folding. The essential difference to origami is that the folding structure could be made from any material, while the paper is the major material for origami structure. However, all the structural design of any folding structure is obtained by using the principles of origami pattern design.

There are some basic origami concepts that should be defined for the clear understanding of origami structures. The creases are the locations of localized folds on the sheet. Every crease can be folded either convex (*mountain*) or concave (*valley*). The final shape of the structure is determined from the creases, folding sequence, folding directions, and folding magnitude. The vertices are the endpoints of the crease lines. The faces are the closed areas that are bounded by the creases. All the creases with its mountain and valley assignments make up the crease pattern. These concepts are shown in Figure 3.1.

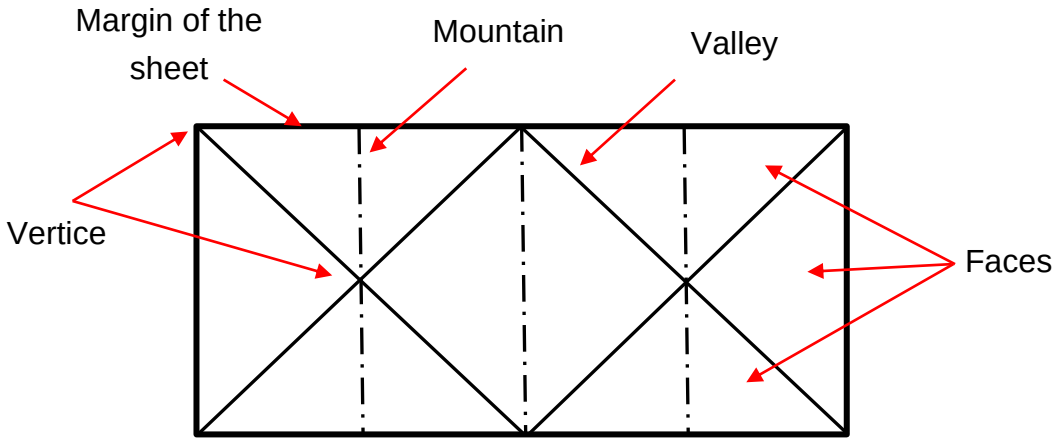

Figure 3.1 Crease pattern illustrating various origami concepts.

The most important parameters that describe the magnitude of a fold are the folding angle and the radius of curvature at the fold line. It is clear that the folds cannot be sharp for the finite thickness sheet. Therefore, it is assumed that the fold has a radius of curvature R. the angle at the intersection of two lines stretching collinearly with respect to the folding faces is known as internal fold angle α_i. The other angle which is defined as $180^{o} - \alpha_i$ is called the external fold angle α_e. See Figure 3.2.

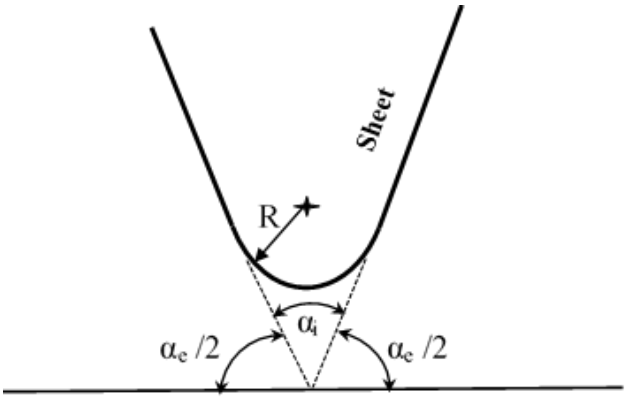

Figure 3.2 Parameters that define the magnitude of a fold.

Every origami crease pattern can be described using mathematical descriptions related to that pattern. Therefore, many equations describe the many origami shapes. All these equations depend on a set of rules in paper folding that define linear folds using points and lines. These rules were set up by Huzita-Justin [66] and they are known as Huzita's seven axioms. At these axioms, the line represents a crease in a piece of paper or the boundary of the paper, and a point is an intersection of two lines.

The axioms State that [67] [68]: *"(a) given two points p1 and p2, we can fold a line connecting them. (b) given two points p1 and p2, we can fold p1 onto p2. (c) given two lines L1 and L2, we can fold L1 onto L2. (d) given a point p1 and a line L1, we can make a fold perpendicular to L1 passing through the point p1. (e) given two points p1 and p2 and a line L1, we can make a fold that places p1 onto L1 and passes through the point p2. (f) given two points p1 and p2 and two lines L1 and L2, we can make a fold that places p1 onto L1 and places p2 onto L2. (g) given a point p1 and two lines L1 and L2, we can make a fold perpendicular to L2 that places p1 onto L1. ".* These operations provide the basis of mathematical origami. Many types of origami pattern are built for different purposes by using these operations and the concepts of crease patterns.

There are many traditional origami patterns, and every year the designers can invent new origami shapes. However, all these shapes can be divided into a lot of categories. In this research, not all these categories could be discussed but just could choose the types that useful for the research project.

Origami could be divided into many categories starting from the "everyday origami"; for example, wrapping presents, folding letters...etc.; passing through the "craft origami" and ending with the "origami puzzles". All these types of origami consist of making shapes from a paper by folding or cutting it. This research is interesting in the origami type that could fabricate shapes with unique mechanical properties. This type is called "Abstract origami" which is the folding of geometric and decorative forms. These forms are either created using one sheet (Tessellation) or created from many sheets (Modular).

In the next section, the modular origami and Tessellation origami are explained with examples.

3.3 Tessellation Origami

The Tessellation origami is a type of origami shape which is produced from a single sheet by using a twist or reverse folding technique. This type has high flexibility and is reconfigurable after folding. These two properties are significant to the functionality of origami robots. Furthermore, the crease patterns of this type consist of a similar element that is repeated many times to form structures on any scale. This property makes it easy to define an actuation procedure for one element and repeat it for all other elements.

The examples of Tessellation origami are

(a) Miura-pattern.

(b) Origami magic ball (Waterbomb).

The major feature which provide by these designs is they can contract and expand in all directions.

3.3.1 Miura Origami

The Miura origami is a periodic structure which contains many identical rigid parallelogram faces that create the geometry of the sheet that folds into a final shape. The parallelogram faces are linked together by edges that represent the crease lines in a crease pattern. These edges are folded into mountain and valley creases to produce the final shape of the Miura origami. Figure 3.3 shows the crease pattern of the Miura origami and its final shape after folding.

Miura origami structure can be divided into many unit cells. Every unit cell has four identical parallelograms which have equal long sides of length b_m, short sides of length a_m, and an acute angle θ_m (which should be between 0^o to 90^o), see Figure 3.4. These parameters are constant and cannot be changed during the folding and unfolding process. The variable parameters that are changed during the folding process are the length (X_{fm}), the width (Y_{fm}) and the hight (h_m) of the Miura unit cell. The other parameter that is changed during the folding process is the projection angle between two ridges (β_m). This angle is required to characterize the folding and unfolding process of the Miura unit cell, and it is an essential parameter that is required to calculate the other parameters for the Miura unit cell. The value of this angle changes from ($\beta_m=2X\theta_m$) for the planar state to ($\beta_m=0$) for the completely folding state.

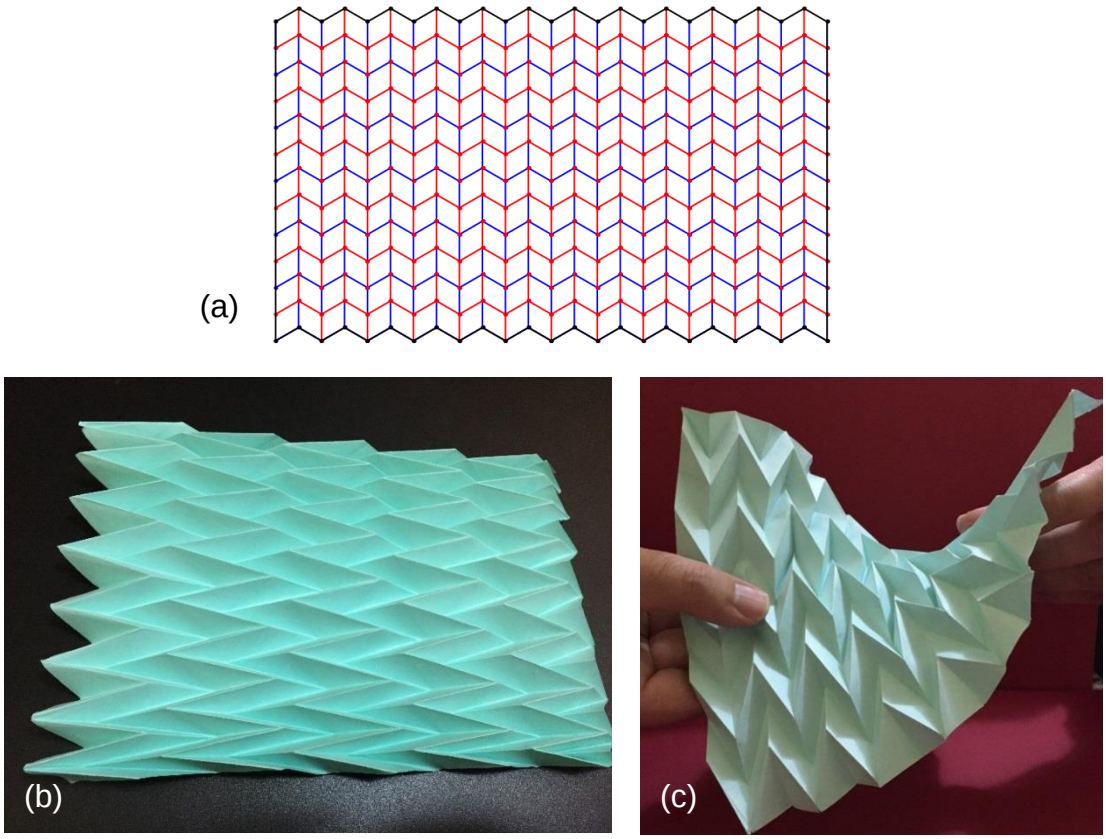

Figure 3.3 (a)The creases pattern of the Miura origami (b) Its final shape after folding (c) The bend ability of the Miura origami.

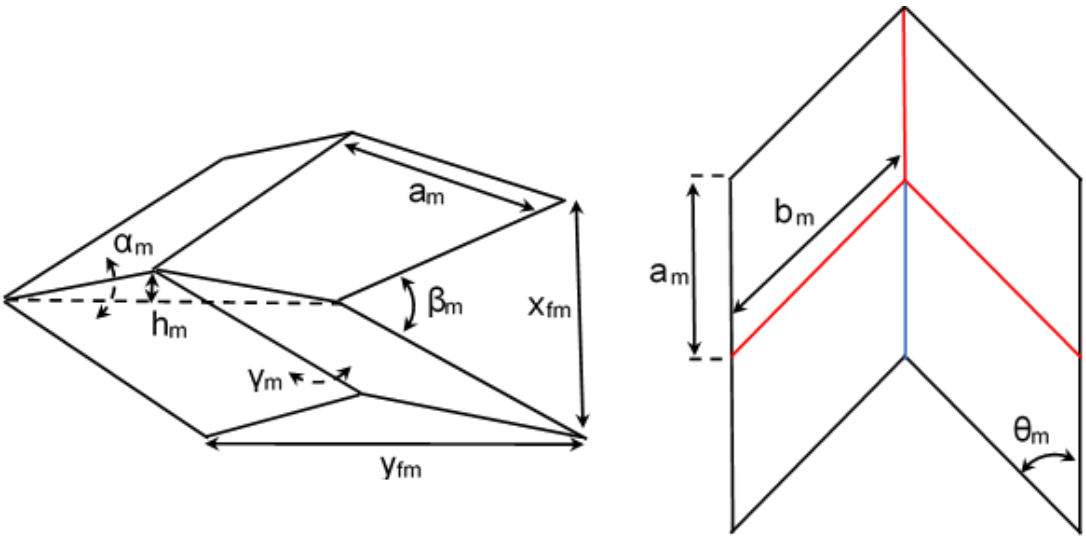

Figure 3.4 Unit cell of Miura origami.

All variable parameters of the Miura unit cell are calculated depending on the constant parameters and the β_m angle as follows:

$$x_{fm} = 2b_m \sin(\beta_m/2) \qquad \textbf{3-1}$$

$$y_{fm} = 2a_m \frac{\cos\theta_m}{\cos(\beta_m/2)} \qquad \textbf{3-2}$$

$$h_m = \frac{a_m\sqrt{\sin^2\theta_m - \sin^2(\beta_m/2)}}{\cos(\beta_m/2)} \qquad \textbf{3-3}$$

The folding of parallelogram faces around the creases line form dihedral angles. These dihedral angles are required to characterize the folding process of the origami pattern. The Miura origami has two dihedral angles γ_m and α_m, see Figure 3.4. Each these angles equal 180° for planar state and 0° for completely folding state. They are calculated using the following equations [69]:

$$\alpha_m = \cos^{-1}\left[1 - 2\frac{\sin^2\left(\beta_m/2\right)}{\sin^2\theta_m}\right] \qquad \textbf{3-4}$$

$$\gamma_m = \cos^{-1}\left[1 - 2\cot^2\theta_m \tan^2\left(\beta_m/2\right)\right] \qquad \textbf{3-5}$$

Every unit cell of the origami structure has one or more angles. All other parameters of the origami unit cell depend on this angle during the folding process. This angle is called the effective angle. The effective angle could be a projection or a dihedral angle. The characteristics of the effective angle are: it is the first folding in the folding sequence; all the parameters that characterize the origami unit cell depend mathematically on this angle; and when it is a dihedral angle, it should not have inverse folding of the edges.

From the above characteristics of the effective angle, the angle γ_m can be chosen to be the effective angle of the unit cell of the Miura origami structure. All the parameters of the unit cell such as length, width, and height are calculated using

equations 3-1, 3-2 and 3-3 and by assuming the value of γ_m to be between 180° (unfolding situation) to 0° (complete folding situation) to calculate the value of β_m from the equation below:

$$\boldsymbol{\beta_m = 2\left[\tan^{-1}\left(\sqrt{\frac{1-\cos\gamma_m}{2\cot^2\theta_m}}\right)\right]} \qquad \textbf{3-6}$$

Figure 3.5 shows the values of length (X_{fm}), width (Y_{fm}) and hight (h_m) when the value of effective angle γ_m changes from 180° to 0° for the unit cell which has the dimensions a_m =15 mm, b_m =21.21mm and θ_m =45°.

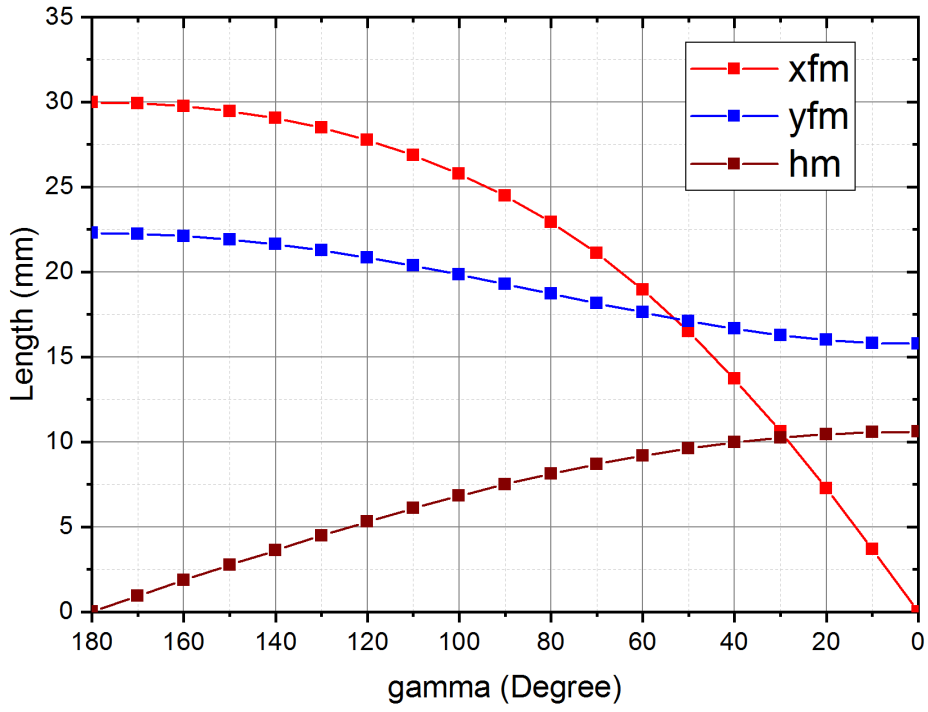

Figure 3.5 The length, width and height of unit cell of Miura origami when the value of effective angle γ_m changes from 180° to 0°.

To describe the whole structure of Miura origami, the numbers of vertices in x and y directions are taken into account. Imagine that the structure of the Miura origami is put in an imaginary box, see Figure 3.6. The dimensions of the whole Miura is then given by:

$$L_m = (n_1 - 1) b_m \sin\left(\beta_m / 2\right) \quad \text{3-7}$$

$$W_m = (n_2 - 1) a_m \frac{\cos\theta_m}{\cos\left(\beta_m / 2\right)} + b_m \cos\left(\beta_m / 2\right) \quad \text{3-8}$$

$$H_m = \frac{a_m \sqrt{\sin^2\theta_m - \sin^2\left(\beta_m / 2\right)}}{\cos\left(\beta_m / 2\right)} \quad \text{3-9}$$

Where n_1 is the number of vertices in the x-direction and n_2 is the number of vertices in the y-direction. The overall volume of Miura origami in folded state is given by

$$V_m = L_m \times H_m \times W_m \quad \text{3-10}$$

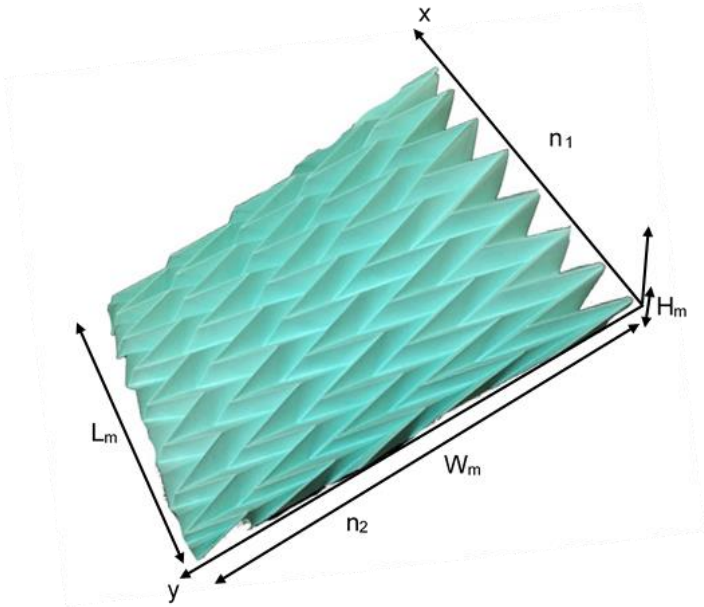

Figure 3.6 Miura origami in its folded state with n_1 vertices in x direction and n_2 vertices in y direction.

The important behaviour of this structure is that the Miura origami can be contracted in x and y directions at the same time. This leads to a common belief that the Poisson's ratio of Miura origami can be a negative value due to intuitive observation and as testified by some theoretical studies using the unit cell [70]. Recently, there is a new study using the size of a whole Miura origami instead of using the unit cell [69]. This study finds that the Poisson's ratio of Miura origami could be negative or positive depending on the combined parameter $(n_2 - 1)\eta \cos\theta_m$ where $\eta = {}^{a_m}/_{b_m}$

In conclusion, the Miura origami has an ability to contract and extend in both directions with negative and positive Poisson's ratio that depends on its constant parameters.

3.3.2 Origami Ball

The Origami Ball is a periodic structure which contains many rigid triangles faces that create the geometry of the origami ball sheet. The triangle faces are linked together by edges that represent the crease lines in the crease pattern. These edges are folded into mountain and valley creases to produce the final shape of the origami ball. Figure 3.7 shows the crease pattern of the origami ball and its final shape after folding.

The origami ball structure can be divided into many unit cells. Every unit cell has six isosceles triangles which are connected at their heads to create a square shape. This square unit cell folded into two mountain creases and four valley creases to create one folded element of the origami ball. Figure 3.8 shows one element of the origami ball before and after folding.

The unit cell of origami ball has a square shape with the length a_b. Therefore, the constant parameter is just the length a_b and all other parameters are variables. The variable parameters are, the side folding distances x_{fr} , x_{fl} , the width folding distances y_{fr} , y_{fl} , and the height h_b. all these parameters depends on the two dihedral angles γ_{br} , γ_{bl} , and the projection angle α_b . the variable parameters are determined as follows:

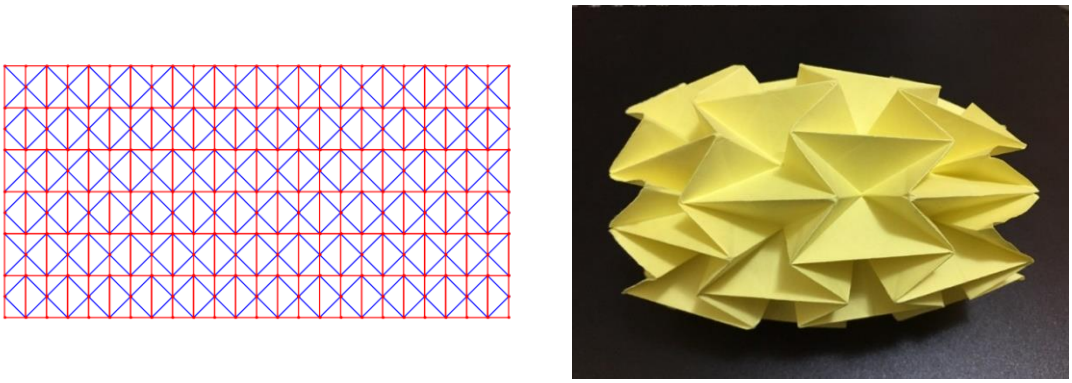

(a) (b)

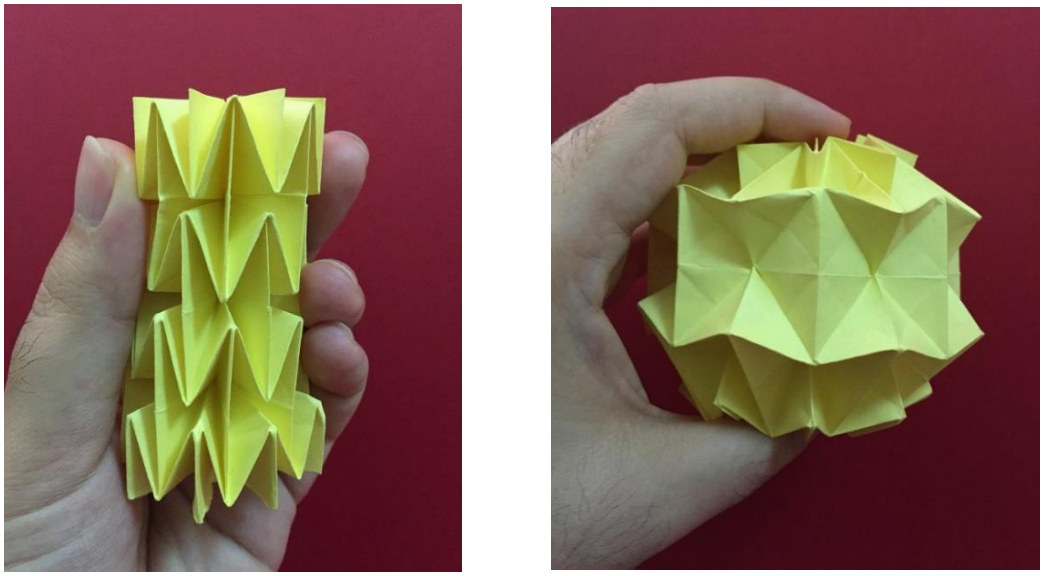

(c) (d)

Figure 3.7 The crease pattern of the Origami Ball (Waterbomb) and its final shape after folding. (a) Crease pattern (b) Origami ball in a wheel shape (c) Origami ball in a cylindrical shape (d) Origami ball in a spherical shape.

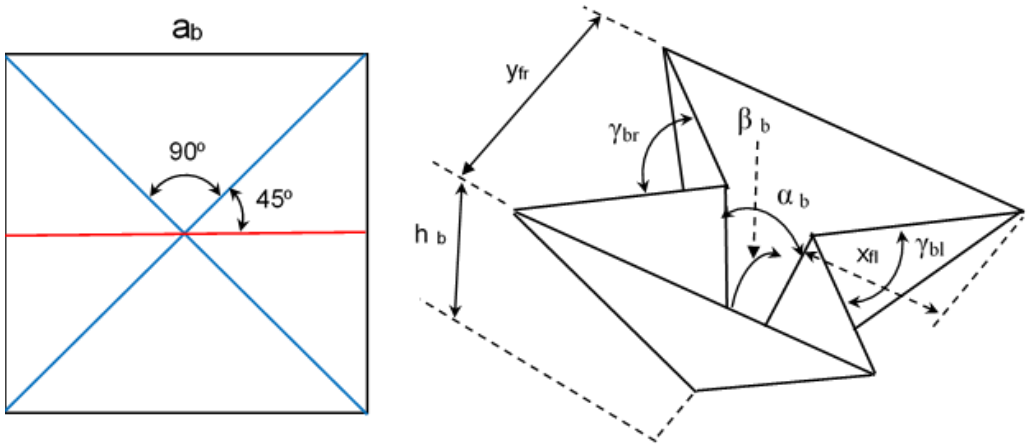

Figure 3.8 Unit cell of Origami Ball. Colors represents crease as mountain (red) or valley (blue).

$$x_{fr} = \frac{a_b}{2}\cos\left(\frac{\gamma_{br}}{2}\right)\cos\left(\frac{\alpha_b}{2}\right) \quad \textbf{3-11}$$

$$x_{fl} = \frac{a_b}{2}\cos\left(\frac{\gamma_{bl}}{2}\right)\cos\left(\frac{\alpha_b}{2}\right) \quad \textbf{3-12}$$

$$y_{fr} = a_b \sin\left(\frac{\gamma_{br}}{2}\right) \quad \textbf{3-13}$$

$$y_{fl} = a_b \sin\left(\frac{\gamma_{bl}}{2}\right) \quad \textbf{3-14}$$

$$h_b = \frac{a_b}{2}\cos\left(\frac{\alpha_b}{2}\right) \quad \textbf{3-15}$$

The relationship between the projection angle and dihedral angles are as follows:

$$\sec\left(\frac{\alpha_b}{2}\right) - \tan\left(\frac{\alpha_b}{2}\right) = \frac{1}{2}\left(\cos\left(\frac{\gamma_{br}}{2}\right) + \cos\left(\frac{\gamma_{bl}}{2}\right)\right) \quad \textbf{3-16}$$

At special case (when $\gamma_{br}=\gamma_{bl}$):

$$\cos\left(\frac{\gamma_b}{2}\right) = \sec\left(\frac{\alpha_b}{2}\right) - \tan\left(\frac{\alpha_b}{2}\right) \quad \textbf{3-17}$$

From equation (3-17) it is clear that the effective angle(when $\gamma_{br}=\gamma_{bl}$) is α_b. But in the general situation, the effective angles are γ_{br} and γ_{bl}. As it is seen in Figure 3.7, the overall volume of the origami ball structure could be a cylindrical or spherical shape. When the origami ball folded to form a cylindrical shape, the radius of this cylinder is equal to $a_b/2$. And when it is extended to form a spherical shape the radius can be calculated using the equation:

$$R_b = \frac{m\, y_f}{2\pi} \quad \textbf{3-18}$$

Where m is the number of unit cells at the circumference of origami ball. y_f is calculated at the middle of the origami ball where $y_{fr} = y_{fl}$ in that place.

The essential unique property of the origami ball is the transformation from the cylindrical to the spherical shape during the folding process. This unique property can be used in many robot applications such as morphing robots and worm-like robots.

3.4 Modular Origami: Twisted Tower

A Twisted tower is made of identical origami segments which are linked in an octagonal way and stacked to from a tower. Every octagon pattern is made up of 16 individual origami sections which have been folded jointly. Any number of layers can be added to a form a tower with a desired value and stroke.

Kinematics of the twisted tower offers amazing properties, such as a high axial stiffness and low bending stiffness due to the fact that the paper bends simply but barely stretches. Therefore, the structure develops, rigid body like, motions which allow us to utilize conventional rigid body kinematics with the addition of physical constraints due to paper structure limitations and thickness. One more interesting property of the twisted tower is that the diameter of the framework doesn't change while contracted or extended [71]. See Figure 3.9.

To understand the differences between the twisted tower and tessellation origami structures see Table 3.1. The table has information about the structure, behaviour, and effective angle for all previous origami structures.

Table 3.1 Specifications of origami structures.

Structure	No. of Sheets	motion	No. of Effective angles	Overall shape
Miura origami	one	contraction and extension in both x and y directions	One	Cuboid (variable length, width, and height)
Origami Ball	one	morphing	One or Two	Cylindrical and Spherical (variable radius)
Twisted tower	Segment of 16 pieces	Twisting	none	Cylindrical (variable height)

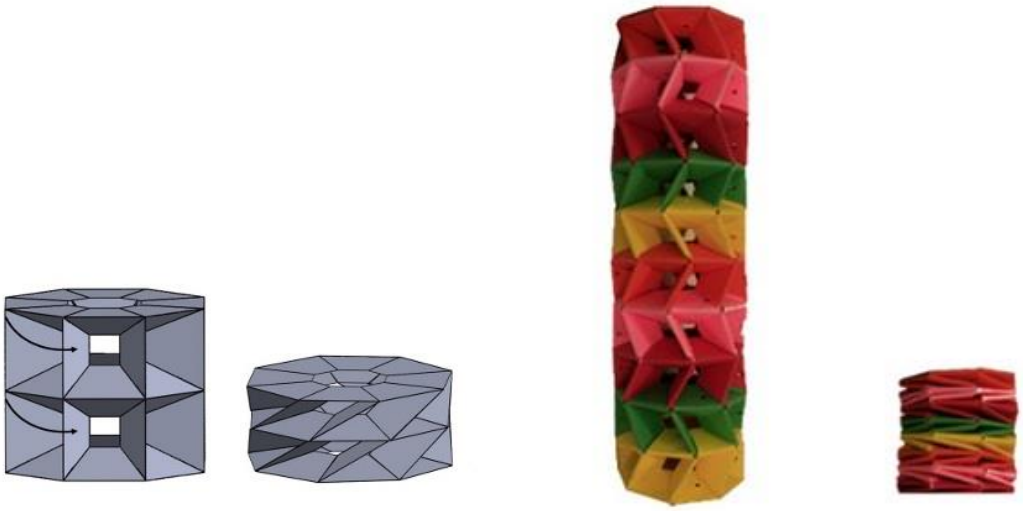

(a) (b) (c) (d)

Figure 3.9 The final shape of Twisted Tower Modular Origami (a) two sections when extended (b) two sections when contracted (c) assembled tower when extended, and (d) assembled tower when fully contracted.

3.5 Mechanical Uses of Origami

Origami structures have many properties that are considered to make many benefits to the mechanical engineering field. The ability to construct a 3D structure from the 2D sheet can make huge progress in the manufacturing field. Furthermore, the folding-unfolding process predicts many types of motions that are useful for mechanical engineering applications. There are many examples of using origami in mechanical engineering such as; some types of solar panels, some folding parts in cars body and to reinforce some sandwich panels. Recently, Sunshields for space photogrammetry is built using origami [72].

The use of origami structure in the robotic field is still in the beginning, and it needs more study to develop. The more important aspects that are required in origami structure to use as a robot are the fabrication by folding (self-folding structure), locomotion with fold/unfolding process, and structures that have a great ability for manipulation. By studying these aspects of origami structures, many types of robots can be created and fabricated. In the next sections, there are more details about that.

3.6 Structures for Self-Folding

When origami is used to build a self-folding structure, it is required to identify the specifications of the folding structure and the ability of the origami model to be a self-folding structure. The specifications of the folding structure depend on the function of this structure. The function could be exploration; search and rescue or a minimally invasive task. When choosing an origami structure that could operate these types of tasks, it is required to study the crease pattern of this origami structure. The most important point for the self-folding crease pattern is that it should be a continuous sheet pattern. This means that it does not have any requirement to stick two pieces together. This property can be found in a Tessellation origami structure such as the Miura origami or the origami ball (waterbomb). Therefore; it is impossible to use a twisted tower as a self-folding structure.

The sequence of the folding process should be considered when designing the self-folding origami structure. The structure that is required to fold all its creases at the same time during the folding process is more stable to be selected as a self-folding structure. The origami structure, where the sequence procedure during the folding process requires a more complicated actuation system compared with the simple origami structure where the creases are folded at the same time. Furthermore, the number of effective angles in the unit cell of the origami structure affects the number of actuators that will be used to activate the self-folding origami structure.

The last property of an origami structure that affects its self-folding ability is the effect of the unit cell on another unit cell. This effect consists of the weight and the forces induced from the folding process. Moreover, the force and behaviour, that is calculated for the unit cell cannot be the same for the whole structure. The behaviour of the whole self-folding structure might be calculated after investigation of all unit cell types that have been used to build the structure. Furthermore, the accurate approach to find the behaviour of self-folding origami structure is by performing empirical test of the whole structure.

From the previous discussion, the whole self-folding structure depends on the type of crease pattern of a continuous sheet: the sequence of folding; the number of effective angles and the forces induced during the folding process. These conditions make the choice of the self-folding structure more complicated to reach a simple fabrication structure. It is clear that the Tessellation origami such as the Miura and the origami ball (Waterbomb) are more suitable to be considered as a self-folding structure. Therefore, to test the self -folding, it should

be started from a simple structure, which is a box and then try another origami structure that is more complicated.

3.7 Origami Structure for Locomotion

Some of the origami structures can create locomotion activity by using a folding and unfolding process. The origami structures that can produce motion during the folding- unfolding process are the twisting tower and the origami ball. All motion processes are produced in the crease lines (the hinge). A simplified origami locomotion can be represented by the movement of a simple strip. The strip consists of some elements with simple one DOF hinges between them. The Figure 3.10 shows a simple strip with ten elements and nine revolute joints between the elements. This strip is modelled using V-Rep software program.

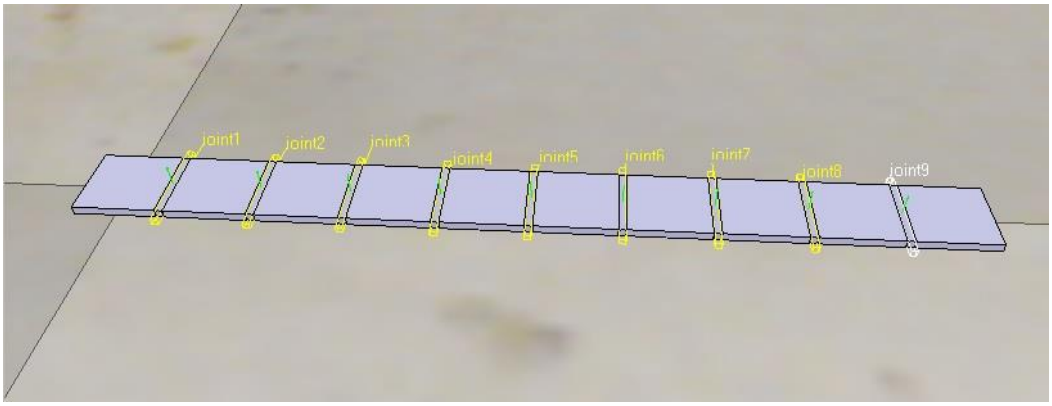

Figure 3.10 The V-Rep model of simple strip with ten elements and nine revolute joints between the elements.

The V-rep software program was used to study the ability of worm-like locomotion with a simple strip. This strip represents a simple origami structure that has nine creases. This following study clarify the locomotion that is produced from the folding and unfolding process. Four wave styles are examined on the V-rep strip model. An active revolute joint was put in every crease and then a code, that has the activation angles and their sequences, was written. The first wave style is a constant angle activation with angles ($+90^o$,-90^o) at all joints, see Figure 3.11. The second style is a wave that starts from ($+90^o$,-90^o) goes to ($+30^o$,-30^o) and repeats the sequence, see Figure 3.12. The third style is similar to the second one but has a 0^o activation angle and inverse the wave sequence, see Figure 3.13. The last one is starting from $+30^o$ for three joints reach to 0^o

angles for one joint and -30º for another three joints, then repeats the sequence, see Figure 3.14.

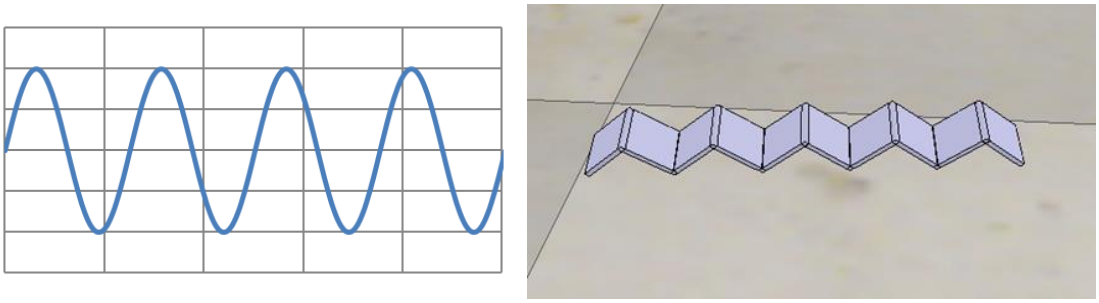

Figure 3.11 The first wave style and the shape of V-rep model simulation.

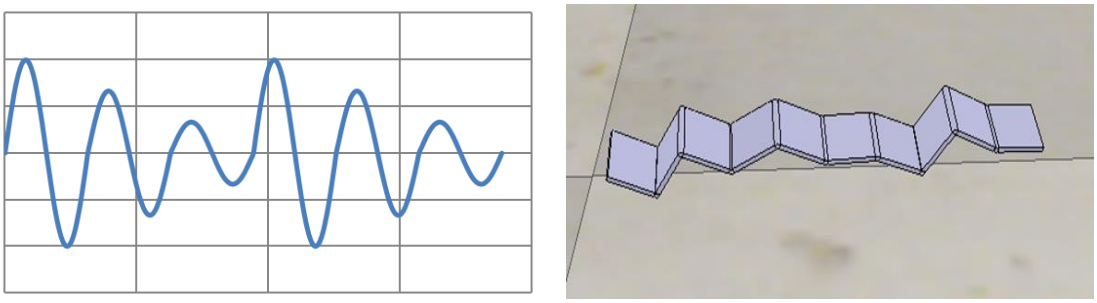

Figure 3.12 The second wave style and the shape of V-rep model simulation.

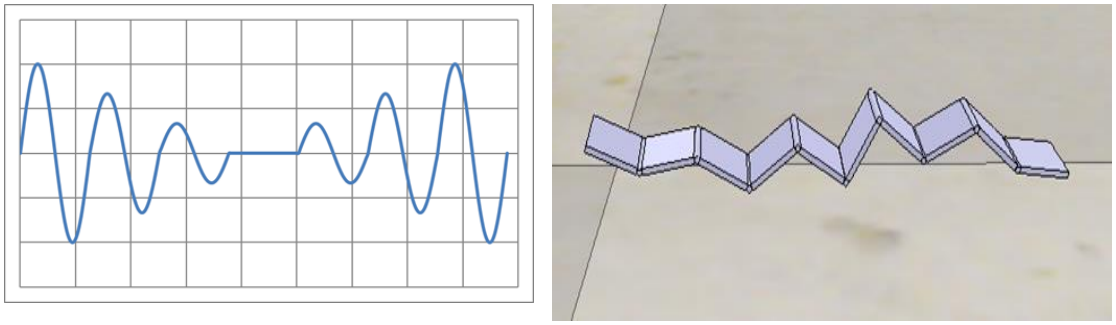

Figure 3.13 The third wave style and the shape of V-rep model simulation.

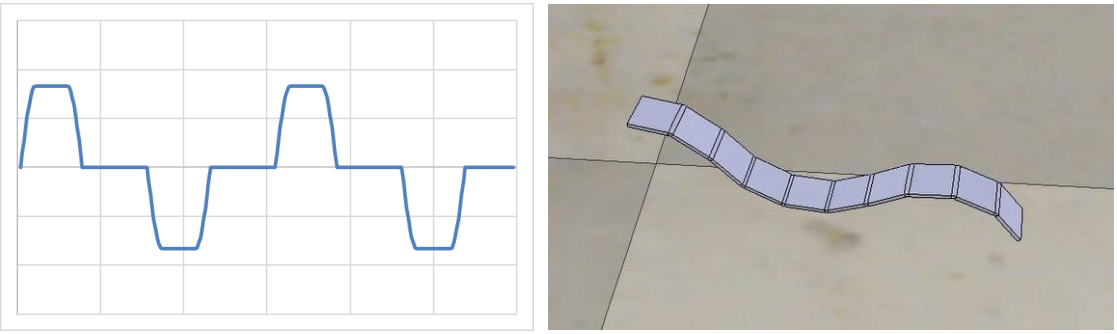

Figure 3.14 The fourth wave style and the shape of V-rep model simulation.

The simulation program V-rep shows that the best sequence is the fourth. It is the best one that has stable worm-like locomotion when it was examined. Table 3.2 indicates the steps of joints activation and the values of the angles during these steps. This sequence can be applied to more complicated origami structures to provide worm-like locomotion for these structures.

Table 3.2 The sequence steps of joints activation angles of the fourth wave style.

joints		Joint1	Joint2	Joint3	Joint4	Joint5	Joint6	Joint7	Joint8	Joint9
Activation angles	Step1	30º	30º	0º	-30º	-30º	-30º	0º	30º	30º
	Step2	30º	30º	30º	0º	-30º	-30º	-30º	0º	30º
	Step3	0º	30º	30º	30º	0º	-30º	-30º	-30º	0º
	Step4	-30º	0º	30º	30º	30º	0º	-30º	-30º	-30º
	Step5	-30º	-30º	0º	30º	30º	30º	0º	-30º	-30º
	Step6	-30º	-30º	-30º	0º	30º	30º	30º	0º	-30º
	Step7	0º	-30º	-30º	-30º	0º	30º	30º	30º	0º
	Step8	30º	0º	-30º	-30º	-30º	0º	30º	30º	30º

3.8 Modular Origami Structure for Manipulation

The most important benefit of the study and investigation of different traditional origami structures is to understand the characteristics of their unit cells and use the useful types to build a new structure that has the desired behaviour. A novel kind of origami arm can be obtained from the unique characteristics of the unit cell of the origami ball. The ability to bend that is provided by the unit cell of origami ball in two directions makes this type of unit cell suitable to build a manipulation arm or snake link structure. Four or more unit cells of the origami ball connected in series can provide a bending motion in three directions depending on the value of angles γ_{br} , γ_{bl} and α_b, see Figure 3.8. A V-rep model that has four unit cells of origami ball is used to evaluate the ability to create bending in two directions, see Figure 3.15.

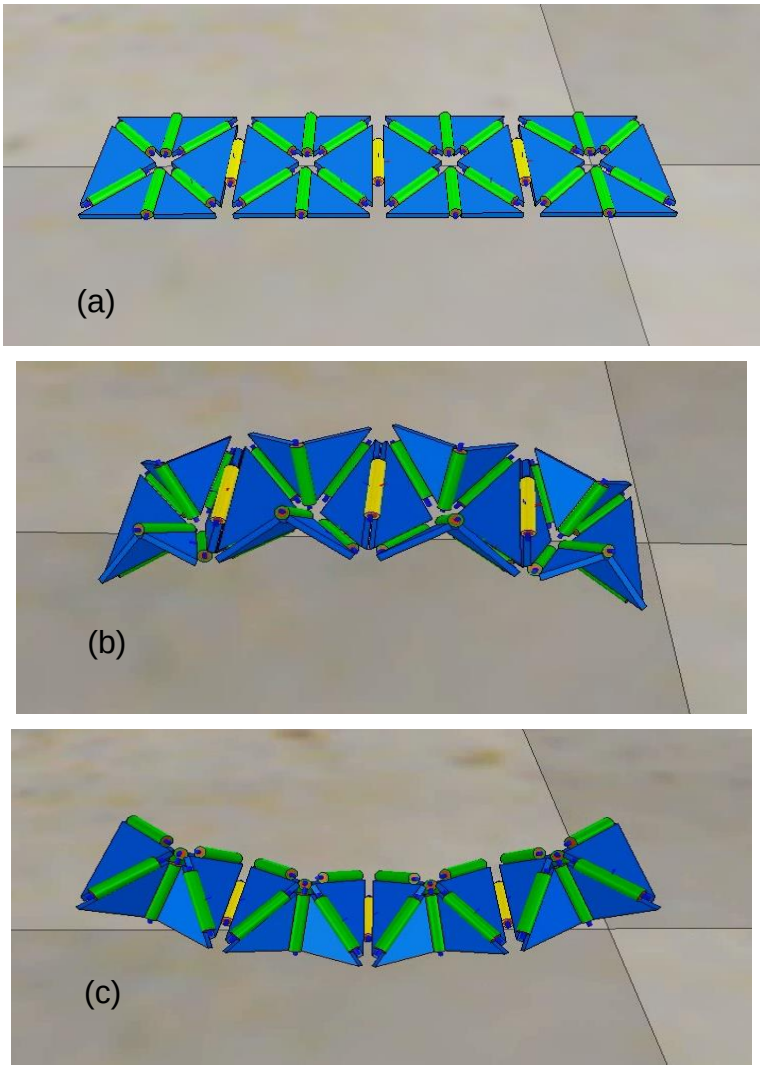

Figure 3.15 The V-rep model with four-unit cells of origami ball in series and its ability to create bending in two directions (a) Flat structure (b) Convex bend (c) Concave bend.

Four-unit cells of origami ball are stacked into a column. This column used as a side of four sides structure which is connected with the top and bottom square pieces of card paper. This structure can bend to four directions because of the flexibility of card paper and the behaviour of the unit cell of an origami ball. See Figure 3.16.

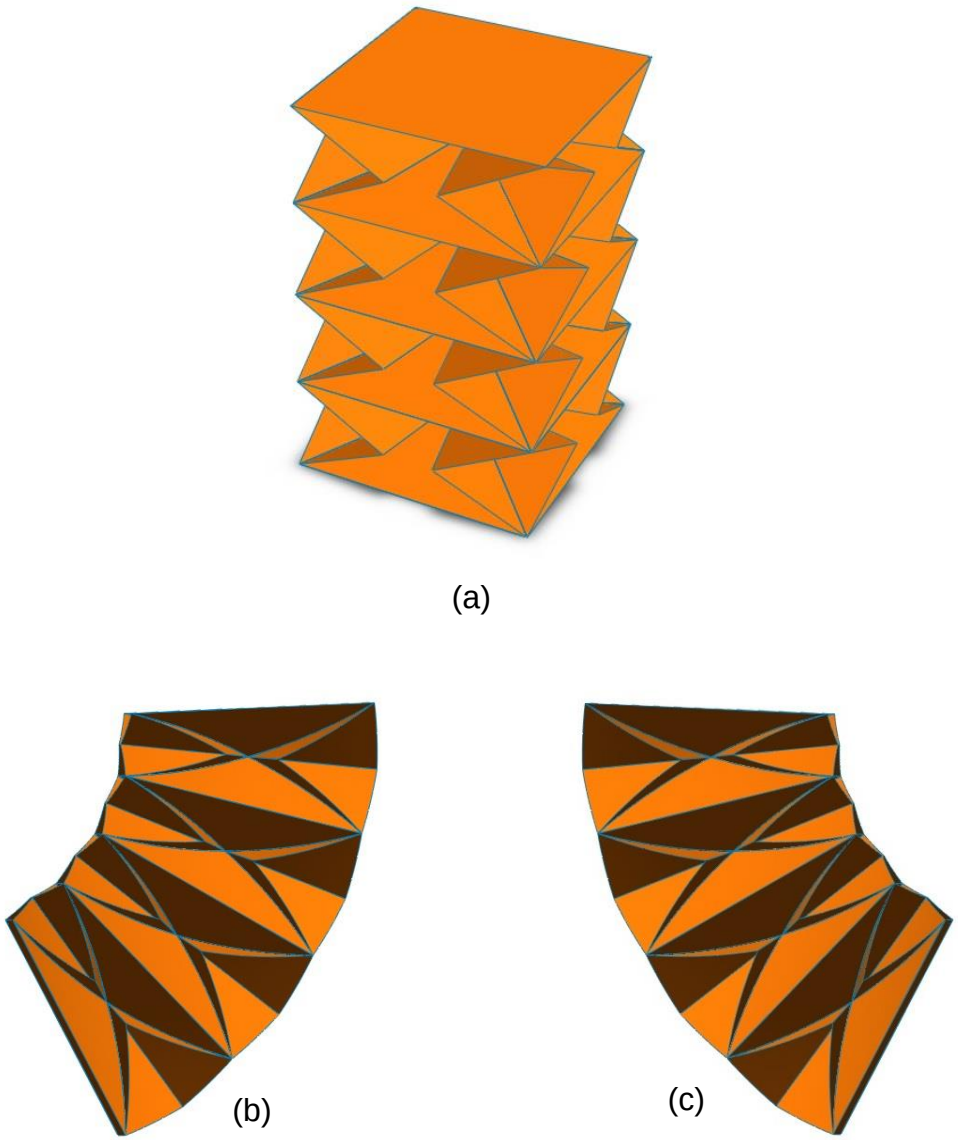

Figure 3.16 The Origami Structure for Manipulation (OSM). (a) The original shape after folding. (b) OSM with a left bend. (c) OSM with a right bend.

Every unit cell in this origami structure for manipulation (OSM) has the same property of the origami ball (Waterbomb) unit cell. The same equations that are used to calculate the parameters (length, width, and height) of the unit cell of origami ball, can be used to calculate the same parameters of this structure. When the two angles γ_1 and γ_2 are known, the length y_{f1} and y_{f2} calculated as:

$$y_{f1} = a_b \sin\left(\frac{\gamma_1}{2}\right) \quad \textbf{3-19}$$

$$y_{f2} = a_b \sin\left(\frac{\gamma_2}{2}\right) \quad \textbf{3-20}$$

These equations are required to describe the bending motion and the position of the end tip of the OSM structure. The position that is reached after bending motion can be calculated using the radius of curvature and the angle of the arc that is created from the bending motion. The radius of curvature and the angle are determined after y_{f1} and y_{f2} are calculated, see Figure 3.17. When calculating the radius of curvature and angle for one-unit cell, these equations are used:

$$R_o = \frac{a_b\ y_{f1}}{(y_{f2} - y_{f1})} \quad \textbf{3-21}$$

$$\varphi_{oi} = \frac{y_{f1}}{R_o} \quad \textbf{3-22}$$

The equation for calculating the overall angle is as follows:

$$\varphi_o = \frac{n\ \ y_{f1}}{R_o} \quad \textbf{3-23}$$

Where n is the number of unit cells in one side of the OSM structure.

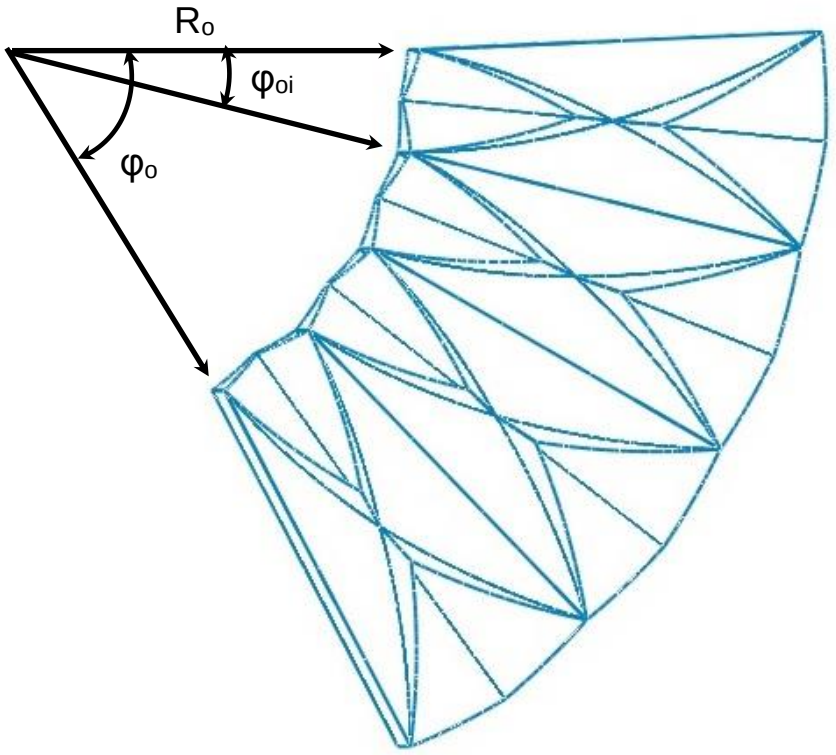

Figure 3.17 The Radius of curvature R_o and the angle φ_o of the arc that is created from the bending motion of OSM.

The kinematics of the OSM structure provides interesting properties, such as the high ability of contractions and low bending stiffness. These properties make the OSM structure to be the potential solution for the structures that are used in arm manipulation robots and snake robots.

3.9 Conclusions

In this chapter, the origami context is clarified. The basic structures that origami employs to create different shapes after folding are described. Three origami structures (Miura, ball and twisted tower) are investigated. The equations to compute the geometry of Miura origami and ball origami are established. The Miura origami structure provides excellent property, which is the ability of contraction and extraction in two directions. And the origami ball provides the ability to morph the shape from cylinder to sphere. These properties made these origami structures suitable to use in the mechanical engineering field.

Furthermore, the features of these two origami structures made them suitable to use for the self-folding structure. The unit cell of Origami ball was used as an element to construct a new type of origami structure. This novel OSM origami structure has great manipulation ability. It provides bend motion in four directions and contraction motion.

A clear study in design the hinges and choosing the material that could fabricate these types of flexure hinges are required to fabricate the self-folding structure and the origami structure for manipulation.

Chapter 4 HINGE DESIGN

4.1 Introduction

In the previous chapter, the principles of the origami structure were explored and it was shown that the origami structure consists of two essential parts: the faces and the creases lines. These two parts constitute the crease pattern. Therefore, the mechanical behaviour of the crease lines should be analysed when designing an origami structure.

The deformation of origami structures occurs on the creases lines as these are subjected to the bending moment during the folding process when the origami structure is created from a sheet. These crease lines act as hinges between the fixed faces. The first step to design the hinges is analysed the hinge behaviour to calculate all the parameters that affect it during the folding process. The mechanical behaviour of these hinges is calculated using the principle of beams. The essential parameter that results from the study of hinge behaviour is the maximum strain on the hinge. This maximum strain value depends on the dimensions of the hinge and the angle of fold.

The second step to design the hinge is to choose an appropriate material that provides the flexibility required for the folding process. This material should be soft and have a suitable fatigue limit to prevent failure during the cyclic folding and unfolding process. Therefore, three experimental tests were conducted for this material to calculate its mechanical properties. In addition, the amount of force that is required to fold the hinge was calculated. The amount of force required to fold the hinge provides an indication of the specification of actuators that could be used to provide this force.

In this chapter, the behaviour of the hinge is analysed and the parameters that affect the folding structures during the folding process are calculated. A 3D printed soft material is tested for use as a hinge material and the results are discussed. In addition, the hinge in folding structures fabricated by laser cutting is described. Finally, the properties of the Kapton film material, which is used as a hinge in the folding structures fabrication, are compared with the other approaches.

4.2 Types of Hinges

The origami folding structure creates a hinge at a crease line from the same material that constitutes the sheet material. Therefore, this research focuses on a flexure hinge that is made from flexible material. A flexure hinge is a mechanical element that connects two rigid members and provides the relative rotation between them through bending (flexing) instead of a traditional rotational joint [73].

The different methods of contact between the flexure hinge and the two rigid bodies creates different types of hinges. As is seen in Figure 4.1, four types of hinges are created by different ways of connecting the flexible material with the rigid material. The different positions of the flexible material (which is in orange color) make different types of hinges. In the first type, the flexible material and solid material have the same thickness and the flexible material has two connection surfaces. In the second type, the flexible material forms a pad for the two sides of the solid material. In this type, the connection surfaces are bigger than the connection surfaces in the first type. The third and fourth types are like a sandwich, but one with the flexible material in the middle, while the other sandwiches the solid material in the middle.

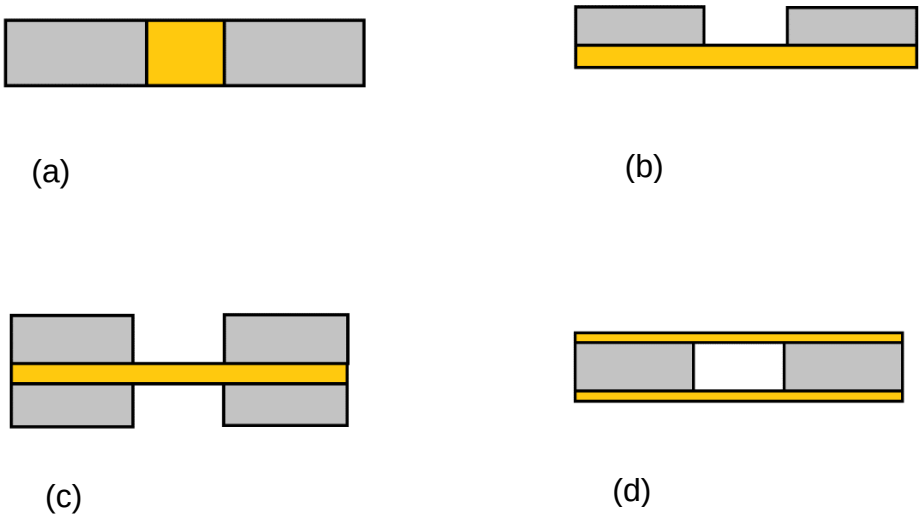

Figure 4.1 Types of hinges created from connecting the flexible material with the rigid material (a) flexible material same thickness as solid material (b) solid material attached flexible material (c) flexible material sandwiched between solid materials (d) solid material sandwiched between flexible materials.

The bending beam theory can be used in the analysis of the behavior of these types of hinges by assuming the flexible material to be a beam. This bending beam theory can solve for the moment and shear as:

$$\boldsymbol{M = EI\frac{d^2v}{dx^2}} \qquad \textbf{4-1}$$

$$\boldsymbol{V = EI\ \frac{d^3v}{dx^3}} \qquad \textbf{4-2}$$

Where M is the bending moment; V is the transverse shearing force; ν is the transverse deflection of the centroid axis of the beam; *EI* is the flexural rigidity; and x is the longitudinal coordinate measured from the left end side of the beam. In the next section, hinges are analysed with a simplified moment and shear equations.

4.3 Hinge analysis

It is important that the hinge does not fail during use. It could fail by the effect of fatigue or overloaded stress. These two parameters depend on the amount of strain. The hinge is assumed to behave as a beam when calculating the strain. From the principle of beams [74], the strain equation is:

$$\boldsymbol{\varepsilon_x = \pm \frac{y}{R}} \qquad \textbf{4-3}$$

Where R is the radius of curvature, and y is the distance from the neutral axis to any point inside the beam thickness. The plus and minus signs refer to the tension and compression strain. See Figure 4.2 that shows the relationship between the radius of curvature and strain for different thickness. The stress is calculated from the axial stress equation:

$$\boldsymbol{\sigma_x = -\frac{My}{I}} \qquad \textbf{4-4}$$

Where M is the bending moment at the location of interest along the beam's length. I is the centroidal moment of inertia of the beam's cross section, and y is the distance from the beam's neutral axis to the point of interest along the height of the cross section. The negative sign indicates that a positive moment will result in a compressive stress above the neutral axis.

These equations calculate the strain and stress in a single crease when considered as a simple hinge (or simple beam).

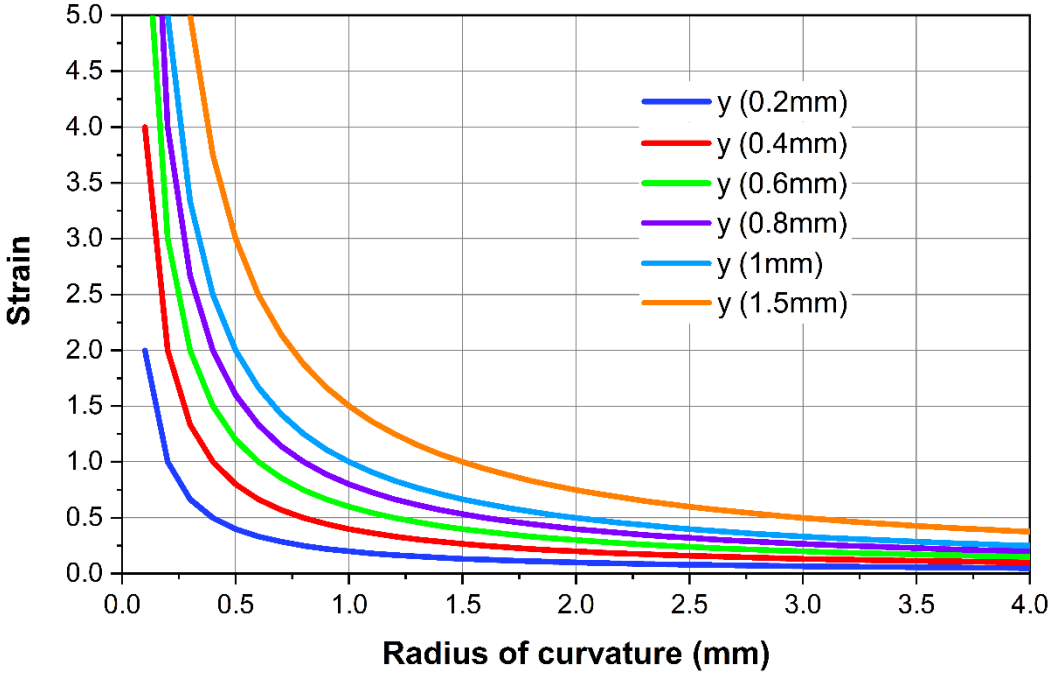

Figure 4.2 The relationship between the radius of curvature and strain for different beam thickness.

When the crease line is analysed for any material, it is assumed to represent a hinge which is connected by two sides of solid material. This hinge has two effective dimensions which are the width b and the thickness t, see Figure 4.3. As described in chapter three, the crease has a radius of curvature R and folding angle θ_i when it is bent. From these parameters, the strain at any point on the edge of two folding faces can be calculated as:

$$\boldsymbol{\varepsilon = \frac{\Delta l}{l} = \frac{r\theta_i - b}{b}} \qquad \textbf{4-5}$$

Where r is the variable radius and its value: $R \leq r \leq R + t$

The maximum fold occurs when the two inner sides of a hinge touch. In this special case, the radius is assumed to be equal to the thickness and the maximum strain on the outer surface of the hinge, calculated as:

$$\boldsymbol{\varepsilon_{max} = \frac{t \times \pi}{b}} \qquad \textbf{4-6}$$

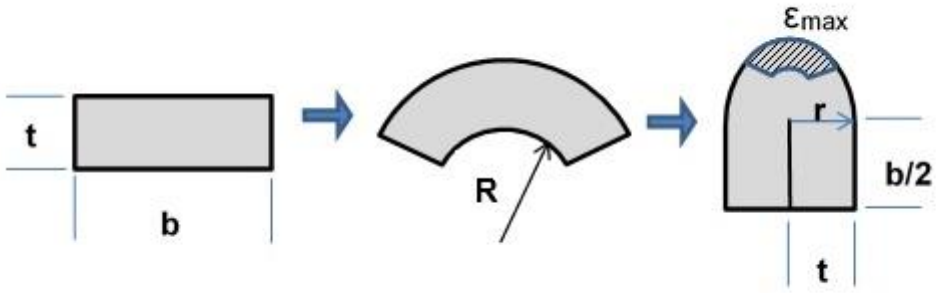

Figure 4.3 Simple sketch of a hinge with width b and thickness t. Starting from flat shape until it is completely folded.

It is seen from equation (4-6) that the maximum strain on the crease tip is directly proportional to the thickness and inversely proportional to the width. For example, if it is a square hinge (i.e. b=t) the maximum strain is π.

To clarify the relation between the maximum strain and the two hinge parameters (b and t), see Table 4.1. In this table, the maximum strain (ε_{max}) decreases when the value of width (b) increases. On the other hand, the maximum strain increases when the value of thickness increases for the same value of b. From this table, it is clear that any design should carefully choose the values of b and t to not exceed the maximum strain value of the material. At the same time these values should produce hinges that achieve a stable folding structure.

Table 4.1 Relationship between the ε_{max} and hinge parameters (b and t).

b(mm)	1	2	3	4	5	6
ε_{max} (t=1mm)	3.142	1.571	1.047	0.785	0.628	0.524
ε_{max}(t=2mm)	6.283	3.142	2.094	1.571	1.257	1.047

Furthermore, the angle of folding should be taken into account when designing the hinge parameters b and t, as this affects the value of strain. The relationship

between the angle of folding θ_i and the strain ε for the hinge with thickness (t=1mm) for four width values is shown in Figure 4.4.

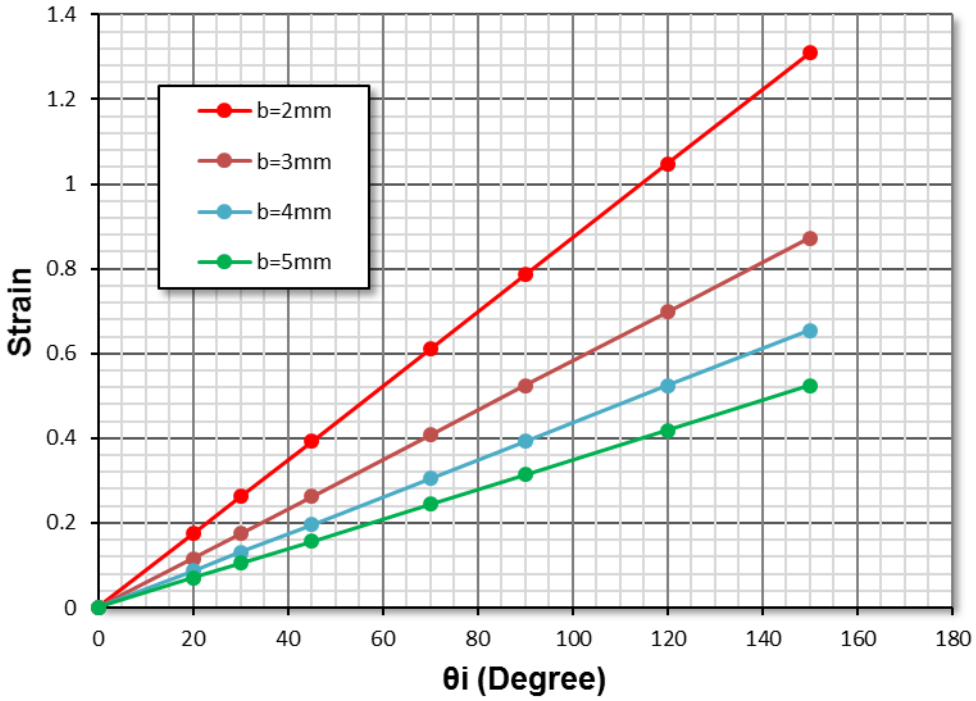

Figure 4.4 The relationship between the angle of folding θi and the strain ε for different hinge width (Hinge thickness t=1mm).

4.4 Materials and Mechanical Tests

To select suitable material for a hinge body, this work has been performed experimentally for different materials. The material must fulfil two main conditions: Firstly, it should be flexible and have the ability to bend until completely folded. Secondly, it should have the mechanical properties that prevent it from failure during the folding process. In other words, The material should have a suitable tensile stress, shear stress, and fatigue limit. These mechanical properties are measured from experimental tests which demonstrate the behaviour of the materials. The hinge material requires several mechanical tests such as tensile test, bending test and fatigue test.

The tensile test machine 'Instron 3369' was used for two test types: the tensile test and the bending test. The Instron 3369 has the capacity of 50 KN with the

vertical test space 1193 mm, see Figure 4.5. The maximum tensile speed of 500 mm/min. Control of the testing system is carried out via Instron Bluehill software. The Bluehill software, inputs a set of defined parameters that the system uses to run tests. The parameters, which are required before starting the test, are the speed of test and the maximum elongation. Bluehill analyses the test data and produces calculated results in an excel file. The software has the ability to calibrate the position and the load before starting the test. The grippers of machine are replaced with three-point bending grippers when operating the bending test.

Figure 4.5 The tensile test machine ‘Instron 3369’.

The Instron Electro-Puls E10000 machine was used to test the fatigue limit. It has ±10kN dynamic linear load capacity and ±100 Nm dynamic torque capacity. The vertical test space is ±60mm. see Figure 4.6. Control of the testing system was carried out via the Instron Wave Matrix software. In Wave Matrix software, the test inputs a file that contains a set of defined parameters that the system uses to run tests. The essential parameters, which are required before starting the test, are the frequency or the speed of test, the linear stroke elongation, and the maximum number of cycles. The Wave Matrix software produces the

calculated results in an excel file. The software has the ability to calibrate the position and the load before starting the test, see Figure 4.6.

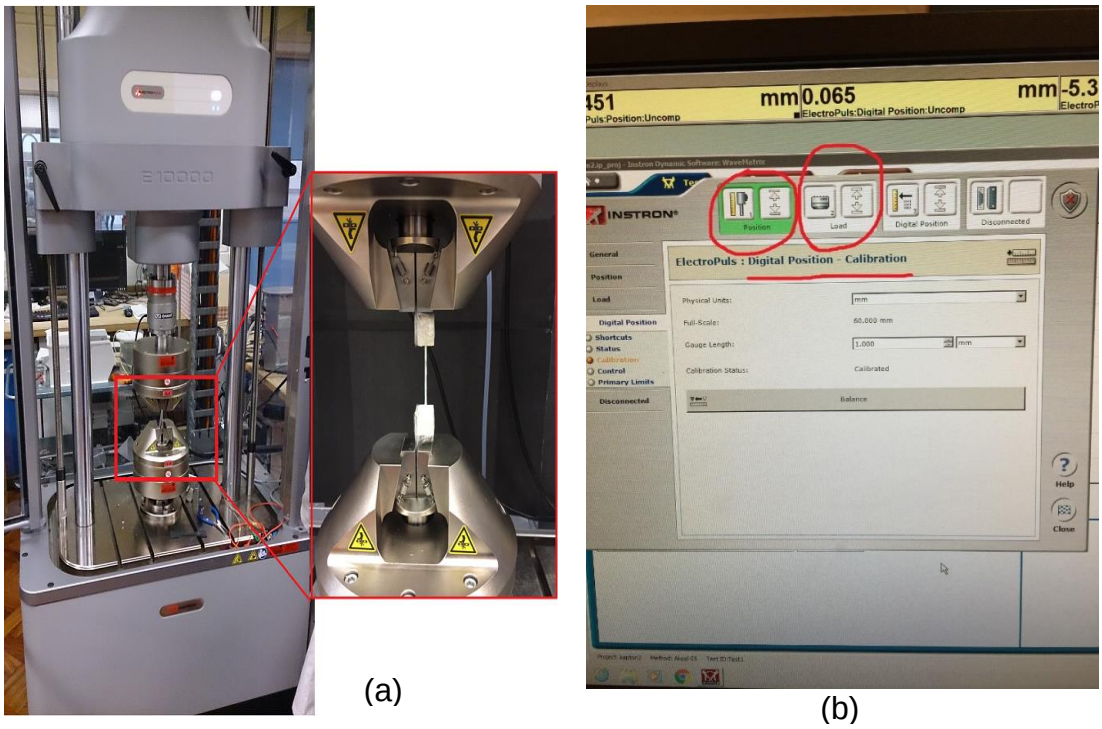

(a) (b)

Figure 4.6 (a)The Instron Electro-Puls E10000 dynamic machine. (b) The interface of Wave Matrix software with the position and load calibration options marked in red circles.

4.5 3D Printed materials

As previously discussed, the structure of folding object consists of two essential parts: the faces and the creases. The folding action is provided by the crease, and the faces maintain their solid shape. For this reason, many researchers fabricate the folding structure by using the multilayer approach and laser cutting, as described in chapter two. The crease lines are cut in the solid layers leaving the soft layer to work as a hinge.

In this research a 3D printer is used to fabricate a folding structure in two types of material. A 3D printer can print two types of different materials at the same time for the same structure by building the faces using solid materials, and the crease lines by using soft material, which provide a large bending ability. Furthermore, these two materials are combined without using any connections

between them. These two types of materials are the Vero for solid faces and Tango plus FLX930 for the soft crease lines. You can see the type of 3D printed materials in Table 4.2. which shows that the rubber like material is the Tango family and rigid materials are Vero family, Vero color, and Vero clear [75].

Table 4.2 Some types of 3D printer materials and their applications [75]

Standard Plastics	Rigid Opaque	Vero™ Family
		Vero Color
	Rigid Transparent	RGD720
		VeroClear™
	Simulated Polypropylene	Durus™
		Endur™
	Rubber	Tango™ Family
Engineering Plastics	Digital ABS™ Green Digital ABS2™ Green	RGD5160-DM RGD5161-DM
	Digital ABS Ivory Digital ABS2 Ivory	RGD5130-DM RGD5131-DM
	High Temperature	RGD525
Medical	Hearing Aids***	
	Rigid, bio-compatible	Clear Bio-compatible MED610
Support	SUP705	
	SUP707	Works with VeroWhitePlus, VeroGray™, VeroBlue™, VeroClear

The soft material at the hinges (crease lines) are subjected to the load directly when the structure folds. Three tests were performed using specimens made from Tango Plus flx930 material to determine the tensile strength limit, fatigue limit and the forces require to fold sheets of different thickness into many folding angles. These results provide explicit material property information to support the designer's decision making when designing an origami robot using Tango Plus material as a hinge.

4.5.1 Tensile Test for Tango Plus

The main reason to perform the tensile test is to calculate the tensile strength which represents the limitation of stress for this material. Although, there are many standards which show the modulus of elasticity and the tensile strength of different materials, not all elastomer materials have tensile strength information especially for the materials used in 3D printers. For this reason, it is important to operate this test for the Tango Plus flx930 to find its limitations for stress and elongation.

Moreover, it is complicated to calculate the modulus of elasticity for elastomer materials analytically, because of many issues such as large deformation response, and non-linearity of the stress-strain curve [76]. Therefore, every new elastomer material should have a particular tensile test to indicate their properties. Although some elastomer properties depend on time due to the hysteresis effect, this test can give suitable indication for these properties.

The tensile test was preformed three times for three different specimens, which had the same shape. The exact dimensions of the specimen shape are shown in Figure 4.7 which were taken from the machine standard. It is seen that the specimen has a cylindrical shape with effective length and area (37.7mm, 39.92 mm^2) respectively. All specimens were printed on an Object-1000 3D printer with the Tango Plus flx930 material in “digital material” mode. The final specimen shape is shown in Figure 4.8.

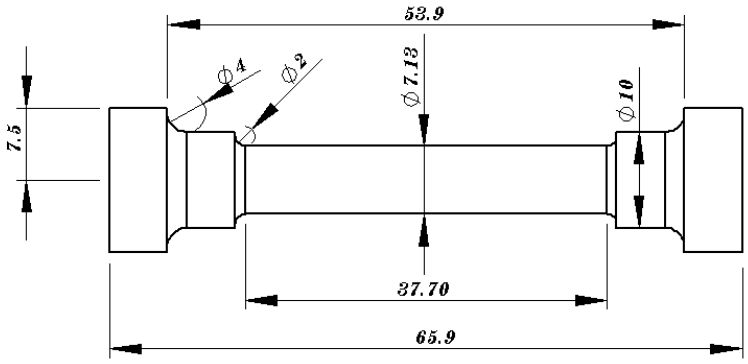

Figure 4.7 An engineering drawing of the tensile test specimens. All measurements given in millimeters.

Figure 4.8 The tensile test specimen made from Tango Plus flx930.

The Instron 3369 tensile machine was used for this test. The tensile test machine was calibrated before starting the test. The test velocity was set at 60 mm/min. After that, the test was operated which took almost two minutes for every specimen. Figure 4.9 shows the tensile test specimen after test.

The machine gives the results of the load and displacement. All specimens show exactly the same behaviour with a few differences in the tensile strength amount. The stress-strain curve can be calculated from the data of load-displacement which was collected from the tensile test machine. It can be determined by using traditional equations of stress and strain which are:

$$\boldsymbol{\sigma = \frac{F}{A_e}} \qquad \textbf{4-7}$$

$$\boldsymbol{\varepsilon = \frac{\Delta L}{L_e}} \qquad \textbf{4-8}$$

Where, A_e and L_e are the effective area and length.

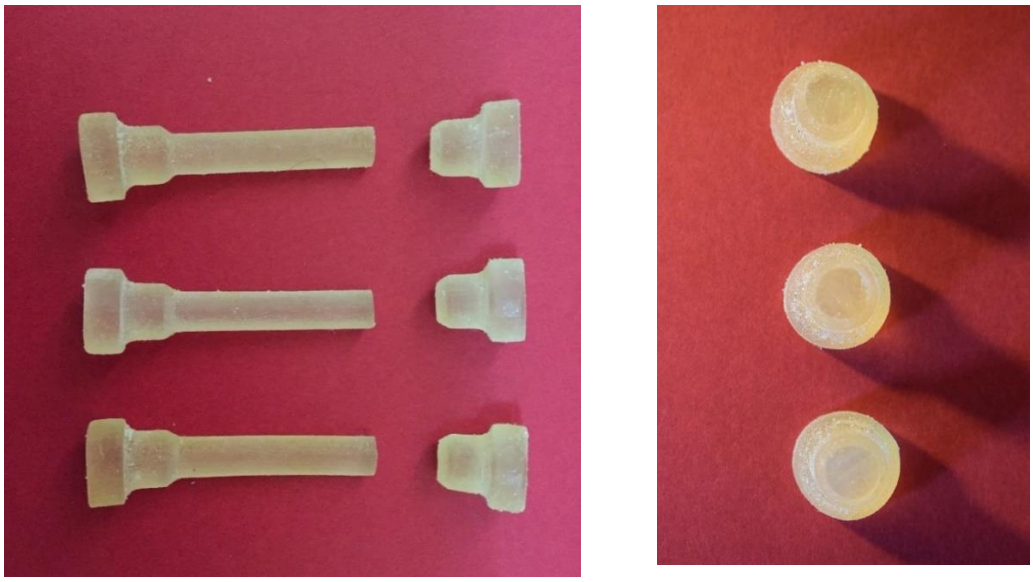

Figure 4.9 The tensile test specimens made from Tango Plus flx930 after test.

The stress-strain curve is shown in Figure 4.10. This figure shows the stress-strain curve for the three specimens, and it is clear that the tensile strength of the first specimen was equal to 0.68 Mpa and the maximum elongation was 260%. For all specimens, the tensile strength range is between 0.63-0.68 Mpa and the maximum elongation range is between 250-260% . The elongation range is close to 170-220% specified in the material data sheet that is given for this material.

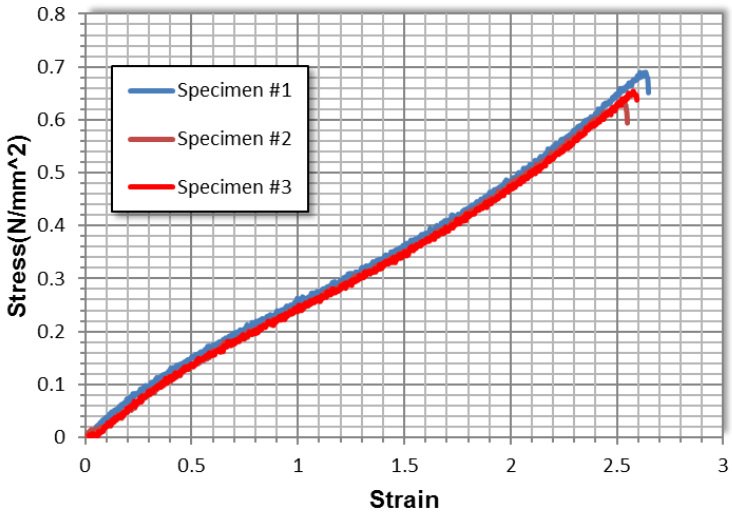

Figure 4.10 The stress-strain curve for Tango Plus flx930.

4.5.2 Bending Test for Tango Plus

The important useful information, which is required from the material behaviour and to support this project, is the amount of force that could fold the sheet made from this material. Therefore, a test was preformed to find the amount of force which is required to fold different thickness of beam through a range of folding angles.

Flat specimens were used for this test which have a beam shape. The dimensions of these specimens were 40mm length and 10mm width in three different thicknesses of 3mm, 5mm, and 7mm. In addition, two types of specimens were used for the 5mm thickness; the first specimen is completely flat, and the second specimen has a notch on both sides in the middle with 1mm radius, see Figure 4.11. The different thickness of specimens were used to explore the relation between the thickness and the folding force. Furthermore, the flat and notched specimens were used to examine the effect of the notch on the folding force. All specimens were printed on an Object-1000 3D printer with the Tango Plus flx930 material in “digital material” mode.

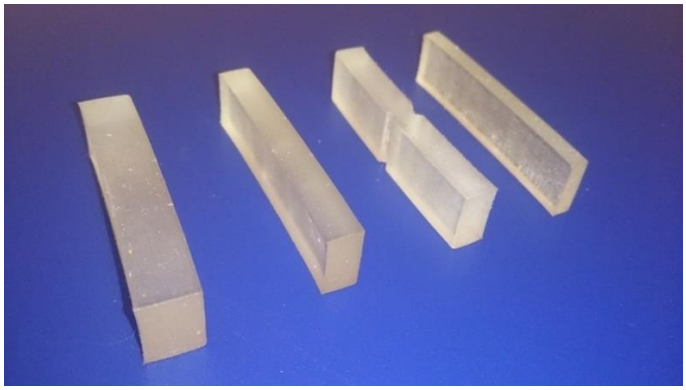

Figure 4.11 The bending test specimens made from Tango Plus flx930.

The machine used for this test was the Instron 3369 tensile machine with the grippers of the three-point bending test. These grippers were used to calculate the material resistance to bending. The middle rod of the gripper was changed from the 6mm wire to a smaller wire of 1mm diameter, to create a sharp folding angle and to enable a smaller radius of curvature in the folding specimen. See Figure 4.12.

The test machine requires the input data of the speed of test and the final displacement to stop. For this situation, the speed of test was 60 mm/min and the final displacement 20mm.

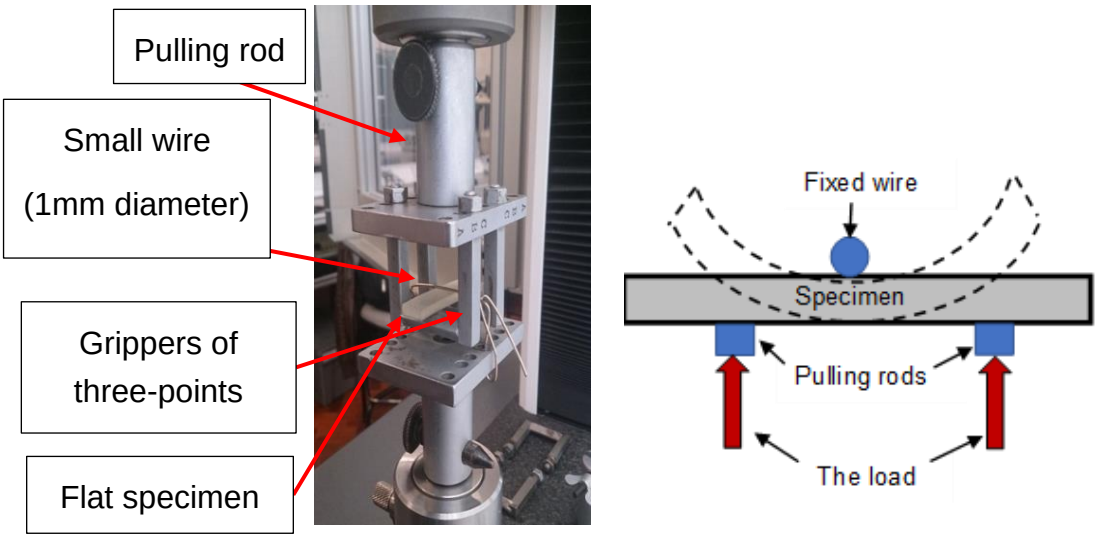

Figure 4.12 Grippers of three-points bending. (a) Photo of the three-point bending gripper. (b) The free-body diagram of the three-point bending gripper.

The test provides the results of force and displacement which were then used to calculate the table of folding angle against the force. When the folding angles were calculated, it was found that there was a drop in force after the angles 105^{o}, 120^{o}, 125^{o} and 135^{o} for the thickness 3mm, 5mm with a notch, 5mm and 7mm respectively. This drop in force was due to the slipping of specimens from gripper rod sides when reaching these angles. The relationship between the folding angles and forces are shown in Figure 4.13 and Figure 4.14 after the slipping zone is cancelled.

Figure 4.13 shows the relationship between the force and angle of folding for three specimens with the same thickness of (5mm). These curves show the accuracy of the test and it is seen that the variation between the specimens results is small.

It is seen from Figure 4.14 that the force increases when the thickness increases. Furthermore, the result for the specimen 3 (5mm thickness with notch) does not decrease the force a lot. Although, it has a 3mm thickness between the notches, its force does not reach the force of specimen 1 (3mm thickness).

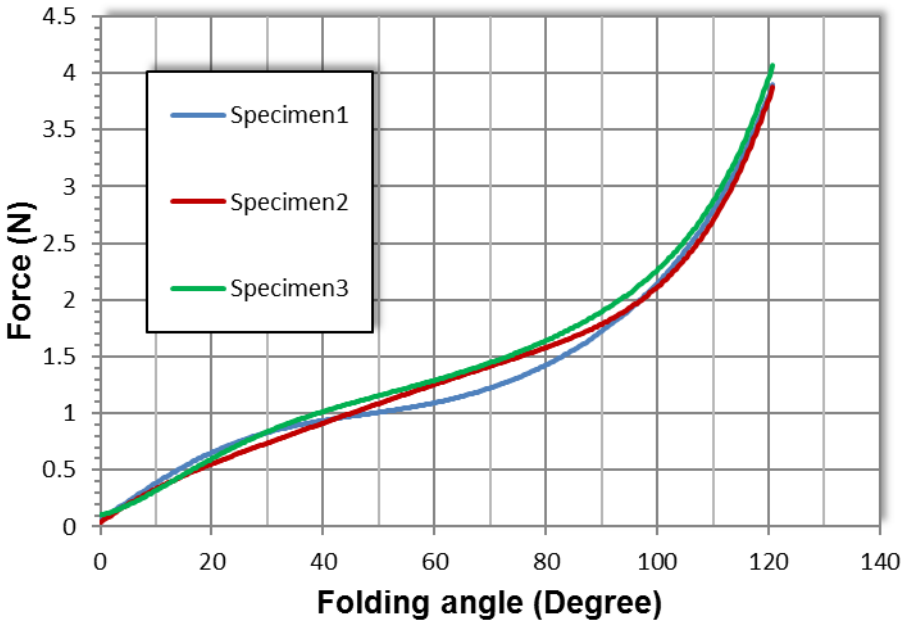

Figure 4.13 The relationship between the force and angle of folding for three specimens (5mm) Thickness made from Tango Plus flx930.

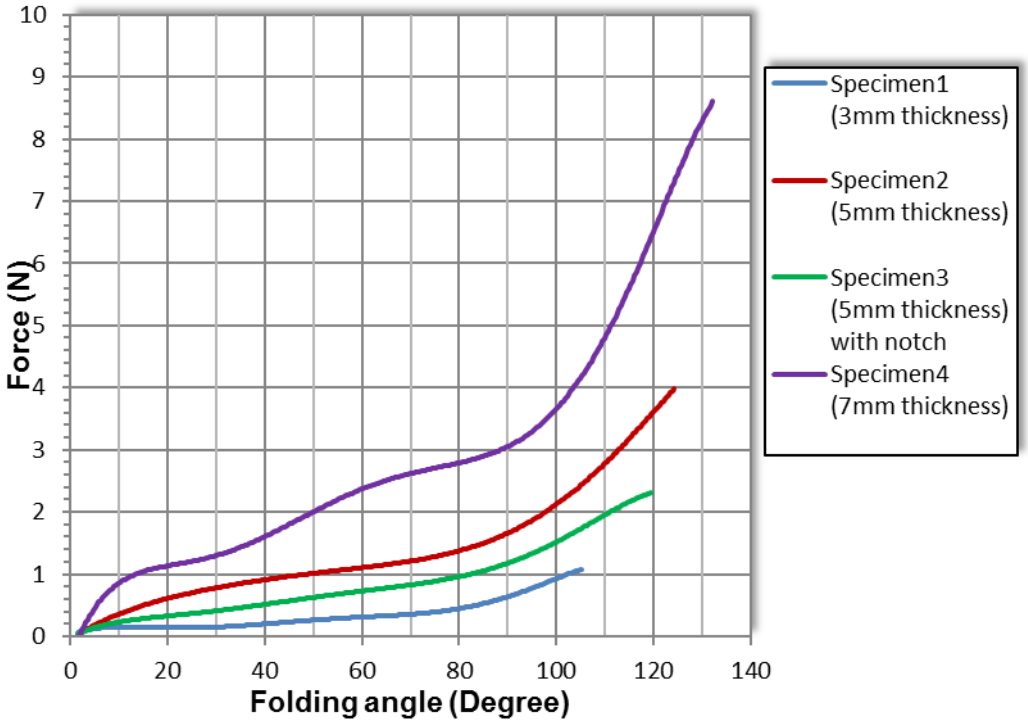

Figure 4.14 The folding angles -forces curves for different thickness specimens made from Tango Plus flx930.

The relationship between the thickness and the force is drawn as shown in Figure 4.15. This figure was plotted by taking the amount of force required to bend the three thickness (3mm, 5mm and 7mm) with the same folding angle. After that, second order of polynomial equation is calculated from these three points. These equations describe the relationship between thickness and force. These equations can calculate the force for any thickness at a certain folding angle. Table 4.3 provides the results of the force for different angles of folding with the thickness (t= 1mm).

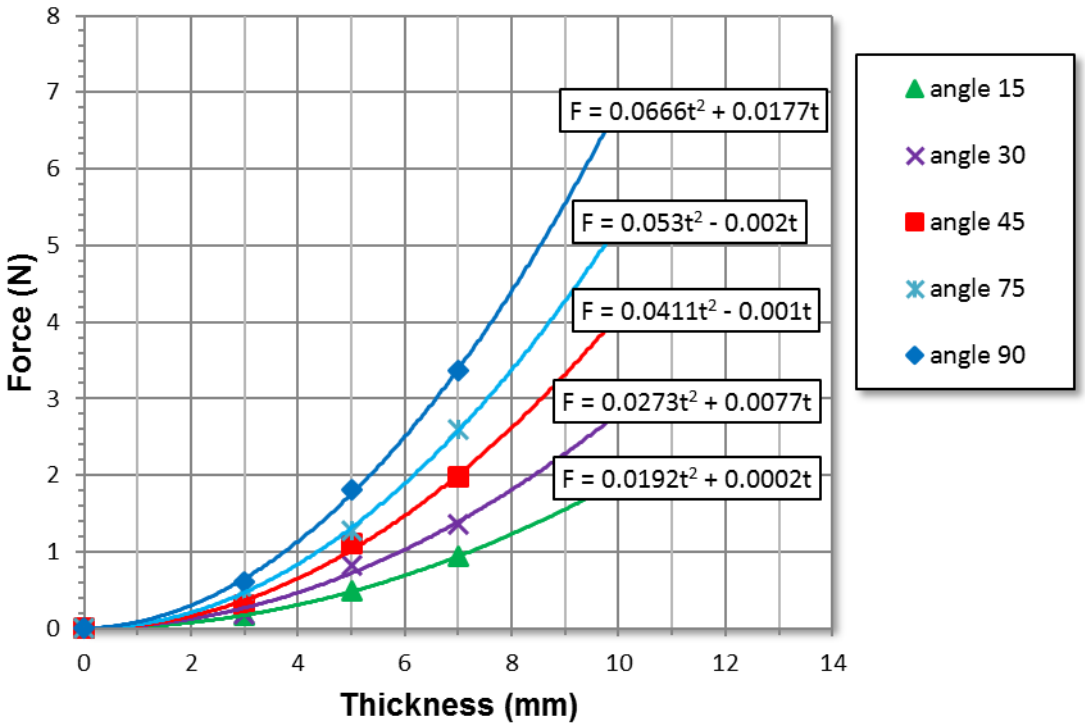

Figure 4.15 The relationship between the thickness and the force for different angles of folding.

Table 4.3 the force for different angles of folding with the thickness (t= 1mm).

Angle of Folding θ_i (Degree)	15	30	45	75	90
F(N)	0.0194	0.035	0.0401	0.051	0.0843

The equation that described the relationship between the force and folding angle at t=1mm is calculated from the data of Table 4.3. In this case, the linear equation was chosen to describe this relationship which is:

$$F = 0.0494\,\theta_i \qquad \textbf{4-9}$$

Where θ_i is in radian units (t=1 mm).

This equation has a maximum error of 20% which is acceptable for this case.

As a result, all equations that describe the relationship between force and folding angle for many thicknesses of hinges can be calculated from the data resulting from this test. In this research, the hinge which is used in the folding structure has the thickness of 0.5-1.5 mm. As was seen before, all data required for folding these hinges can be calculated with these values of actual hinge thickness. It should be emphasised here that all the forces calculated are for hinge made from pure Tango Plus flx930 and the effect of faces on these hinges are neglected.

4.5.3 Fatigue test for Tango Plus

The fatigue life of a material is a key parameter when the material is used in an operation that has a dynamic load. In origami structures, the material in the hinge is subjected to repeated loads which are produced by the folding and unfolding process. Therefore, the fatigue limit for the Tango Plus FLX930 should be calculated by using a fatigue test. The fatigue test was preformed for three specimens with three different elongation magnitudes (30%, 60% and 100%) the exact dimensions of the specimen shape is seen in Figure 4.16. The specimens were designed according to the ASTM standard ASTM D4482-11, 2011. The final specimen shape that was printed on an object-1000 3D printer is seen in Figure 4.17.

The Instron Electro-Puls E10000 machine was used for this test. The fatigue test machine was calibrated before starting the test. The test was operated three times for three specimens with 100% elongation, three times for three specimens with 60% elongation, and once for the specimens with 30% elongation (i.e., the elongation is the maximum extension input to the machine). The loading and relaxation cycle was taken from the ASTM standard. This standard specified a testing frequency of 1.7 Hz. Figure 4.18 shows the fatigue test specimens after test.

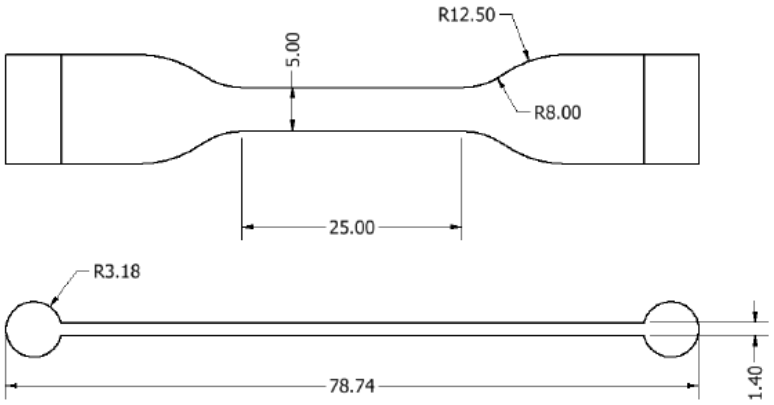

Figure 4.16 An engineering drawing of the fatigue test specimens. All measurements given in millimeters.

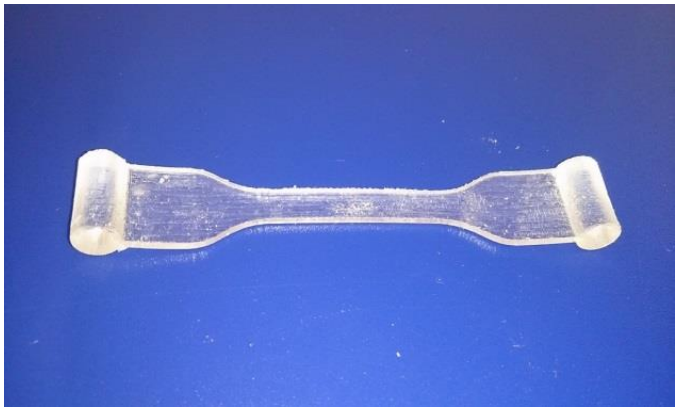

Figure 4.17 The fatigue test specimen made from Tango Plus.

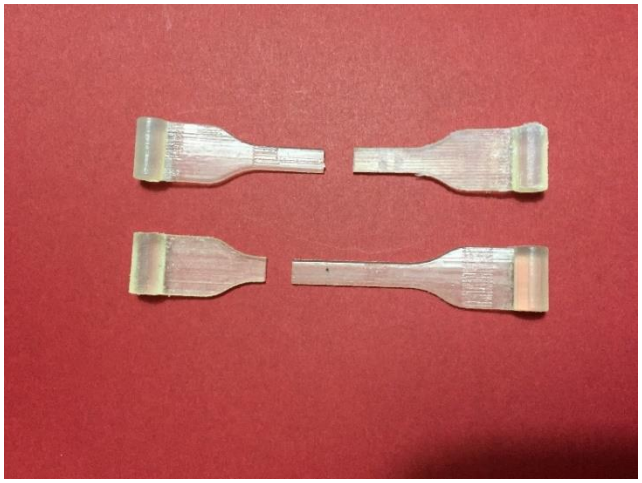

Figure 4.18 The fatigue test specimens made from Tango Plus after test.

The average results taken from fatigue machine are (6992 cycles, 3640 cycles and 1861 cycles) for the strains (0.32, 0.6, and 1) respectively. From these results, the equation of fatigue life can be obtained as:

$$N = \left(\frac{\varepsilon_a}{\varepsilon_o}\right)^k \qquad \textbf{4-10}$$

Where N is the fatigue life in a number of cycles, ε_a is the actual strain and ε_o & k are the constants of the equation. The constants are calculated as (ε_o=723 and k= -1.14). Therefore, the equation of fatigue life for the Tango Plus FLX930 will be:

$$N = \left(\frac{\varepsilon_a}{732}\right)^{-1.14} \qquad \textbf{4-11}$$

Furthermore, the ε-N curve can be obtained from the results which represent the strain vs. fatigue life for the Tango Plus FLX930. See Figure 4.19.

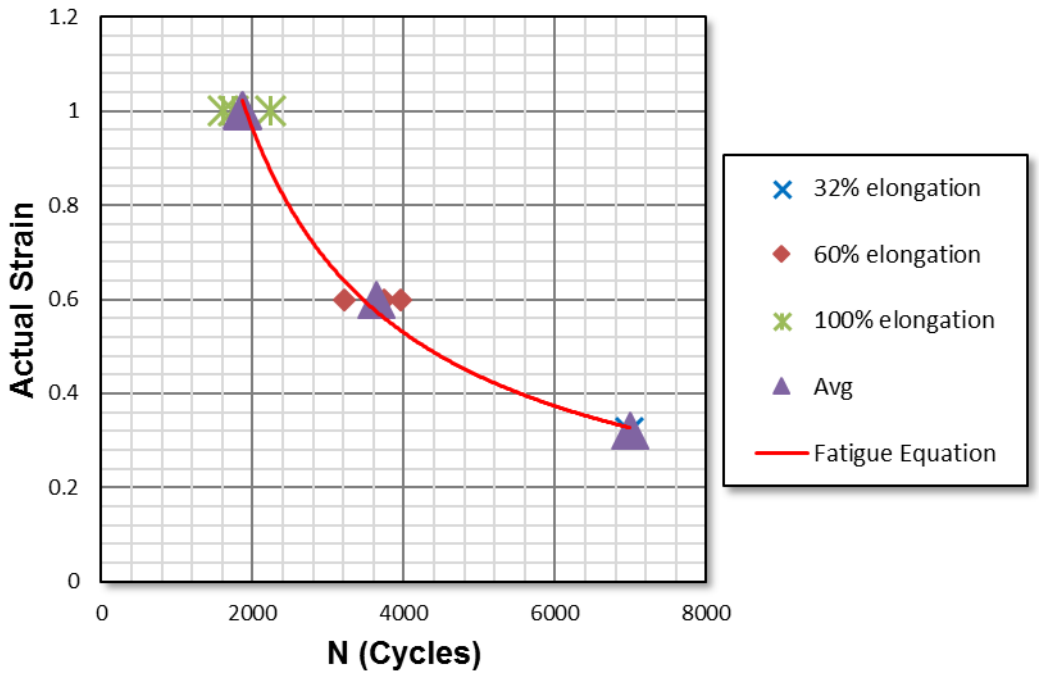

Figure 4.19 ε-N curve for the Tango Plus FLX930.

4.6 Kapton and Laser cutting approach

The use of laser cutting is another possible approach to the fabrication of a folding structure. It is also possible to use the same design technique as outlined for the 3D printing approach, which is to use two types of materials to form the folding structure. The first type of material should be solid to use as faces, while the second type of material should be soft or easily bent for use as hinges. For this project, acrylic with 1mm thickness was used as face material due to its solid nature and ease of use in laser cutting. Kapton film was used as the hinge. Kapton is not classified as a soft material but it is easily bent because it is a thin film.

In this approach, the acrylic is cut into the shape of faces of the crease pattern by using laser cutting machine. This acrylic sheet is the middle layer. This middle layer is covered from two sides using the Kapton material. The gap between two faces forms the hinge width which is covered by Kapton film from both sides.

As described in section 4.5, the hinge part (crease line) is subjected to the load directly when the structure folds. It should have a clear view of the mechanical properties of the material that represents the hinge part. Therefore, the mechanical properties of Kapton film are discussed in the next section.

4.6.1 Mechanical properties of Kapton

Kapton is a high-quality polyimide film which is produced by DuPont™ [77]. There are several types of Kapton polyimide films with the most commonly used types being the HN, FN, and MT. These are the characters that represent different types of Kapton. Each type of Kapton has an individual fabrication approach and chemical components. These types have some differences in properties such as electrical and thermal properties, and also have slightly different mechanical properties.

In this research, the Kapton film HN is used to representing the hinge in the folding structure that is fabricated by using laser cutting. This type of Kapton has a high balance of properties over a wide range of temperature. It is fabricated as a thin film and thin tape with the range of thickness between (25-125µm). DuPont™ company provides the datasheet of this type of Kapton with all properties and the methods used for testing. All mechanical properties are shown in Table 4.4.

Table 4.4 Physical Properties of DuPont™ Kapton® HN at 23°C (73°F)

Property	Unit	1 mil 25µm	2 mil 50µm	3 mil 75µm	5 mil 125µm	Test Method
Ultimate Tensile Strength at 23°C, (73°F) at 200°C (392°F)	psi (MPa)	33,500(231) 20,000(139)	33,500(231) 20,000(139)	33,500(231) 20,000(139)	33,500(231) 20,000(139)	ASTM D-882-91
Ultimate Elongation at 23°C, (73°F) at 200°C (392°F)	%	72 83	82 83	82 83	82 83	ASTM D-882-91
Tensile Modulus at 23°C, (73°F) at 200°C (392°F)	psi (GPa)	370,000 (2.5) 290,000 (2.0)	370,000 (2.5) 290,000 (2.0)	370,000 (2.5) 290,000 (2.0)	370,000 (2.5) 290,000 (2.0)	ASTM D-882-91
Density	g/cc	1.42	1.42	1.42	1.42	ASTM D-1505-90
MIT Folding Endurance	cycles	285,000	55,000	6,000	5,000	ASTM D-2176-89
Tear Strength-propagating (Elmendorf), N (lbf)		0.07 (0.02)	0.21 (0.02)	0.38 (0.02)	0.58 (0.02)	ASTM D-1922-89
Tear Strength, Initial (Graves), N (lbf)		7.2 (1.6)	16.3 (1.6)	26.3 (1.6)	46.9 (1.6)	ASTM D-1004-90
Yield Point at 3% at 23°C, (73°F) at 200°C (392°F)	MPa (psi)	69 (10,000) 41 (6,000)	69 (10,000) 41 (6,000)	69 (10,000) 41 (6,000)	69 (10,000) 41 (6,000)	ASTM D-882-91
Poisson's Ratio		0.34	0.34	0.34	0.34	Avg. three samples, elongated at 5, 7, 10%

From Table 4.4 it is seen that the yield point at 23º C is 69 MPa which is significantly higher than the Tango Plus tensile strength. However, it has a smaller elongation than the Tango Plus elongation. This mean that the Kapton is not a soft material compared with the Tango Plus material, but it can be bent easily because it is a very thin tape with high tensile strength.

In Kapton tape, the force required to bend it, can be neglected because it is a very slight amount. The force that has a great effect on the folding structure is the weight of faces and the resistance of Kapton material to the pulling force. The fatigue limit is not illustrated inTable 4.4. Therefore, a fatigue test is performed for Kapton tape which is illustrated in the next section.

4.6.2 Kapton Fatigue Test

The fatigue limit is a significant parameter that is not listed in the material datasheet of Kapton. Although, the Kapton tape has a high flexibility and bends with a small amount of strain in hinge tip, the fatigue limit should considered to have clear results of the amount of strain that could be hold by a Kapton hinge during dynamic fluctuating loading.

The Kapton fatigue specimen has the same dimensions of the tango plus specimen that was illustrated in section 4.5.3. However, it was not possible to make the specimen from pure Kapton tape because it is a very thin tape. The specimens were made from the acrylic material with double sides of Kapton tape in the effective area. The length of the Kapton tape in the fatigue specimen is 10mm. All results from this test are for the double sides of Kapton tape. See Figure 4.20 which shows the actual shape of double sided Kapton fatigue specimen.

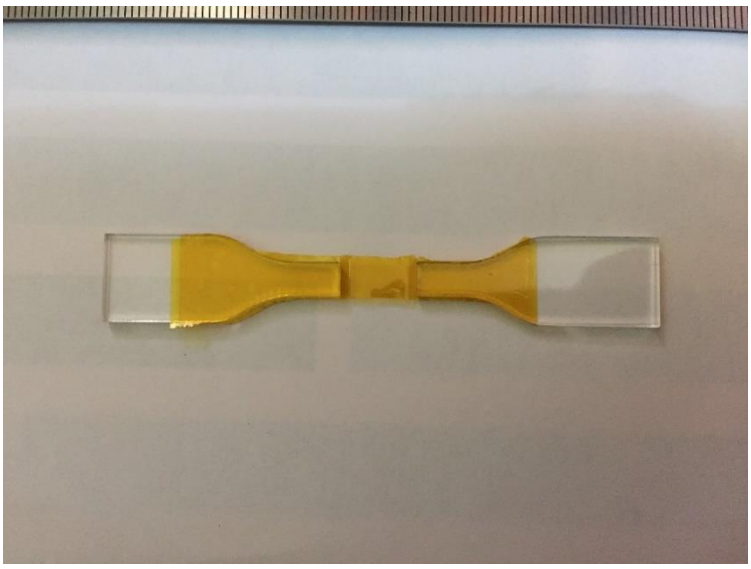

Figure 4.20 The actual shape of double sides Kapton fatigue specimen.

The Instron Electro-Puls E10000 machine was used for this test. The fatigue test machine was calibrated before starting the test. The test was operated three times for each elongation which are 2mm, 1.5mm, and 1mm. The loading and relaxation cycle was taken from the ASTM standard. This standard specified a testing frequency of 1.7 Hz.

The average results taken from the fatigue machine are (19 cycles, 14437 cycles and 20000 cycles without failing) for the strains (0.2, 0.15, and 0.1) respectively. The ε-N curve can be obtained from these results which represent the strain vs. fatigue life for the double Kapton sides. See Figure 4.21. This figure shows that the strain fatigue limit for double Kapton tape sides is 0.1. This means that, Kapton can be used for dynamic loads that cause strain under 0.1, without fatigue failure.

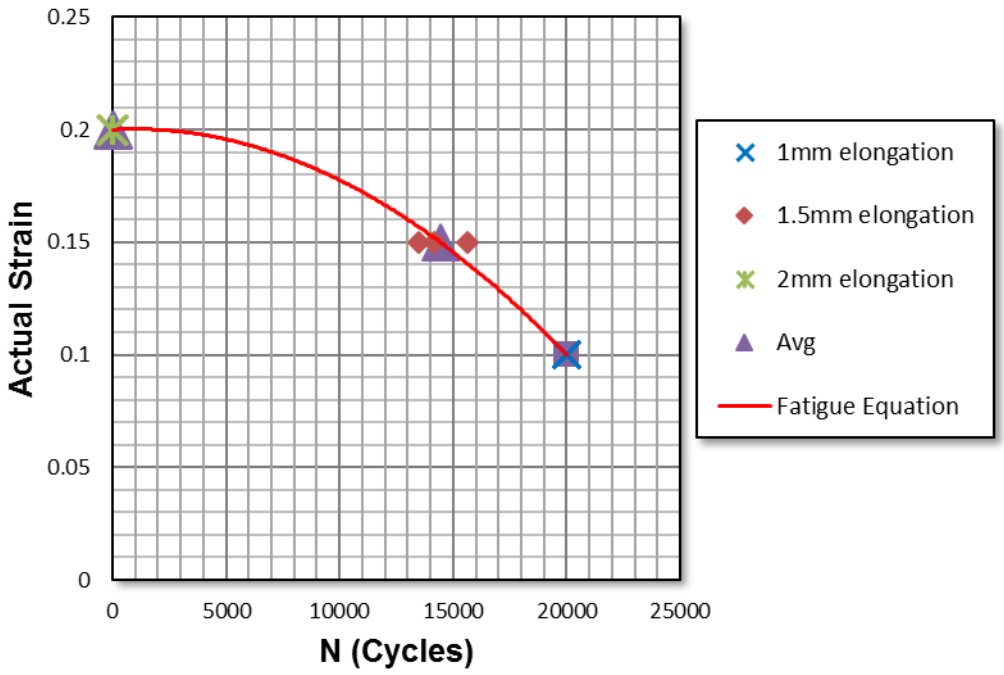

Figure 4.21 ε-N curve for the double Kapton sides.

4.7 Conclusions

In this chapter, the maximum strain at the crease tip is calculated from the width and thickness of the hinge. This value should take into account when designing any folding structure. For a successful design, the strain should not be up to the maximum strain limit.

The model of the folding structure pattern can be printed on the 3D printer using the Vero material for surfaces and Tango Plus FLX930 for the hinges. The strain and stress are determined in these hinges by assuming them as a beam and using equations derived from mechanical principles. However, the mechanical properties of the material at that hinge must be calculated.

Therefore, three tests on Tango plus FLX930 are performed. From these tests, the fatigue life limit, tensile strength and the amount of force required to fold Tango Plus material with different thickness were obtained. The results show that the strain limit of fatigue is 0.226 for high dynamic load, but it can be increased to 1.6 for low cyclic load. Furthermore, the Tango plus FLX930 cannot fail due to tensile forces under this range of strain. The Kapton mechanical properties shows high tensile elongation compared with the Tango Plus material. The Kapton fatigue limit is calculated and the results show that the strain limit of fatigue is 0.1 for high dynamic load.

The bending test gives the results for the force required to fold the beam made from the Tango plus FLX930 material. The extrapolation method was used to calculate the force for any thickness and angles. The actuator must provide these amounts of force. Therefore, in the next chapter, the force generated by some actuators that are used for self-folding processes and manipulation are investigated.

Chapter 5 ACTUATION

5.1 Introduction

This chapter explores the ability of actuators to be used in an actuation system for origami structures. Origami structures were investigated in chapter three to find out the types of origami structures that have suitable behaviour and performance to use as a self-folding or origami manipulation robot. The Origami Structure for Manipulation (OSM) was described in section 3.8 as a new type of origami robot arm. This structure can be fabricated using different types of materials. According to chapter four, there are two ways to fabricate origami structures, and both of them depend on using soft and hard materials combined together. The first way is to use multi-materials in a 3D printer, to print folding structures using the soft material Tango Plus flx930 as a hinge and the hard material Vero as faces. The second way is to use Kapton tape as a hinge and Acrylic as faces. In the present chapter, two main approaches of actuation are suggested to provide the actuators for these origami structures. These approaches are external actuation and embedded actuation.

The external actuation uses actuators outside the controlled structure that transmit the force using a force transmission system, for example, strings, ropes, and chains. This actuation system can use any actuator types that provide a different amount of force and motion speed. Most of them are conventional actuators like motors.

The embedded actuation uses actuators embedded in the structure and is a part of it. This actuation system requires special types of actuators that can generate force on the elements. Actuators created with smart materials are a popular

actuator with the potential to be used in an embedded actuation system. The requirements to design an embedded actuation system are, the selection of a suitable smart material that could be embedded in the structure which provides the required force, and choosing the activation type.

In this chapter, first external actuation is described and two types of force transmission systems are analysed, force transmission using string, and force transmission using 3D printed materials. After that, the embedded actuation is described. Smart materials are investigated and the shape memory wire actuators are examined and tested. In the final part of the chapter, discussion and conclusions are drawn.

5.2 External Actuation

The origami structure for manipulation (OSM), which was described in section 3.8, is a folding arm with four sides of origami structure. Every side can be manipulated using a string connected to an external actuator. In this case, the OSM required four actuators to manipulate it to give four degrees of freedom.

Many types of actuators could be used in an external actuation system e.g. electrical motors, pneumatic actuators, magnetic fields, and other conventional actuators. This variation of actuator types that could be used with this system of actuation is because the actuators located outside the structure. The significant point to choose the actuator is the required force to manipulate the structure. In this research, electrical motors are chosen to manipulate the folding structure OSM because they provide a suitable amount of force, they are easy to control, and they have a relatively high response speed.

The stepper motor and servo motor are two types of electrical motors that are suitable for use in an external actuation system for the OSM structure. The actuator requirements to manipulate the OSM structure are relatively high-speed, high torque, and precise angular movement when using a pulley or gears as a transmission system. Furthermore, a constant holding torque (without the need for the motor to be powered) is not required. Therefore, servo motors are chosen for the external actuation system of the OSM structure.

The motor type (MG996R) with a metal gear servo is used for actuation of the OSM structure. This high-torque servo can rotate approximately 120 degrees. For its Specifications see Table 5.1.

Table 5.1 Specifications of servo motor (MG996R)

Weight	55 g
Dimension	40.7 x 19.7 x 42.9 mm
Stall torque	92.2 N.cm (4.8 V), 107.8 N.cm (6 V)
Operating speed	0.17 s/60º (4.8 V), 0.14 s/60º (6 V)
Operating voltage	4.8 V - 7.2 V
Running Current	500 mA - 900 mA (6V)
Stall Current	2.5 A (6V)

The second part of the external actuation system is the transmission system that could transmit the required force for the structure. A string is chosen to be the transmission tool for this system.

5.2.1 Force transmission using string

String was used when the structure required an axial pulling force to manipulate it. Four axial pulling forces are required to control the OSM structure with four DOF. The structure uses four ropes (one rope in every side) to manipulate it. The properties of the rope, that should be considered when it used in an actuation system, are the stretch, weight and stiffness. Furthermore, the important property is how much load can be held before breaking, this is called the breaking load and it can be calculated using a tensile test.

The Dyneema rope is used with our actuation system. Dyneema is an UHMwPE (Ultra High Molecular weight Polyethylene) fibre which is an ingredient material in many of highest performance ropes and is used across a range from kite lines to heavy lift slings. Samples of 1mm diameter SK75 Dyneema rope were tested in order to calculate the breaking load. The Specifications of this rope, which are taken from the supplier (www.ropelocker.co.uk), are a low stretch and high strength. Furthermore, it has (1912 N) break load for 1mm diameter and its weight is 0.09 g/m.

Five specimens of 1mm diameter of Sk75 Dyneema with three different lengths (100 mm, 200mm, and 300 mm) were tested on tensile test machine to calculate the breaking load. The specimen was attached to the testing rig using the double figure-eight loop knot which is a strong knot used in many sports activates like

climbing and sailing. The Instron 3369 tensile machine was used for this test. The tensile test machine was calibrated before starting the test and the test velocity was set at 20 mm/min. This movement caused an increase in the pulling load until the specimen breaks. See Figure 5.1 and Figure 5.2.

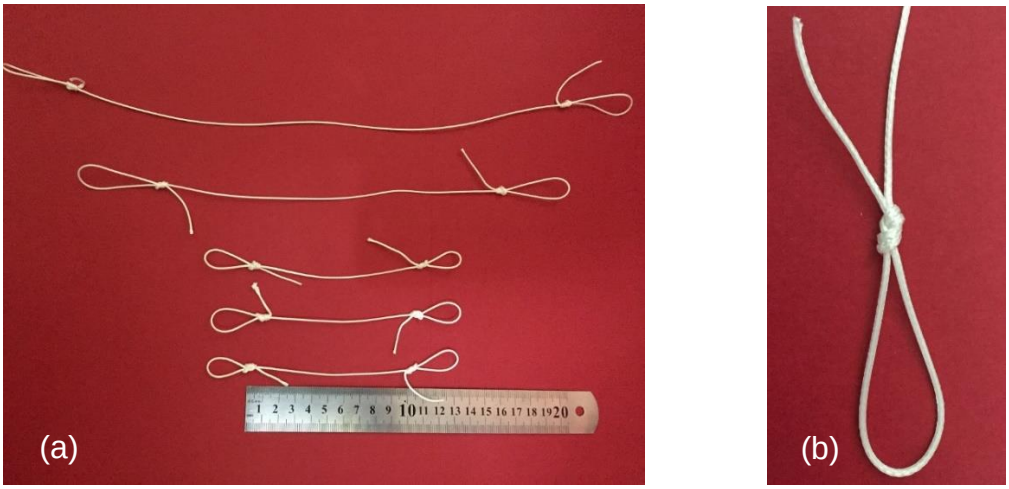

Figure 5.1 (a) The 1mm SK75 Dyneema Rope specimens. (b) The double figure-eight loop knot.

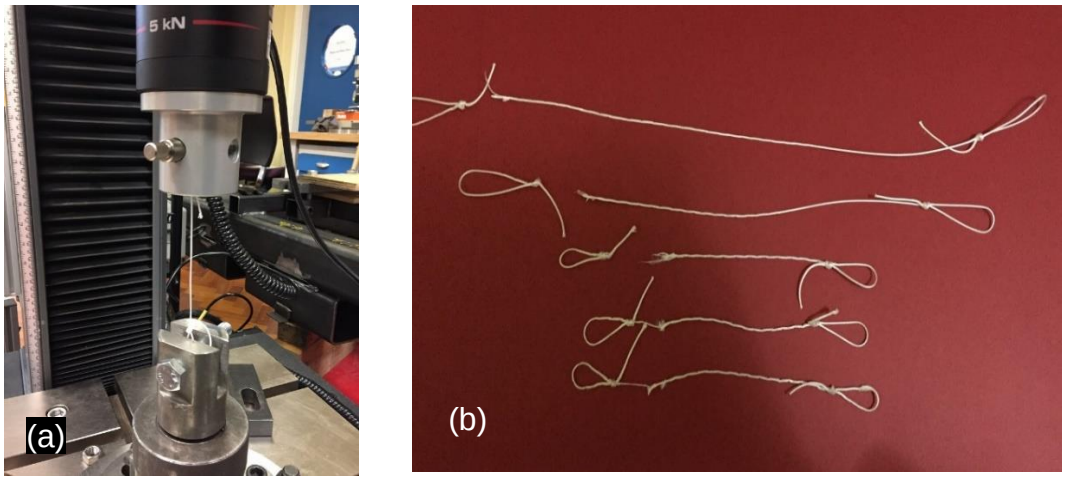

Figure 5.2 (a) Tensile testing machine. (b) The specimens after testing.

The results of the load and extension for the five specimens are then plotted as shown in Figure 5.3. Furthermore, the stress, strain and Young's Modulus can be calculated using the stress, strain equations (4.7) & (4.8), and Young's Modulus equation:

$$E = \frac{\sigma}{\varepsilon} \qquad \textbf{5-1}$$

Then the results of the stress and strain for the five specimens are plotted as shown in Figure 5.4.

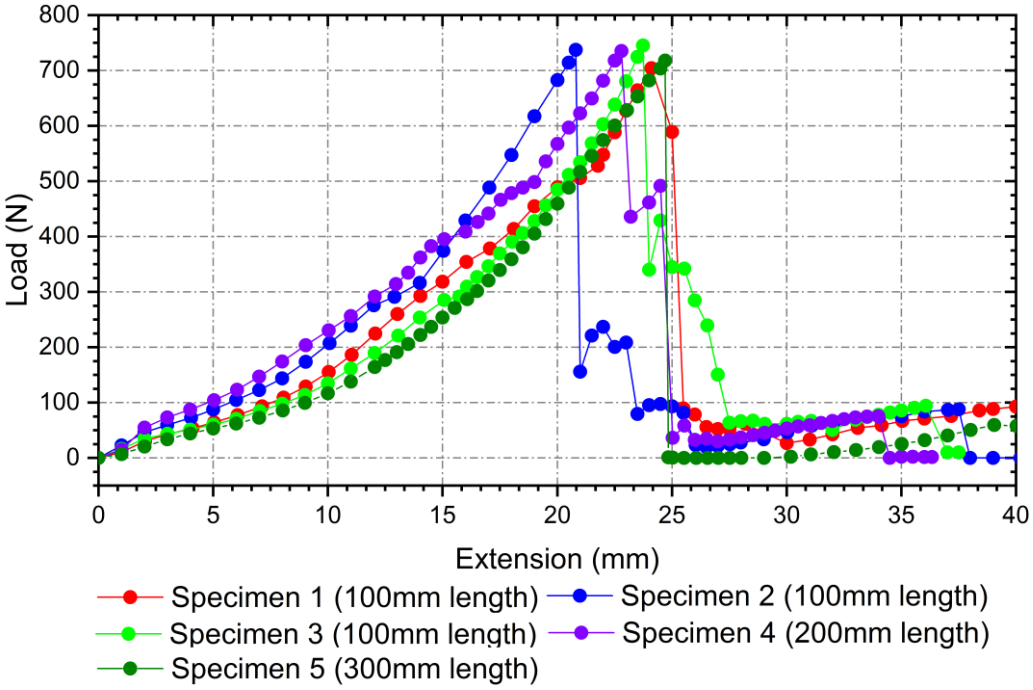

Figure 5.3 Results of the tensile testing of 1mm SK75 Dyneema Rope.

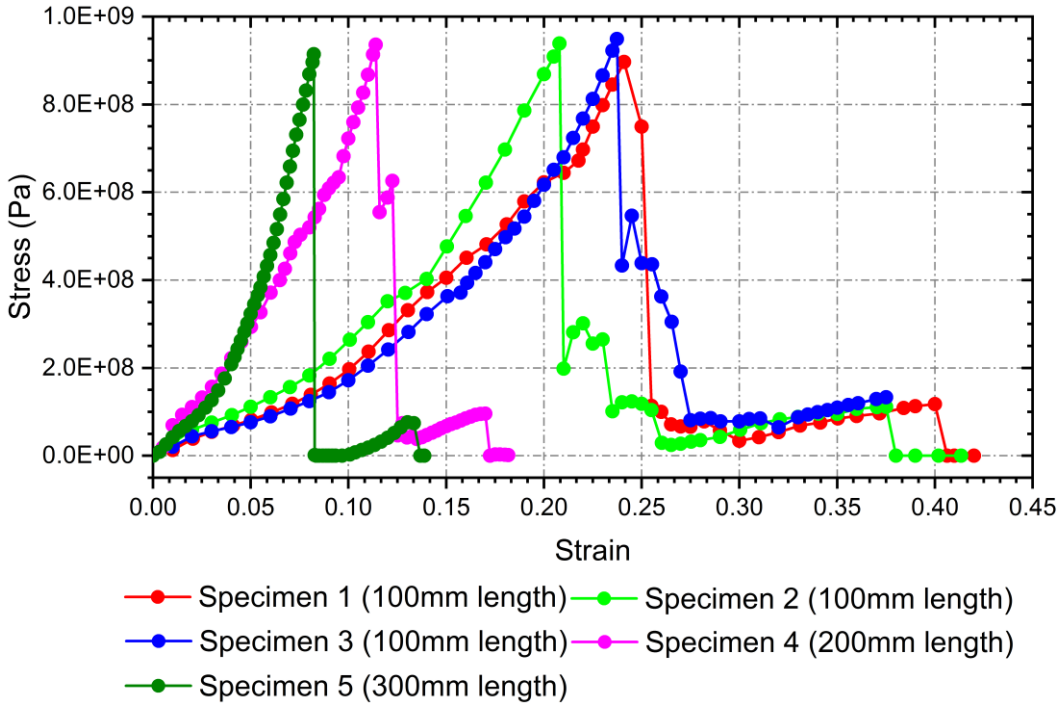

Figure 5.4 Stress – Strain curve for 1mm SK75 Dyneema Rope.

The average breaking load for the SK75 Dyneema rope in Figure 5.3 is 728N, and the average strain at the breaking load in Figure 5.4 is 0.176. Comparing the breaking load to the value taken from the supplier, a decrease of 61% was noted. This result is expected because other researchers found a decrease in breaking load when they tested different diameters of Dyneema rope [78].

Although the breaking load is reduced to 39% from the breaking load given, it is still very big compared to the amount of force that is required to manipulate the OSM structure. When the structure is made from card paper, it weighs a few grams and requires just 0.5-1N to manipulate it. Furthermore, it could weigh 150-200g or 250-350g when it is fabricated using laser cutting or a 3D printer. When these values of weights are adding to the forces required to fold the hinges, the overall force that is required to manipulate the structure can be calculated, and it is approximately 2.5-3.5N for the Acrylic-Kapton OSM structure, and 20-23N for the 3D printed OSM structure (All the details of calculating the weights and overall forces are illustrated in chapter six).

The SK75 Dyneema rope is strong, low stretch and has an excellent performance to be a force transmission tool. These properties make it a suitable choice to use in an external actuation system. For the OSM structure, the SK75 Dyneema rope provides force transmission ability more than the structure needs. Therefore, another force transmission tool was fabricated using a 3D printer.

5.2.2 Force transmission using 3D printed chain

Building the OSM structure using a 3D printer provides an opportunity to print the transmission system in the same process. This process produces a “print to go” structure that could attach the actuators immediately. This fabrication approach reduces the assembly process that was required when using other string types.

The design of the 3D printed transmission system or string depends on the material type and the shape of the string. Three types of 3D printed string were made. The first one is a cylindrical rod made from Tango Plus material, the second one is a square section bar made from combining two materials which are the Tango Plus material and the Vero material, the third one is a cylindrical chain made from Vero material. See Figure 5.5.

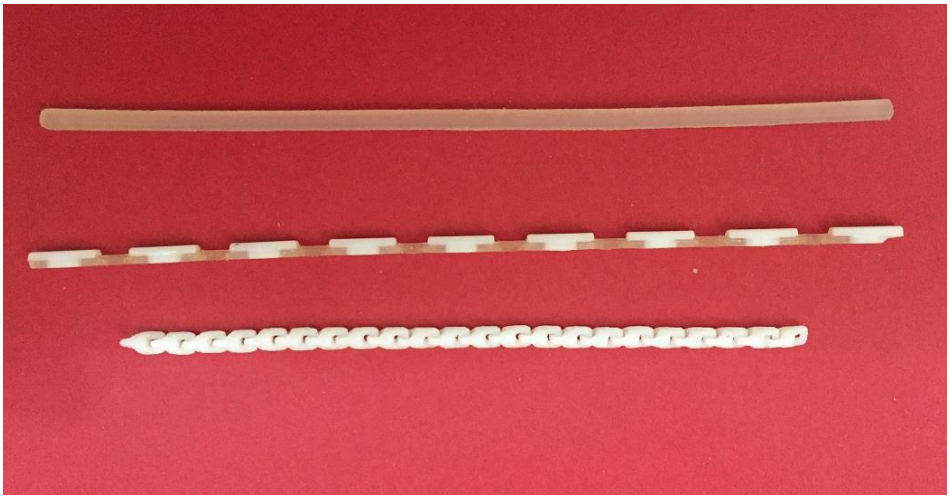

Figure 5.5 Three types of 3D printed strings. From up to down, cylindrical rod (Tango Plus material), Tango Plus with Vero segments, and Vero chain.

The first type is made from Tango Plus flx930 material. This material was tested in chapter four and its properties are known. From a tensile test, it seems that the extension of the material is 250- 260% and the yield stress is 0.68 MPa. The breaking load can be calculated by using the stress equation and knowing the cross-section diameter of the rod and the yield stress. The result of the breaking load is (4.45N) and this is a very small load compared with the required load to manipulate the OSM structure which is approximately (20-23N). Furthermore, the high extension value of this material makes it stretch under the load effect and transmit a small amount of force.

The second type shows the same behaviour as the first type when it is tested because the intervals of the Tango Plus material control the bar behaviour. The solid parts that are made from Vero material reduce the extension value of the bar but they do not increase the breaking load. Using the stress equation to calculate the breaking load of the Tango Plus interval, it seems to be (3N). This breaking load is smaller than the breaking load of the first type.

The third type is the chain which is designed to be a cylindrical chain and consists of several links that are connected together. The essential link part is a small rod with 1mm diameter, that is connected with the other rod of another link to form the chain. This design gives high flexibility with very low extension ability. This chain was printed using Vero material. Figure 5.6 shows the shape and dimensions of the chain link, showing the chain printed using Vero material.

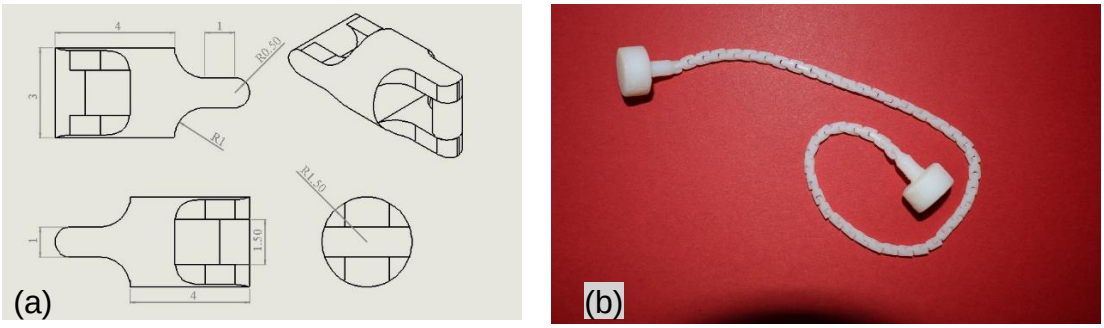

Figure 5.6 The design of 3 mm diameter 3D printed chain. (a) Design and dimensions of one element from the chain. (b) final shape after print.

Since the 1mm rod that connected every two links in the chain is the weakest part, the breaking load of this rod is assumed to be the breaking load of the chain. The breaking load is calculated analytically using the maximum shearing stress theory (Tresca yield criterion) which predicts that "yielding begins when the maximum shearing stress equals the maximum shearing stress at the yield point in a simple tension test" [74]. The maximum shearing stress is assumed to be equal to the yield stress for the Vero material which is known from its datasheet. Then the load can be calculated by using:

$$\tau_{max} = \frac{F}{A} \qquad \textbf{5-2}$$

Where

τ_{max} = the maximum shearing stress.

A = the cross sectional area.

F = the load.

By using the yield stress of the Vero material, which equals (50 MPa), the breaking load value is calculated as (39.27 N). This analytical value of breaking load is more than the force that is required to manipulate the 3D printed OSM structure. However, the breaking load was calculated using other methods so as to ensure that the 3D printed chain could be used as a force transmission tool.

The second method that is used to evaluate the breaking load is finite element analysis (FEA). SolidWorks software was used to perform the FE analysis with a model of chain link under applied axial load. Figure 5.7 shows the stress distribution results under applied axial loads of 19N and 23N. It seems that the maximum von Mises stress exceeds the yield stress of the Vero material when the load is equal to 23N. A decrease of 41% was noted when comparing this

breaking load to the analytical value. Moreover, this breaking load is nearly equal to the force required to manipulate the OSM structure and that means that the chain could fail during operation.

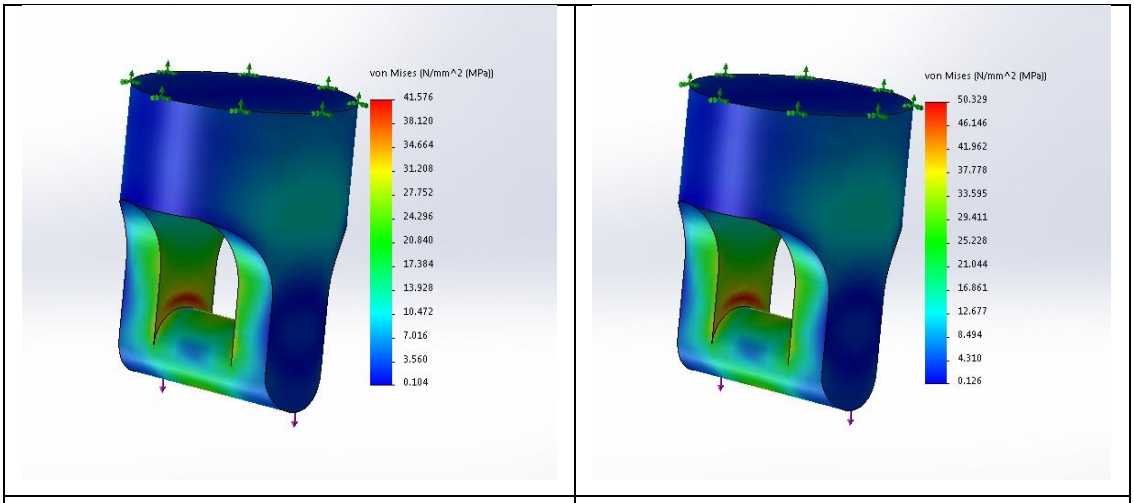

(a) (b)

Figure 5.7 The finite element stress distribution results under applied axial loads for the 3D printed chain link (a) applied axial load 19N (b) applied axial load 23N.

The third way to determine the breaking load is the empirical method. Six specimens with different lengths (100 mm, 120mm, 150mm and 200 mm, shown in Figure 5.8) were tested on tensile test machinery. The Instron 3369 tensile machine was used for this test. The tensile test machine was calibrated before starting the test and the test velocity was set at 4 mm/min. This movement caused an increase in the pulling load until the specimen broke, See Figure 5.9. The results of the load and extension for the six specimens were plotted as shown in Figure 5.10.

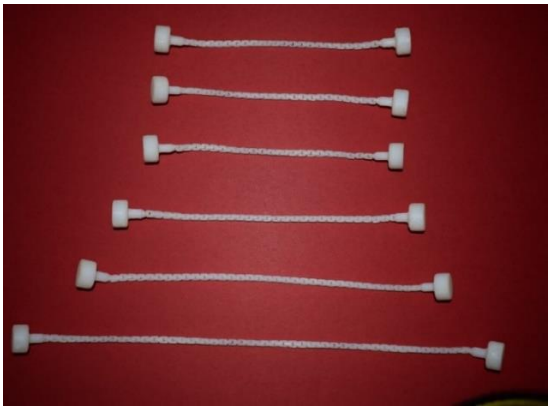

Figure 5.8 Six specimens of 3D printed chain.

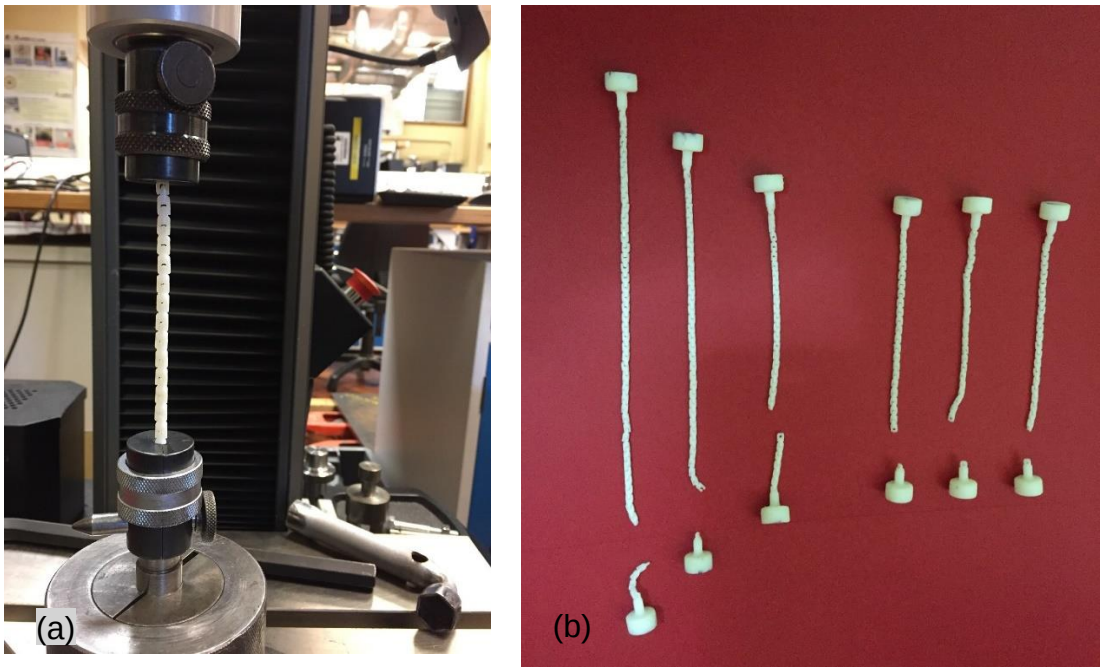

Figure 5.9 (a) Tensile testing machine. (b) The 3D printed chains after testing.

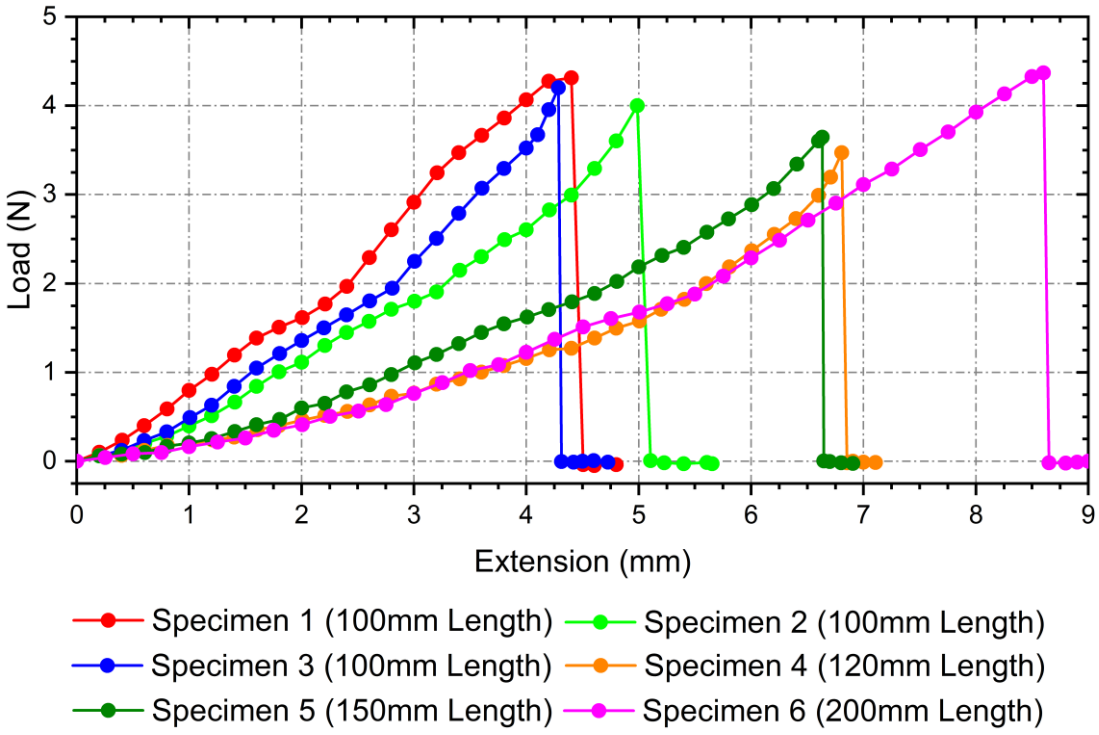

Figure 5.10 Results of tensile testing for the 3D printed chains.

The result of the average breaking load is 4.05N, and the result of average extension at the breaking load for the 100mm length specimens is 4.3mm. This breaking load is small compared with the load required to manipulate the 3D printed OSM structure. The empirical results prove that the 3D printed chain cannot be used as a force transmission tool. Furthermore, these results show that the “print to go” structure cannot be performed because the chain will fail during operation.

To increase the breaking load, two other specimens were printed with the diameter of 4.5mm and 100mm length, see Figure 5.11. The two specimens were tested on tensile test machinery using the same test procedure as the previous specimens. The results are shown in Figure 5.12. The average breaking load is 8.3N which is increased compared with the breaking load of the 3mm diameter chain but it is still below the load required to manipulate the 3D printed OSM structure.

The 3D printed chain gives a high flexibility performance to use as a force transmission tool for 3D printed structure but the breaking load is the issue. Furthermore, there is a big difference between the breaking load calculated analytically and the empirical one. The reason is that the material behaviour depends on the printing process. Therefore, every 3D printed structure showed be tested before using it.

Figure 5.11 The 4.5 mm diameter 3D printed chains compared with the 3 mm diameter 3D printed chain.

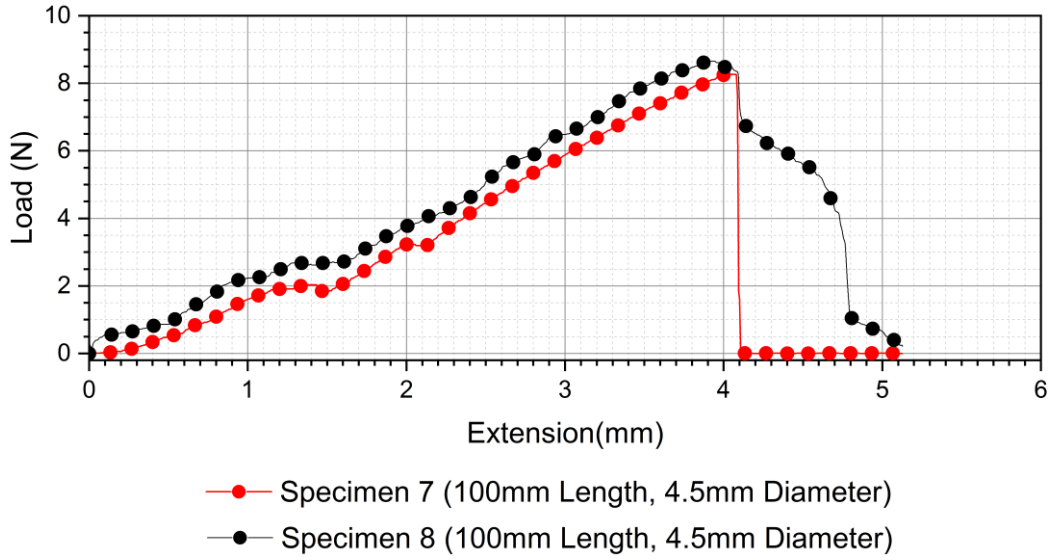

Figure 5.12 Tensile testing of the 4.5 mm diameter 3D printed chain.

5.3 Embedded Actuation

Embedded actuation means using actuators that could be embedded in the structure and be a part of it. This approach is useful when required to build an actuation system for a miniature robot or a self-folding structure. Although the external actuation provides a big amount of force, it cannot be used for the self-folding process because actuation of the self-folding process is more complicated compared with the manipulation structure. Many hinges should be folded to certain angles in sequence or at the same time during the folding process in the self-folding structures to form this structure. This would require many external actuators with a large force transmission system to operate the process. Therefore, the simple approach to actuation of the self-folding structure is to use embedded actuation. An actuator is attached to every folding hinge and there is no need for any force transmission.

Embedded actuation requires special types of actuators that can provide force directly. Smart materials as actuators are the popular choice for embedded actuation systems. The requirements to design the embedded actuation system are, choosing a suitable smart material that could be embedded in the structure and providing the required force, as well as choosing the activation type.

5.3.1 Smart materials

Smart Materials are the materials that have a property change as a response to changes in their environment. These materials have one or more properties that can be significantly changed in a controlled fashion by external stimuli, such as stress, temperature, moisture, pH, electric or magnetic fields, light, or chemical compounds. Some of these materials are used as sensors and others are used as actuators. The smart materials change their mechanical properties when activated, and usually they are used as actuators. The popular smart material that is used as an actuator in the miniature or self-folding robot are shape memory alloys (SMA) and shape memory polymers (SMP).

Shape memory alloys are the type of metallic alloys which have the capability to retain a particular size or shape prior to deformation, this is done by using the heating process. The shape memory effect comes from the phase transformation process between two crystal structures, the lower temperature martensite phase, and the higher temperature austenite phase. At the martensite phase, the SMA can be easily deformed by applying a small force. While in austenite, which is the high-temperature phase, the SMA becomes hard and has a higher Young's modulus. When the SMA is deformed in the martensite phase, it can recover its original shape when it is heated to a particular temperature. This heating process causes SMA to transform into the austenite structure. This process can be achieved by resistively heating the material using electric current, which is known as Joule's heating.

There are many types of SMAs that have been discovered. However, the type that has proven to be the most successful in engineering applications is the NiTi shape memory alloy, also known as Nitinol. The NiTi alloys have the greatest potential as actuator because they have many qualities such as reliability over millions of cycles under appropriate training, biocompatibility, they can be electrically heated, which simplifies the mechanism. In addition, they have the general advantage of overall SMA actuators such as a silent and clean operation, high work output, the simplicity of design and ease of miniaturization.

SMA actuators can be used in different forms such as straight wires, cantilever strips, helical springs, torsion tube and torsion springs. For every type of configuration, there are formulations or equations that calculate the force or torque generated and the bending produced. It is very complicated to derive the formula analytically. Therefore, some researchers use the empirical method to calculate the force or the torque.

The shape memory polymers SMPs have almost the same physical properties of SMAs, which are related to the different transformation phases, yet they are polymers. There are many examples of SMPs actuators, but the popular one used in robotics is the prestretched polystyrene (PSPS). This type is shrunk when subjected to uniform heating. These shrink actions can be controlled in order to form many folding shapes by using the multilayers approach.

The difference between SMPs and SMAs is that the PSPS activated fold is permanent while the SMA fold is not permanent but can be reversed through external manipulation. The ability of SMA to fold in two directions without manually resetting the state after each use makes it very useful to enable the cyclic operation for locomotion. For these reasons, the SMA is chosen to be used as actuators for the self-folding structure.

5.3.2 Shape memory wire actuators

The simplest type of SMA actuators that could be used with self-folding structures is the SMA wire. SMA wires enhance the simplicity of the joint structure when it is used as actuators for self-folding origami. According to the specific shape programming, the SMA produces various shape changes that induce various forces or torque directions. SMA wire is the cheapest type of SMA and can be conveniently shape-programmed for use in various applications.

Two types of SMW actuators are illustrated in this section which are the bending shape memory wire (BSW) and the torsion shape memory wire (TSW) actuators, see Figure 5.13. The difference between these two actuators is that the generated force by BSW depends on the one edge bending operation while the generated force by TSW depends on the rod torsion operation.

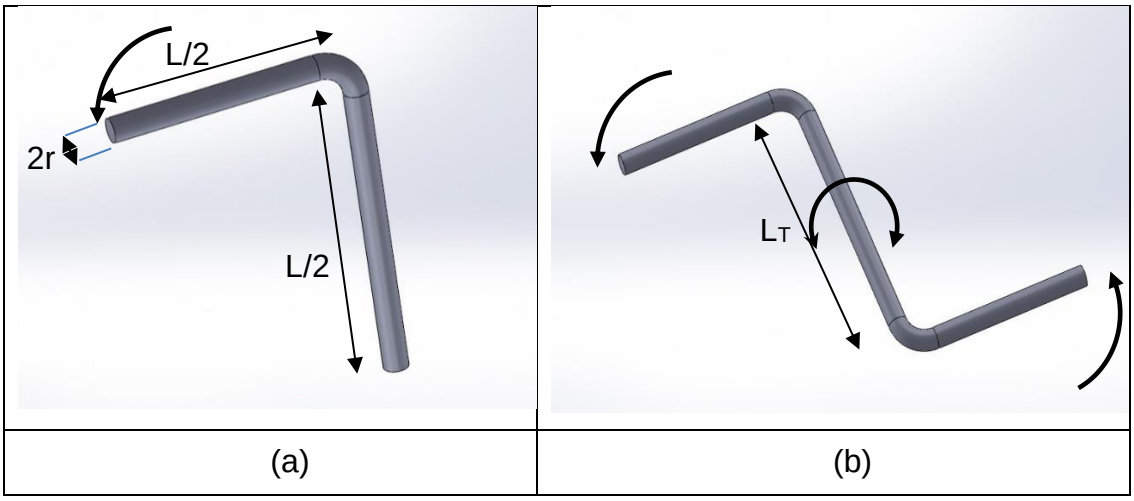

Figure 5.13 Design parameters of the BSW and TSW actuators (a) BSW actuator (b) TSW actuator.

To obtain a clear understanding of the BSW and TSW actuators, the model equations are derived by combining the mechanical constitutive model of the SMA and the deflection model of the wire (bending deflection or torsional deflection). The mechanical constitutive model was established by Liang et al. [79] on the basis of the Tanaka model [80] as follows:

$$\boldsymbol{\sigma - \sigma_0 = E(\varepsilon - \varepsilon_0) + \Theta(T - T_0) + \Omega(\xi - \xi_0)} \qquad \textbf{5-3}$$

where

ε is the strain; *T* is the temperature; ξ is the phase volume fraction, which is a function of ε and *T*; E is Young's modulus; Θ is the thermoelastic tensor; and Ω is the transformation tensor. The subscript "0" denotes the initial state. E, Θ, and Ω are functions of ε, *T*, and ξ. When the initial conditions are set to zero, the equation becomes [50]:

$$\boldsymbol{\sigma = E\varepsilon + \Theta T + \Omega\xi} \qquad \textbf{5-4}$$

By substituting this mechanical constitutive model in the equation for the bending beam:

$$\boldsymbol{M = \frac{\sigma I}{r}} \qquad \textbf{5-5}$$

We can obtain:

$$\boldsymbol{M = \frac{IE}{r}\varepsilon + \frac{I\Theta}{r}T + \frac{I\Omega}{r}\xi(\varepsilon, T)} \qquad \textbf{5-6}$$

The thermoelastic tensor, Θ, can be eliminated because there are just two thermal static models one for austenite phase at high temperature for actuation and one for martensite phase at low temperature for releasing. The phase of the SMA depending on the temperature affects the Young modulus, E. At high temperature, the Young modulus has a high value, E_a, which is an austenite phase. At a low temperature, it has a low value, E_m, which is in martensite phase. The model equation of BSW can be abbreviated to

$$\boldsymbol{M = \frac{IE}{r}\varepsilon + \frac{I\Omega}{r}\xi(\varepsilon)} \qquad \textbf{5-7}$$

The transformation tensor can be modelled as

$$\Omega = -\varepsilon_L E(T)$$

where ε_L is the maximum recovery strain [81]. Finally, the static model of the BSW actuator is given as

$$\boldsymbol{M = \frac{IE}{r}\varepsilon - \frac{IE}{r}\varepsilon_L\xi(\varepsilon)} \qquad \textbf{5-8}$$

To apply this model to the TSW, the model converted to shear mode is written as

$$\boldsymbol{\tau - \tau_0 = G(\gamma - \gamma_0) + \Theta_s(T - T_0) + \Omega_s(\xi - \xi_0)} \qquad \textbf{5-9}$$

Where

τ shear stress; γ shear strain; G shear modulus. The subscript “s” of Θ and Ω denotes the shear mode. By following the same above procedures and using the equation for the torsional beam:

$$\mathbf{T} = \boldsymbol{\frac{\tau J}{r}} \qquad \textbf{5-10}$$

The static model of the TSW can be calculated as

$$\mathbf{T} = \boldsymbol{\frac{JG}{r}\gamma - \frac{JG}{r}\gamma_L\xi(\gamma)} \qquad \textbf{5-11}$$

Both BSW and TSW have two design parameters which are the radius of the wire, r, and the length of the wire L for BSW, or the length of the torsional part, L_T, for TSW as shown in Figure 5.13. These two parameters have a relationship with the folding angle α and the strain, whether it is a normal strain ε or shear strain γ, as follows:

For the BSW:

$$\boldsymbol{\varepsilon = \frac{r}{L} \propto} \qquad \textbf{5-12}$$

For the TSW:

$$\boldsymbol{\gamma = \frac{r}{L_T} \alpha} \qquad \textbf{5-13}$$

The BSW and TSW actuators are fabricated using the heating process. The SMA wire is fixed in a zigzag shape along an array of bolts that are installed onto the aluminium plate. Then it is put into the furnace and heated at 400 °C for 15minutes. This process programs the shape of the wire into the zigzag shape. Then the array of the zigzag wire is cut to obtain multiple TSW and BSW actuators as shown in Figure 5.14. All the actuators are made from Nitinol (NiTi) SMA wire.

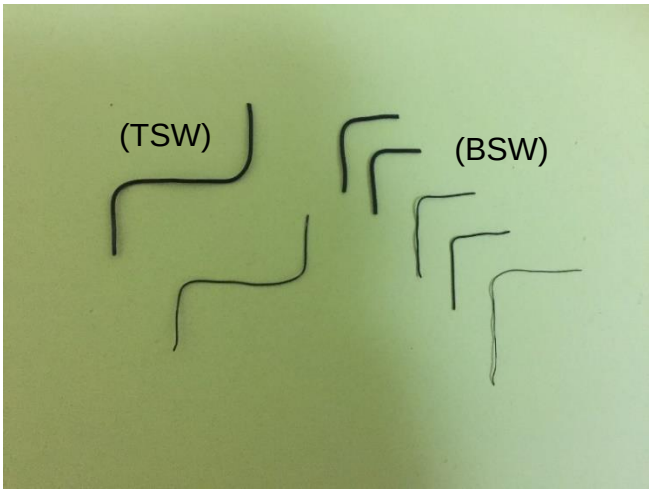

Figure 5.14 SMA wires in torsion (TSW) and bending (BSW) actuators types.

The BSW is programmed to fold 90^{o} folding angle and it could be fabricated with different folding angles. The TSW is programmed when it is fixed to the structure, for example, if 180^{o} folding angle is required, the TSW should be twisted -180^{o}. The negative sign refers to the opposite direction of the deformation.

By knowing the radius and the length for the BSW and the TSW, the normal strain and the shear strain can be calculated from the equations (5-12) and (5-13). However, the bending and torque calculations are complicated because they were required in order to calculate the maximum recovery strain experimentally. Therefore, a force test device for SMW actuators was built to test the force generated from BSW and TSW directly.

5.3.3 Force test device for SMW actuators

The significant parameters that are required to be determined for the SMW actuators are the generated force and the activation temperature. Therefore, the test device to measure these parameters should have a load cell, to measure the force, and thermosensor, to measure the temperature. The device was built using a flexible load cell and a thermocouple type K shown in Figure 5.15. The load cell that was used is called SingleTact load cell and it is from the supplier SingleTact [82]. It has a full-scale measure of 1N with force resolution <0.2% of full scale and it could measure up to 300% at full scale. The load cell is fixed to a 3D printed platform that has a pad placed above the load cell. This pad could be replaced with another one that has a different surface angle to measure the generated forces for different angles of folding, see Figure 5.16.

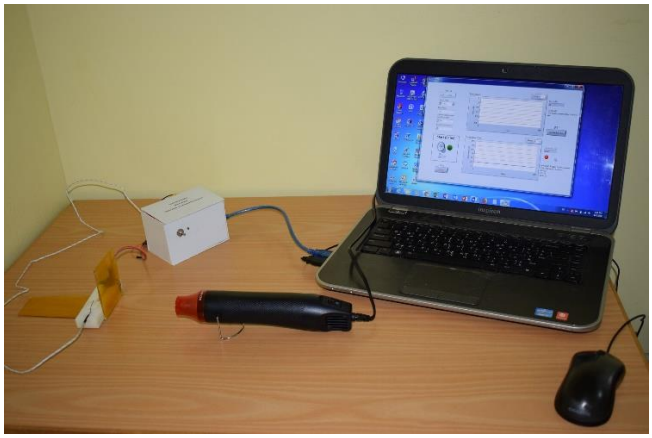

Figure 5.15 Force test device for SMW actuators

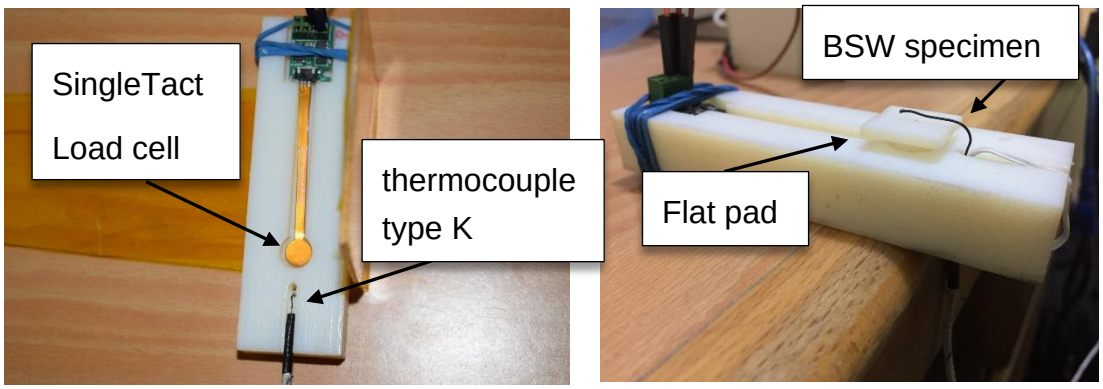

(a) (b)

Figure 5.16 (a)The load cell attached to 3D printed platform, and (b) the flat pad (90 folding angle) with fixed BSW actuator specimen.

The type K thermocouple that is used in this device has the temperature range from 0ºC to 700ºC with 0.25ºC resolution. It used the MAX6675 junction to convert the analog signal to digital. The two sensors are connected to the Arduino which is programmed to be compatible with the LabView software.

The virtual instrument script (VI) was built using LabView software to collect and save the results in an Excel file. Figure 5.17 shows the graphical user interface of the VI program which displays the temperature and force charts. Furthermore, it has a calibration button which resets the value of the load cell measure to the original line.

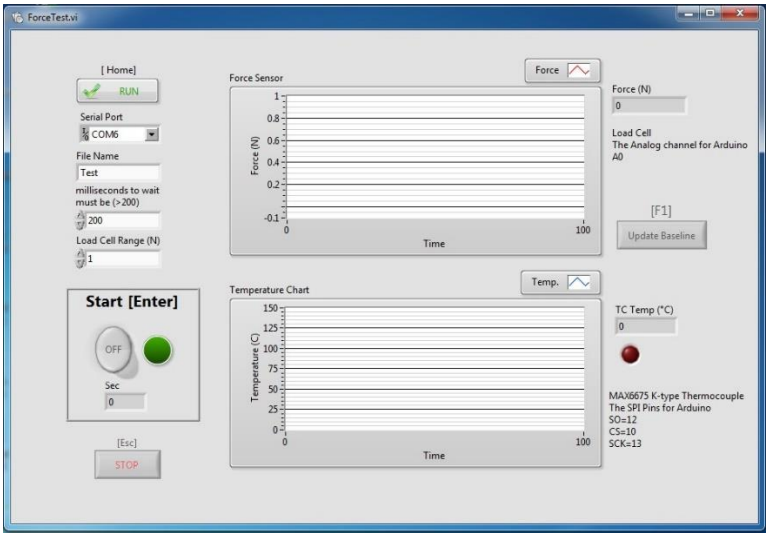

Figure 5.17 Graphical User interface for the force test device.

The test procedure starts with the selection of the pad angle that required to measure the force. The specimen is fixed in the 3D printed platform and the thermocouple attached it. The specimen is activated and the force measured at different temperatures. There are two ways to activate the SMW actuator. The first way is to use a hot air blower that can provide hot air at temperatures up to 200º C. The second way is to use a direct electric heating (Joule heating) process which activates the SMW with an electric current. A Mosfet transistor is used to prevent short circuit damage.

All sensors were checked before use. The thermocouple was checked using chilled water and boiling water. The thermocouple read 0.5º -0.7º C for chilled water and 100.4º -101º C for boiling water which means it has an error range between 0.7 to 1%. Furthermore, the hysteresis of the load cell was tested by using three loads (0.5, 0.7 and 0.9N) and the results are shown in Figure 5.18. The maximum value of the hysteresis error reached 5%.

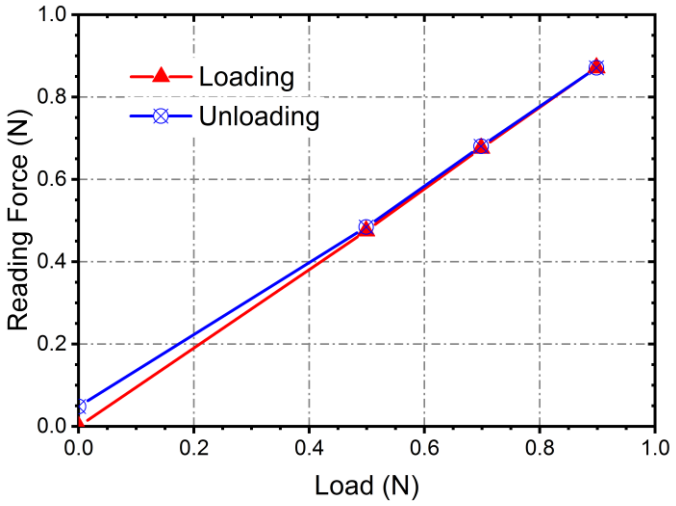

Figure 5.18 Hysteresis Test curve for the force test device.

5.3.4 SMW force tests

Three wires with different diameters were used in these tests to find the relationship between the diameters and generated forces. The sizes of the diameters were (0.25mm, 0.5 mm and 1 mm). Three specimens with 1mm diameters were tested first. They were activated using hot air and used the 90º pad test. Figure 5.19 shows the results. The start activation temperature is between (51–55º C) and the austenite finish temperature is between (72-76º C). Furthermore, it can be seen that the generated forces reach a steady state at 1N for the finish temperatures.

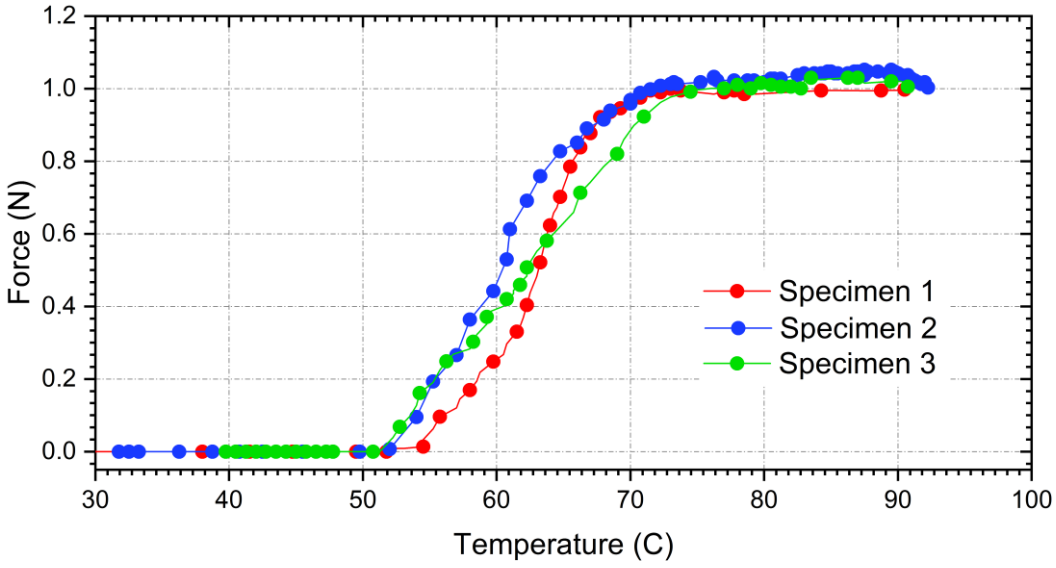

Figure 5.19 Activation curve for BSW actuators (1 mm Diameter, 90º folding angle) using hot air activation process.

Nine BSW specimens were tested using different angle pads so as to find the effects of the folding angle on the generated force. Six specimens have 1mm diameter and other three have 0.5 mm diameter. They were tested using (30^{o} ,60^{o} and 90^{o}) angles of folding pads and were activated using hot air. The results are shown in Figure 5.20 which shows that there is a very slight difference between the amount of generated forces (less than 0.04N) at different folding angles. Furthermore, it is clear that the diameter of the wire has a large effect on generated forces. The generated forces are between (0.95-1.06N) when the diameter is 1mm. With a diameter of 0.5mm, the generated forces are between (0.45-0.51N).

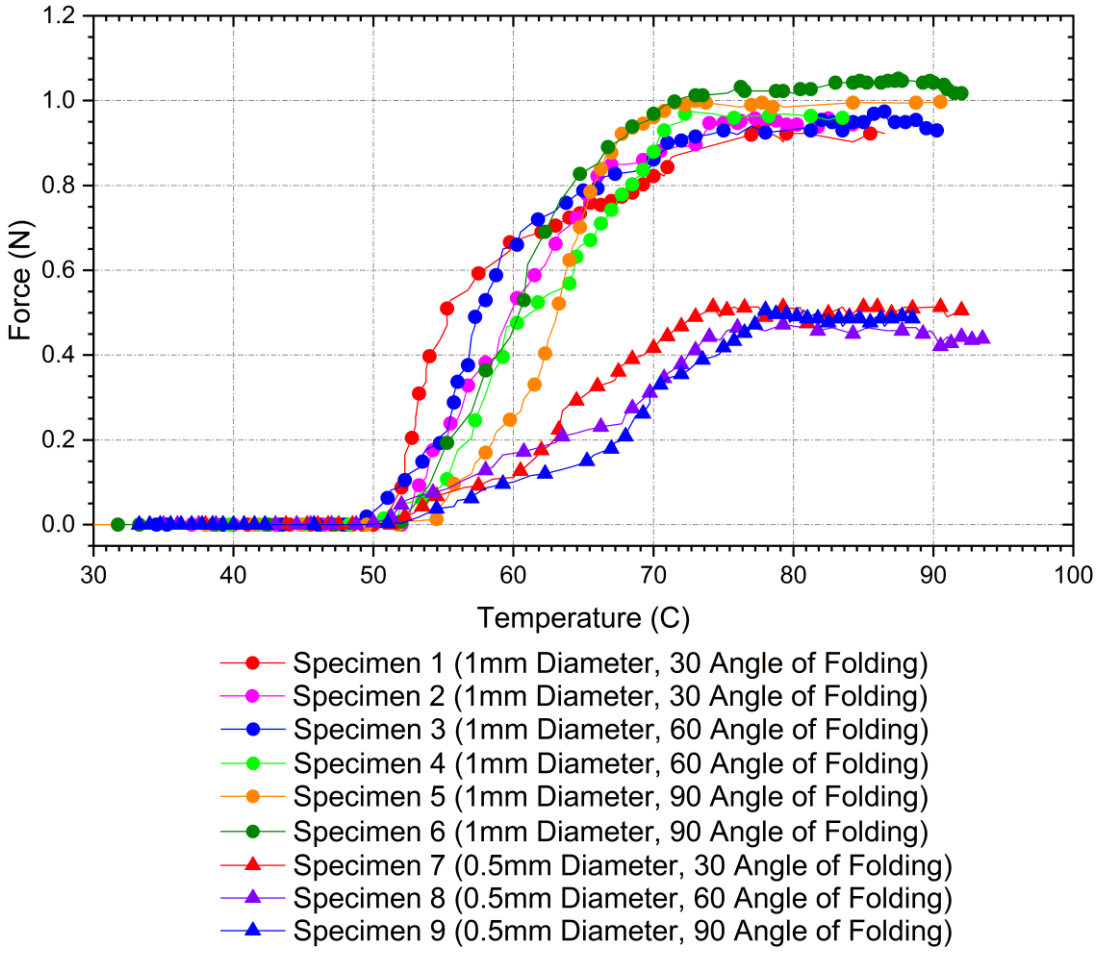

Figure 5.20 Activation curve for BSW actuators with different angles of folding using the hot air activation process.

The next test focussed on the effect of the wire diameter on the generated force in BSW actuators. Four specimens were used in this test. They were tested using hot air activation and 90 degree angles of the folding pad. The results are shown in Figure 5.21. It is clear that the generated force is increased when the size of the diameter is bigger. The steady state generated force for 0.25mm diameter is 0.2N and for 0.5mm diameter is 0.49N. The results show stability in the activation process for all diameter sizes and they have nearly equal activation temperatures. The start activation temperature is between (51–54C) and the austenite finish temperature is between (72-78C).

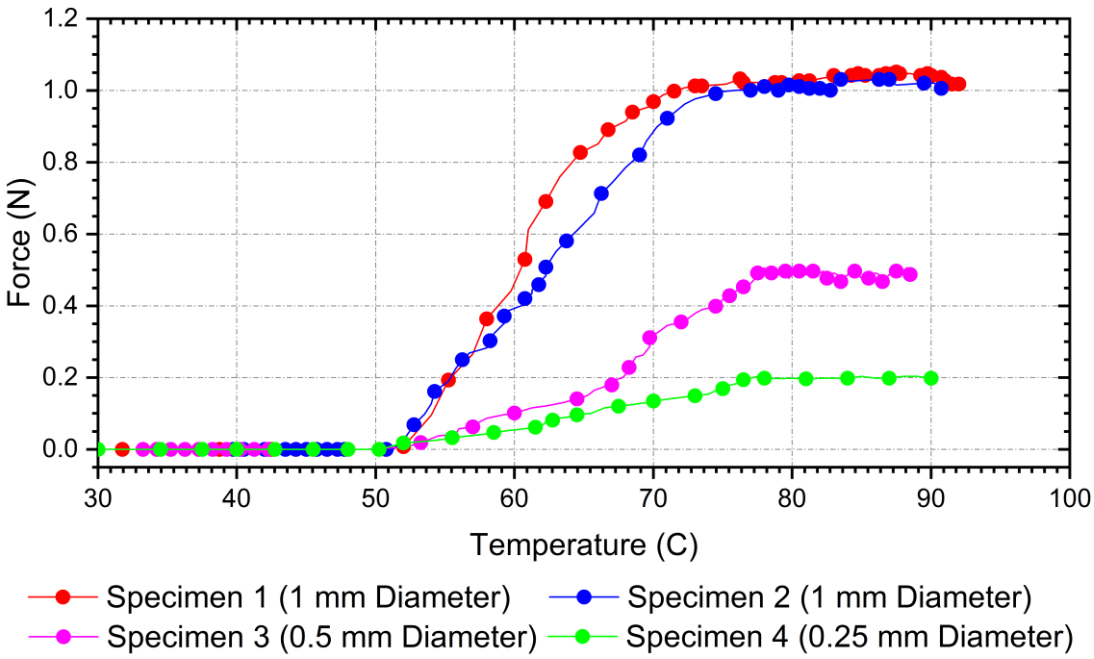

Figure 5.21 Activation curve for BSW with the 90º folding angle and different diameters sizes using hot air activation process.

Moving to the TSW actuators, four TSW specimens that have different diameters sizes (two with 1mm diameter and other two with 0.5 mm diameter) were tested using 90 folding angle pad and hot air activation. Figure 5.22 shows the results. The start activation temperature is between (50–55C) and the austenite finish temperature is between (71-79C). The steady state generated force for 0.5mm diameter is 0.45N and for 1mm diameter it is 1N.

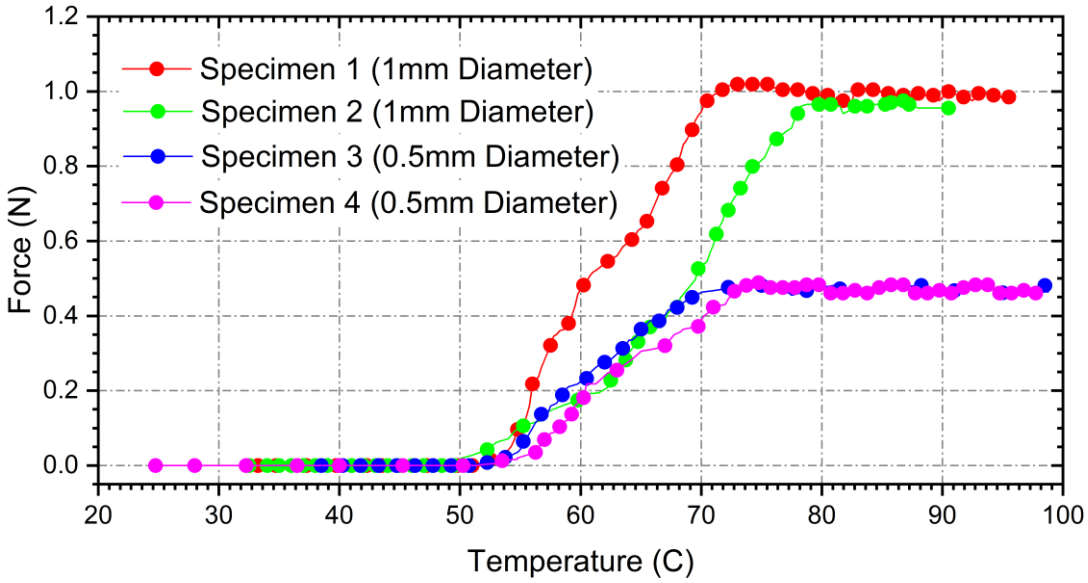

Figure 5.22 Activation curve for TSW actuators with the 90º folding angle and different diameters sizes using the hot air activation process.

It is clear that the TSW actuator produces force nearly equal to the force that is generated from BSW actuator. In Figure 5.23, the results of four specimens were put, two BSW actuators and two TSW actuators, that have the same diameters (1mm) and for the same folding angle pad (90º). It is clear that the results of the generated forces are nearly equal.

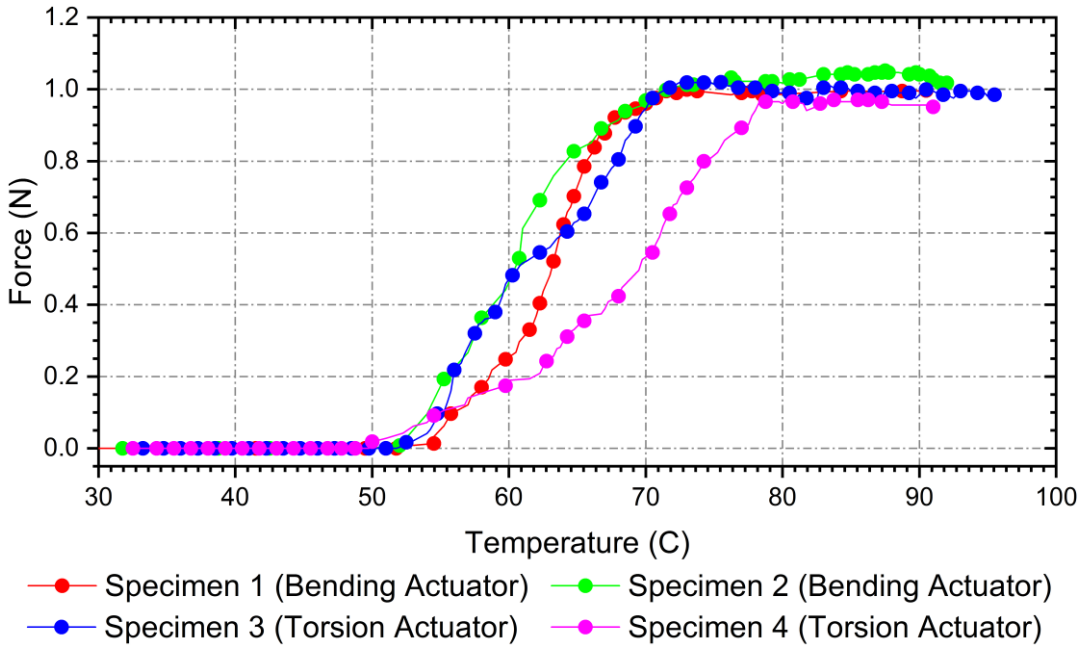

Figure 5.23 Activation curve for BSW and TSW actuators (1 mm Diameter, 90º folding angle) using hot air activation process.

The final test illustrates the effect of the activation type on the generated forces. Four BSW specimens made from Nitinal (NiTi) SMA wire were tested. These specimens have the same diameters (1mm) and same folding angle (90). Two of them were activated using hot air and the other two specimens were activated using electric hating (Joule heated). The results are shown in Figure 5.24. It is clear that the activation type has no effect on the amount of the generated force. There is a slight difference between the results but it is so small that it could be neglected. The start activation temperature and the austenite finish temperature are in the same range as in previous results and that is expected because the activation temperature is a material property and it is not effected by activation type.

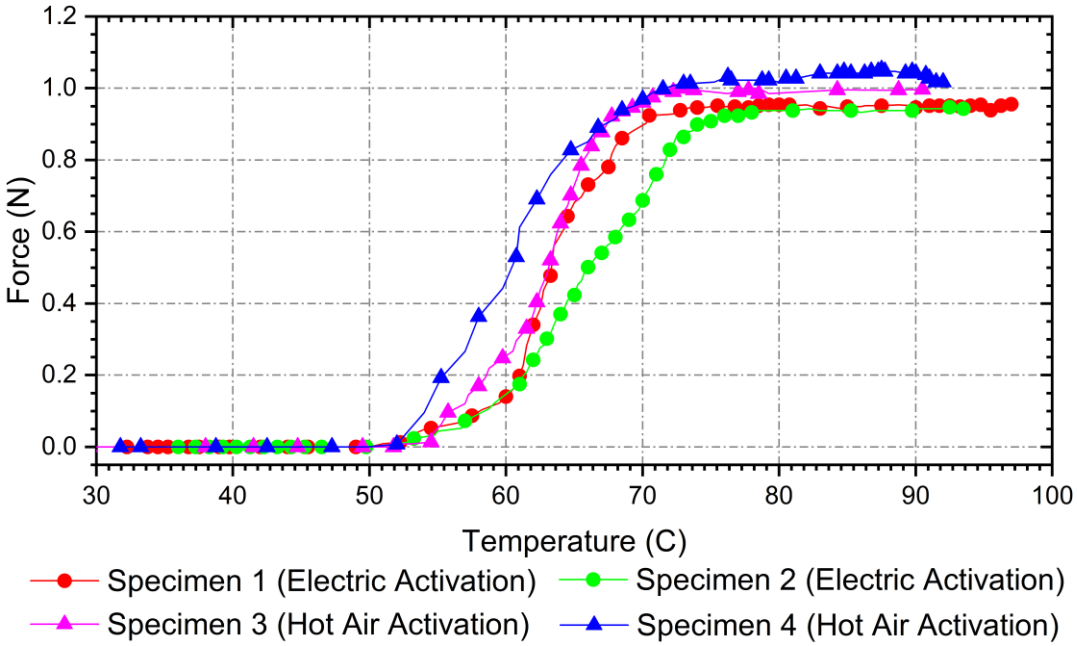

Figure 5.24 Activation curve for BSW actuators (1 mm Diameter, 90^{o} folding angle) using two types of the activation process.

The overall results of tests show that the wire diameter is a very effective parameter to determine generated forces and other parameters have no effects or have very small effects. The average generated forces are 1N, 0.45N and 0.2N for 1mm, 0.5mm and 0.25mm diameters of SMA wire, respectively. The range of start activation temperature is between (50–55C) and the range of austenite finish temperature is between (70-79C).

5.4 Discussion

The actuation system depends on the specification of the robot structure. Speed, accuracy and a large amount of force are required in the case of the manipulation structure OSM. Therefore, the external actuation is the right choice to actuate this type of structure because the actuators are placed outside the structure and that means it can be used at any high speed and heavy duty motors as an actuator. However, this actuation system required a force transmission system that can transmit these amounts of force without breaking.

Two types of force transmission tools were tested; the SK75 Dyneema rope and the 3D printed chain. The results show that the SK75 Dyneema rope has a breaking load of 728N. This is a very big load that is more than that is needed for the manipulation structure. Meanwhile the results of breaking load for the 3D printed chain are very small compared with the breaking load of Dyneema rope. Three different results were obtained when the breaking load of the 3D printed chain was calculated. The analytical result is 39.27N, the FEA result is 23N and the empirical result is 4.05N. The difference between the analytical result and the FEA result was expected because the analytical calculation depends on the maximum shear stress theory (Tresca yield criterion) while the FEA calculation depends on the Von Mises theory. The unexpected result is the empirical result. This result gave the fact that every small-scale design is fabricated by using the 3D printer and should be tested before use because the 3D printed process is not ideal to produce the same big scale material properties.

With all the benefits of the external actuation system it cannot be used as an actuation system for the self-folding structure because the complication of the self-folding process would require a huge system of force transmission to operate it. Therefore, embedded actuation with smart materials is the suitable system for the self-folding structure. The SMA wire is used to fabricate different types of actuators that could work as an embedded actuation system.

The results of testing the two types of the SMA wire actuators show that the BSW actuator and the TSW actuator gives the same amount of force for the same diameter. Also, this amount of force is suitable to fold a hinge made from 3D printed material or by using the Kapton-acrylic approach. The results show that the amount of generated forces for different angles of folding are equal and that is because the generated force in every angle of folding was tested separately and without any external load.

5.5 Conclusions

Two main approaches of actuation are suggested to provide the actuators for the origami structures. These approaches are external actuation and embedded actuation. The external actuation was described and two types of force transmission systems were analysed, which are force transmission using string, and force transmission using 3D printed materials.

After testing the force transmission systems, it is found that the SK75 Dyneema rope is suitable as an actuation system to operate the OSM structure. It is flexible, low stretch and has a high breaking load. The results show that the 3D printed chain has very small breaking load and it cannot used as a force transmission tool. This result means that it will not be possible to fabricate a successful “print to go” 3D printed OSM structure.

The embedded actuation was proved to be the feasible actuation system for the self-folding structure after testing the BSW and TSW actuators. The results show the ability of these actuators to fold 3D printed hinges and Kapton -acrylic hinges.

The next step was to combine the OSM structure with the external actuation system in order to build an OSM-bot (Origami structure for manipulation robot). Merging the 3D printed structure, (that has hinges printed using Tango plus material), with SMW actuators to provide a self-folding structure was another step towards realising self-folding structures.

Chapter 6 DESIGN AND FABRICATION OF FOLDING STRUCTURES

6.1 Introduction

The three steps to the fabrication of any folding structure are; studying the geometry of the structure; choosing the material; and choosing the actuators that provide the folding forces. The geometry and kinematics of the origami structure, and the design of structures that are suitable for use as an origami robot arm were investigated in chapter three. In chapter four, the ability to use 3D printed materials to build a hinge was examined and proved. Furthermore, the behaviour of Kapton as a material to use as a fluctuation hinge was investigated. Chapter five discussed the actuation systems and the differences between them. To build a folding robot, all the information from the three previous chapters had been used and the technology was integrated to create a self-folding structure and an origami robot arm.

Therefore, the fabrication of self-folding samples by using three different methods and materials are illustrated in this chapter. The fabrication of the OSM-Bot is demonstrated in this chapter. Furthermore, the OSM-Bot behaviour and motion are examined, and the results are shown. Finally, there are conclusions.

6.2 Fabrication of Self-Folding Structures

Self-folding structures are made from a continuous sheet which has solid faces and fluctuation hinges between these faces with embedded actuators. There are many approaches to fabricate the self-folding structure. The commonly used or the conventional approach is the manual approach. This approach consists of cutting the shape of faces from solid material and sticking them on a flexible

sheet to form the crease pattern manually. The flexible material between face edges works as a fluctuation hinge. The other approach to fabrication is by using laser cutting to cut the solid faces with more precision. After that, the laminar layers that contain a flexible thin sheet between solid faces form the crease pattern. The third approach is by using a 3D printer to print the crease pattern using the multi-material printing technique. This technique prints a structure by using two different materials at the same time; solid material for the faces and soft material for the fluctuation hinges. All these approaches were used to fabricate two simple types of origami structures. These are the origami ball structure and self-folding cubic structure.

6.2.1 Unit Cell of Origami Ball (Waterbomb) Structure

All Tessellation structures consist of several identical unit cells that form the crease pattern, such as Miura origami and origami ball. The design and fabrication of these type of structure can be simplified by designing and fabricating one unit cell and then repeating the process to fabricate the full structure. All three construction methods are used to fabricate the unit cell of the origami ball. Before that, the simulation program V-rep is used to examine the process of unit cell folding. Figure 6.1 shows the folding and unfolding of the unit cell of origami ball with active revolute joints at angles γ_{br} , γ_{bl} and α_b. The maximum activation angles are 90^o.

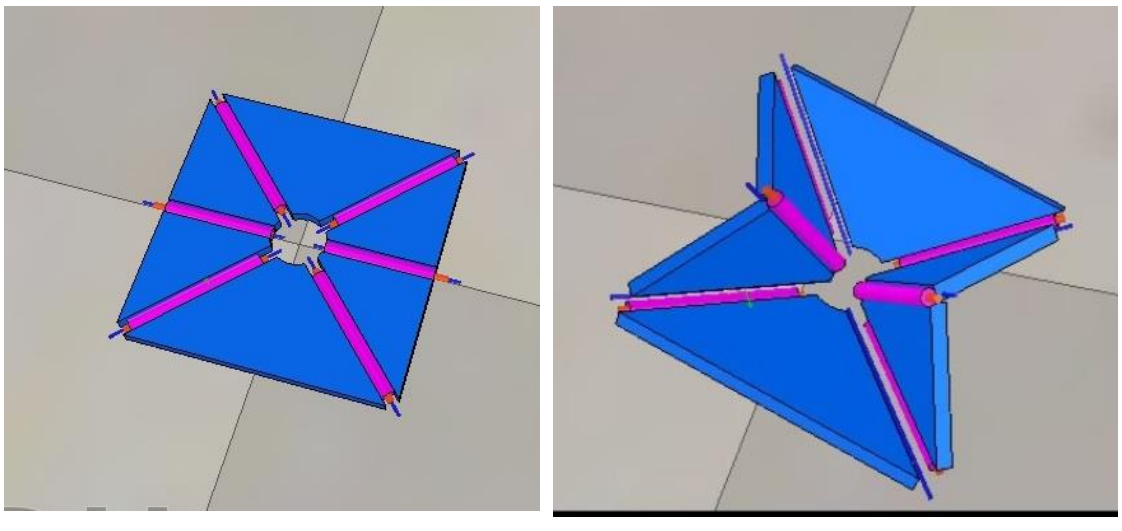

Figure 6.1 V-REP model of the unfolding, and folding of a single origami ball cell with active revolute joints.

The three approaches to fabricating self-folding structures were used to fabricate the self-folding unit cell of the origami ball. The first sample was fabricated by using hard card paper as faces and thin nylon film as a pad to form the fluctuation hinge between faces. After that, three bending SMW actuators (BSW) were stuck on angles γ_{br}, γ_{bl}, and α_b with activation angle 90^o. Figure 6.2 shows the complete folding origami ball after activation by using hot water (70 -90^oC). The folding process took 2-3 sec to complete.

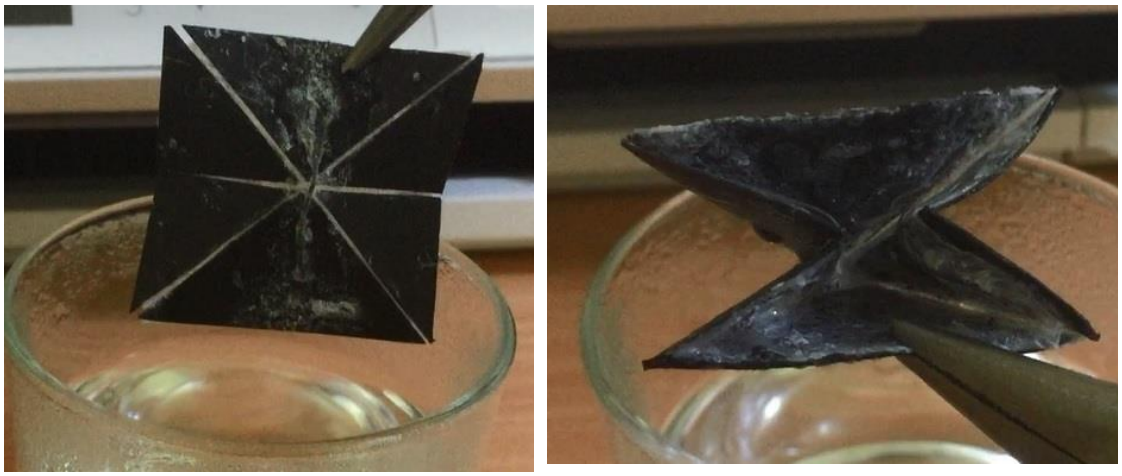

(a) (b)

Figure 6.2 Self-folding paper of a single origami ball cell before and after activation by using hot water (70 -90^o C). (a) before activation (b) after activation.

The same design of the unit cell was fabricated using an acrylic sheet that is cut into triangular shapes to be the faces by using laser cutting. After that, the faces were covered with upper and lower thin layers made from Kapton film to form the final shape of the unit cell. The three BSW actuators were used to actuate the unit cell in the same way as the previous sample. See Figure 6.3. The two layers of Kapton films works as a fluctuation hinge between the solid acrylic faces. The behaver of folding for this sample is the same as the previous sample with folding time of 2-3 sec when using hot water (70-90^oC) as an activation boundary.

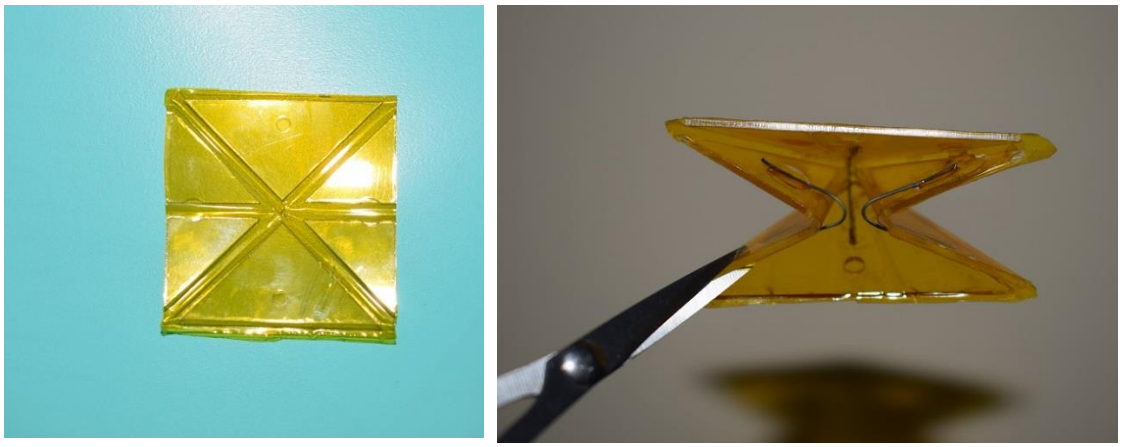

(a) (b)

Figure 6.3 Self-Folding unit cell of origami ball, which is made from acrylic and Kapton, before and after activation by using hot water (70 -90^{o} C). (a) before heating (b) after heating.

The third sample was fabricated using a 3D printer with a multi-material technique. As described in chapter 4, the Vero material was chosen for the faces and Tango Plus flx930 material for the fluctuation hinges. The first attempt to print this sample of the unit cell failed, see Figure 6.4. The figure shows many cracks on the transformation edges. This situation happens due to the transformation process from solid material to the soft material, where gaps appear at the borders. These gaps are formed because some printing lines have no material in the head of the 3D printer.

To solve this problem, A new sample of the unit cell with 0.5 mm overlap of the Tango Plus material on the transformation edges was printed. Figure 6.5 shows that some cracks were formed in the hinges during the folding/ unfolding process. These cracks were formed because of the relatively high thickness of the Tango Plus material. Finally, the solution to the hinge failure was found by making the soft material as a pad layer under the solid faces and making the solid faces as the inner surface during the folding process see Figure 6.6. Figure 6.6b shows the three layers that create the unit cell. The blue layers represent the Tango Plus material, and the red layer represents the Vero material. Every layer has a 1mm thickness. When they were printed; an overlap of 0.25 mm was considered to be between Vero and every Tango Plus layer.

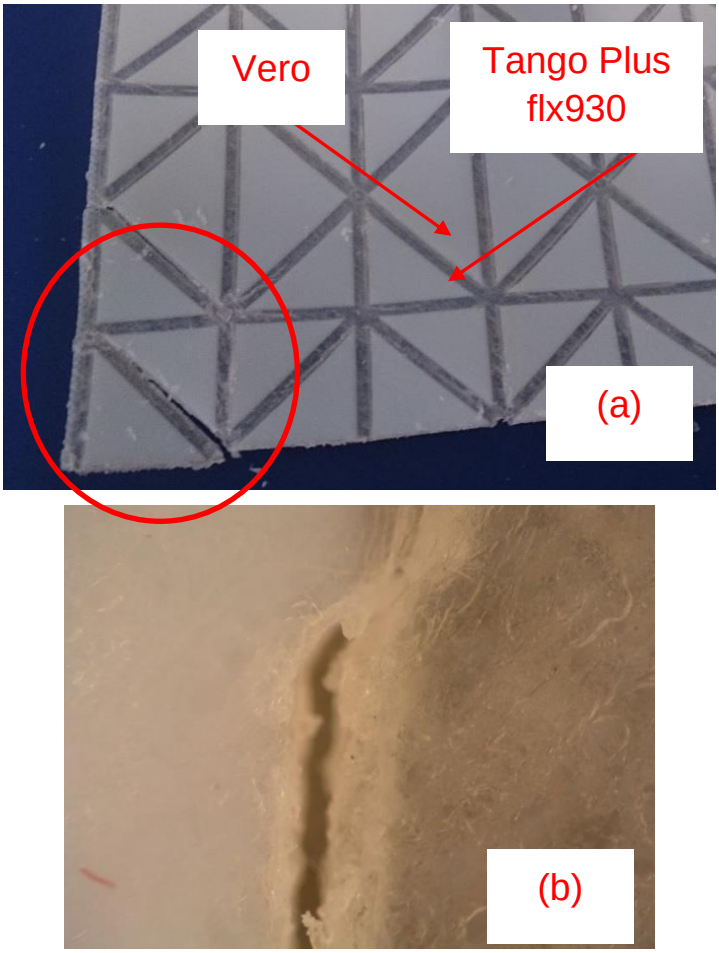

Figure 6.4 (a)Origami ball pattern printed by using 3D printer with multi-materials technique. (b) Gaps at the border between solid and soft material.

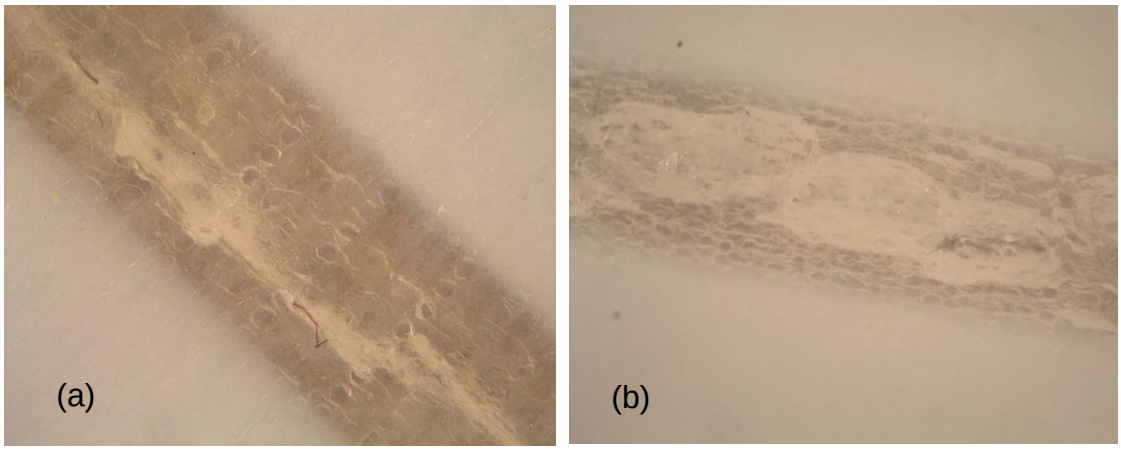

Figure 6.5 Microscopic photos of the hinge printed using Tango Plus flx930 material. (a) Gaps at the border between solid and soft material. (b) The cracks on the surface of the soft material.

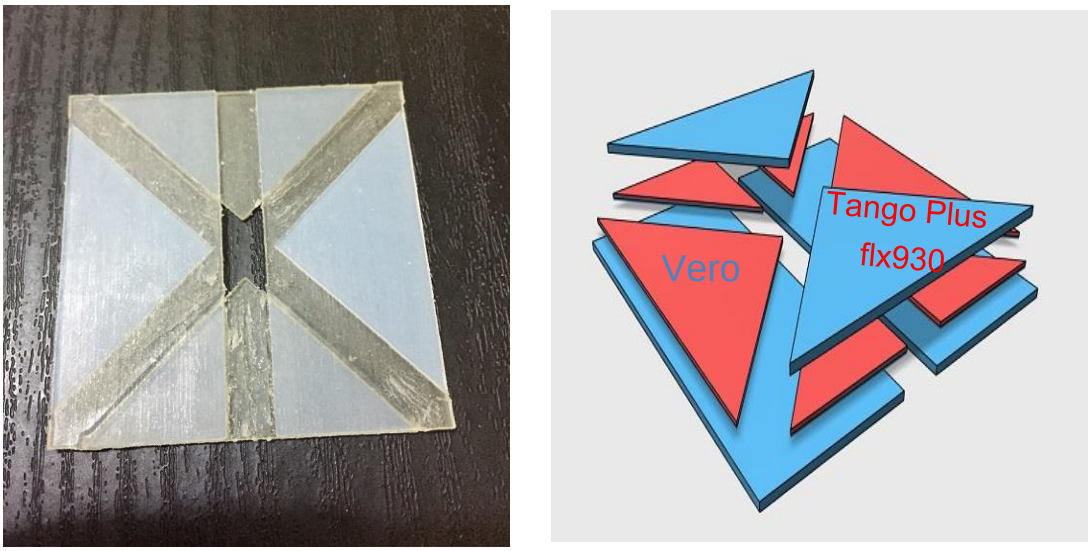

(a) (b)

Figure 6.6 (a) 3D printed Unit cell of Origami ball. (b) The layers of Tango Plus and Vero materials.

6.2.2 Self-Folding 3D Printed Cube

Six square faces and five fluctuation hinges are configurations any folding cube. Figure 6.7 shows the process of folding a cube by using the v-rep simulation program. Five revolving joints with 90^{o} final angle of folding were used. The simulation results shows a smoothly folding process with a suitable stable body. The 3D printed model has been designed using the dimensions 30x30 mm for faces and 5 mm for the width of fluctuation hinges. The faces thickness is 1 mm, and the fluctuation hinges have a thickness 1.5 mm. The model was printed by using the multi-material 3D printed technique and made a Tango Plus pad with 1.5 mm thickness under the Vero faces, see Figure 6.8.

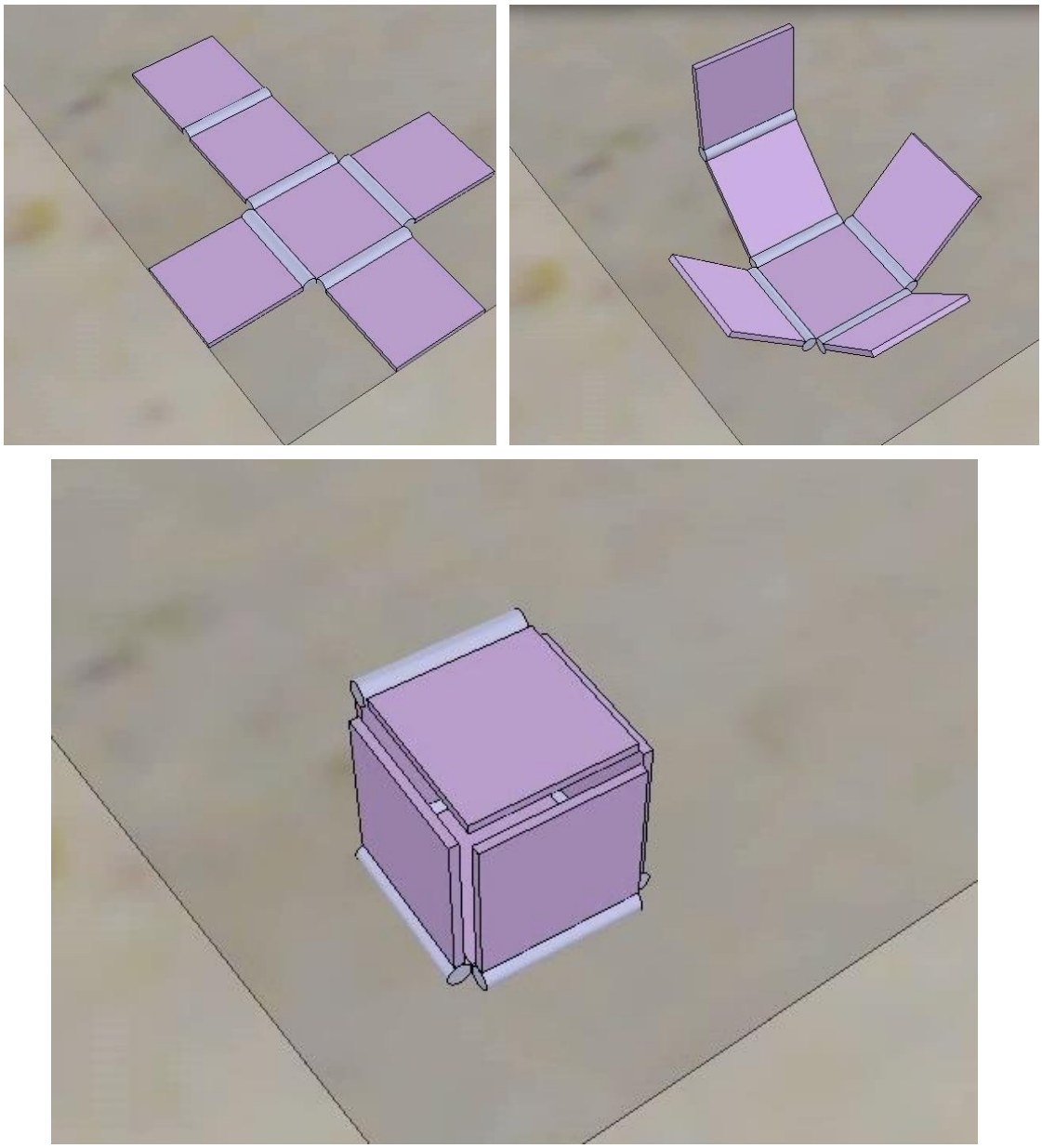

Figure 6.7 V-REP model of the unfolding, and folding cube with active revolute joints.

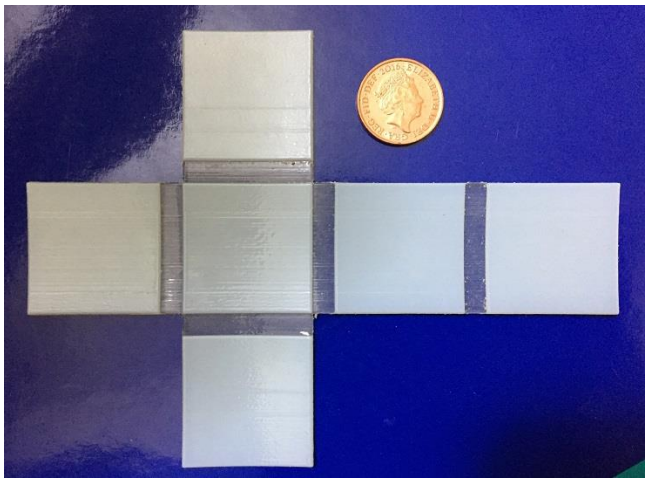

Figure 6.8 Cube pattern printed by using 3D printer with multi-materials technique.

The BSW with 1 mm in diameter is used to actuate the self-folding origami cube. Five BSW actuators with 90^{o} activation angle are stuck to the structure of the 3D printed cube. Each BSW actuator was attached on the outer side of the fluctuation hinges, see Figure 6.9. The self-folding cube was tested under uniform heating by using hot air (90^{o} C-120^{o}C) as an activation boundary. Figure 6.10 shows that the self-folding cube is completely folded in just 19 seconds.

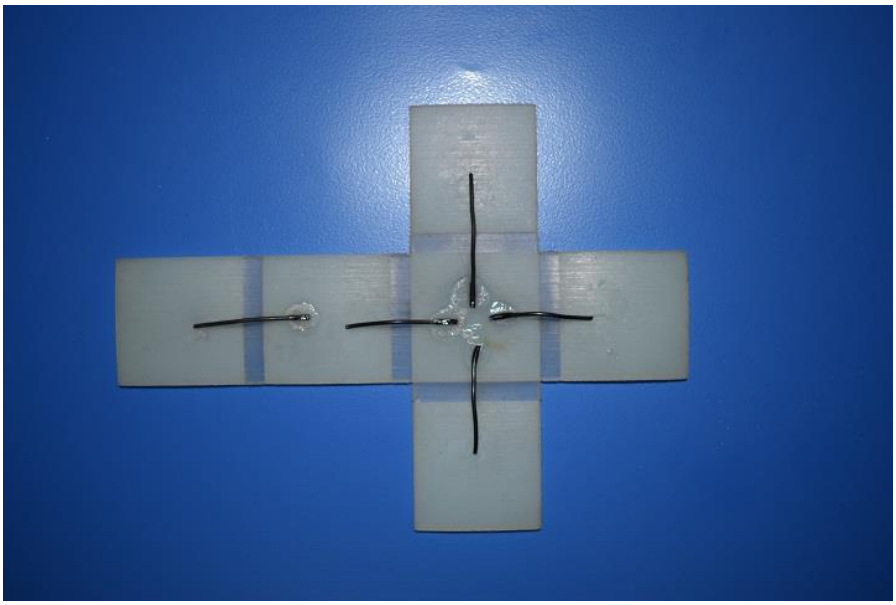

Figure 6.9 Five BSW actuators with 90^{o} activation angle are attached to the structure of the 3D printed cube.

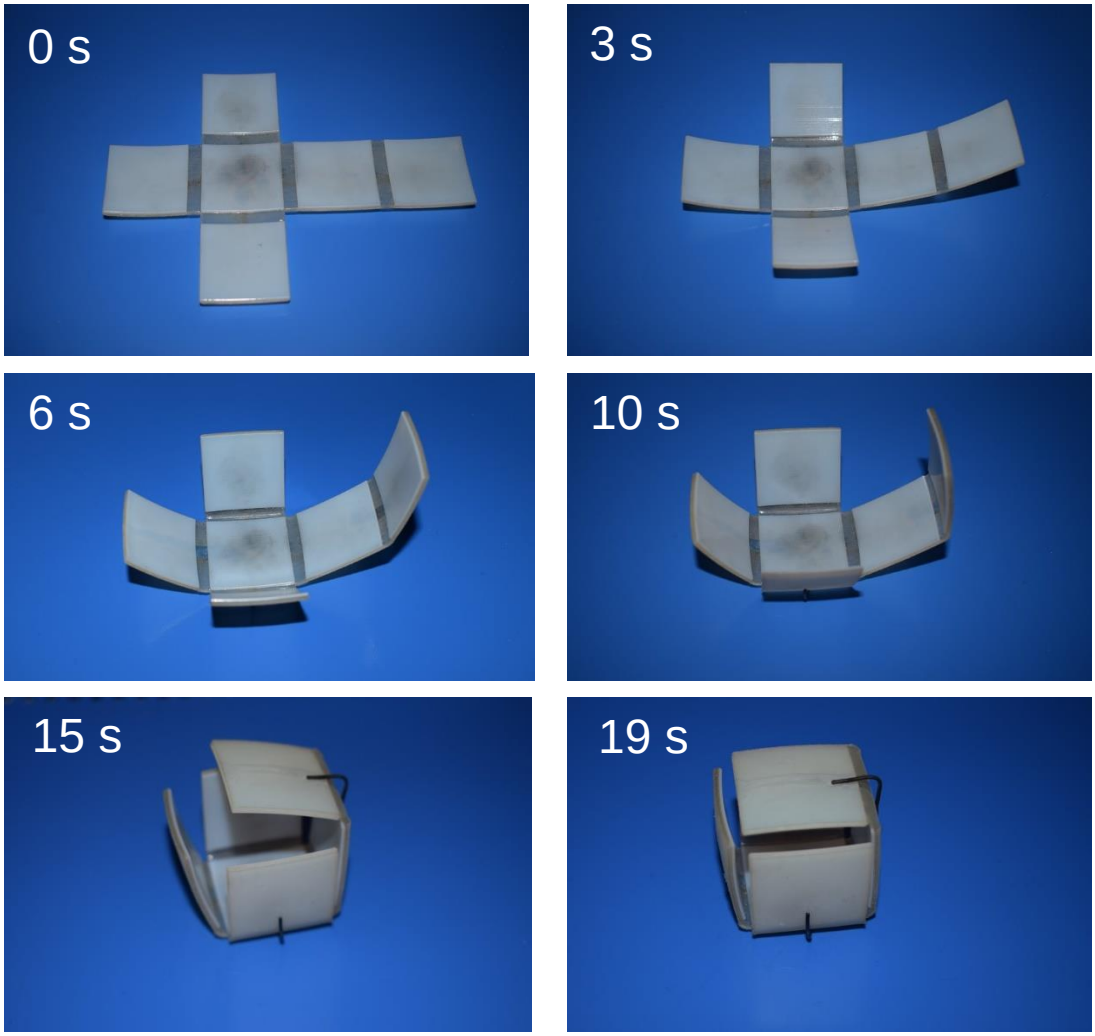

Figure 6.10 Self-folding process by uniform heating.

6.3 Origami Structure for Manipulation Robot (OSM-BOT)

The origami structure for manipulation (OSM-Bot) is a folding structure arm that has four sides of the origami structure which have been described in section 3.8. Every side consisted of four unite cells of origami ball. This unique structure provides an excellent bendability when actuated using a string to pull every side individually. This structure can form an arm with a bend of a small radius of curvature by using three segments.

In section 5.2, the ability to use string to actuate OSM-Bot has been investigated. The actuation system that was used with this type of robot arm is the external actuation system using a rope for force transmission.

The OSM-Bot was fabricated using inexpensive materials. This structure has unique properties. It is a very lightweight robot with high manipulation ability. The soft material that is used to form the fluctuation hinges makes this robot to be soft. It has a soft reflection on any disturbance force. The prototype of OSM-Bot was fabricated using a thick paper to examine the ability to manipulate it.

6.3.1 The Fabrication of (OSM-Bot)

Card paper has been used as a preliminary material to fabricate the prototype of (OSM-Bot). The first step is folding the four sides of the segment. Every side has a crease pattern which contains four unit cells of origami ball set as a column, see Figure 6.11. The dimension of the unit cell is a_b=55 mm and θ=45^o. After folding all the four sides, they are attached from the top and bottom to the square bases, which are made from card paper, to form one segment, See Figure 6.12. The OSM-Bot is made from three segments connected together. See Figure 6.13. Four strings, which are SK 75 Dyneema rope with 1mm diameter, are used as a force transmission mechanism in the actuation system of the OSM-Bot. Every rope is connected with one side and provide a tensile force on that side.

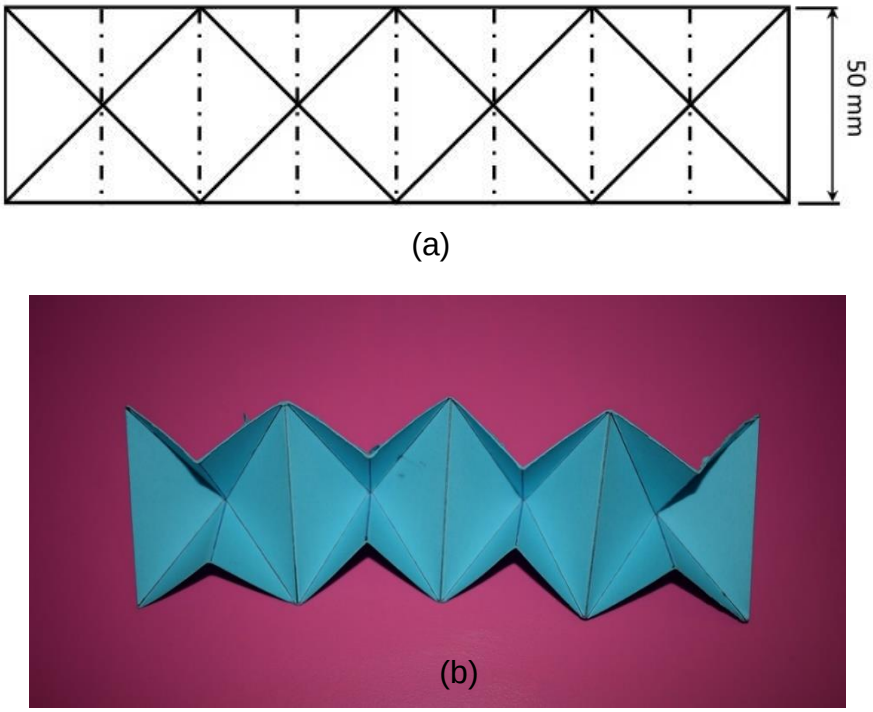

Figure 6.11 One side of paper OSM-Bot. (a) Its crease pattern. (b) Final shape made from card paper.

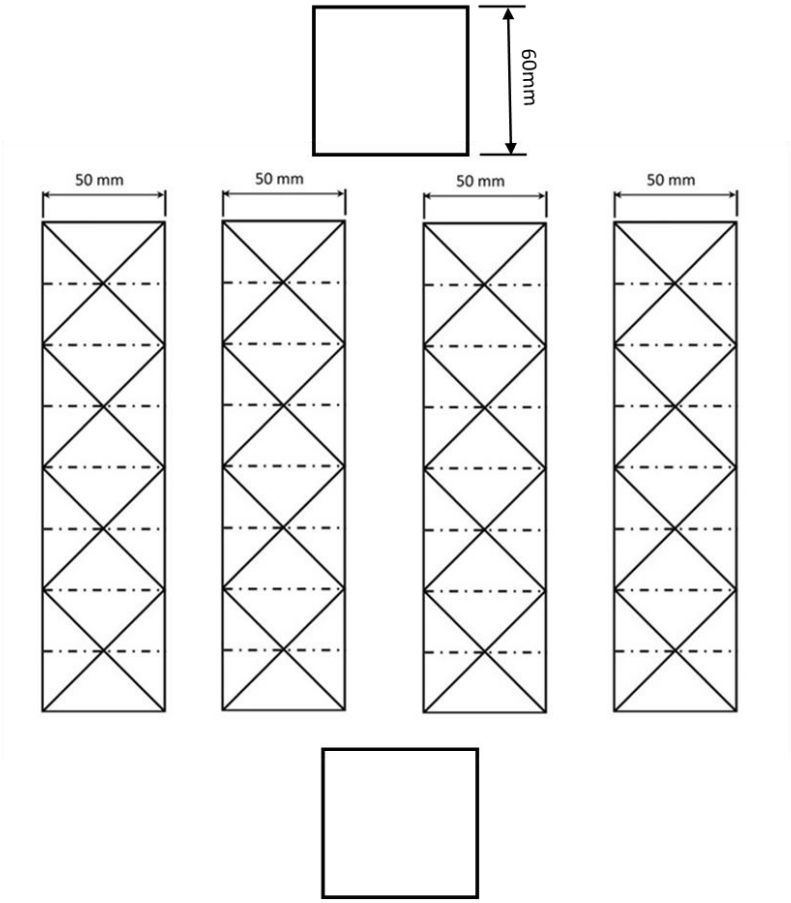

Figure 6.12 Crease patterns of four sides and the top and bottom square bases that form one segment of OSM-Bot.

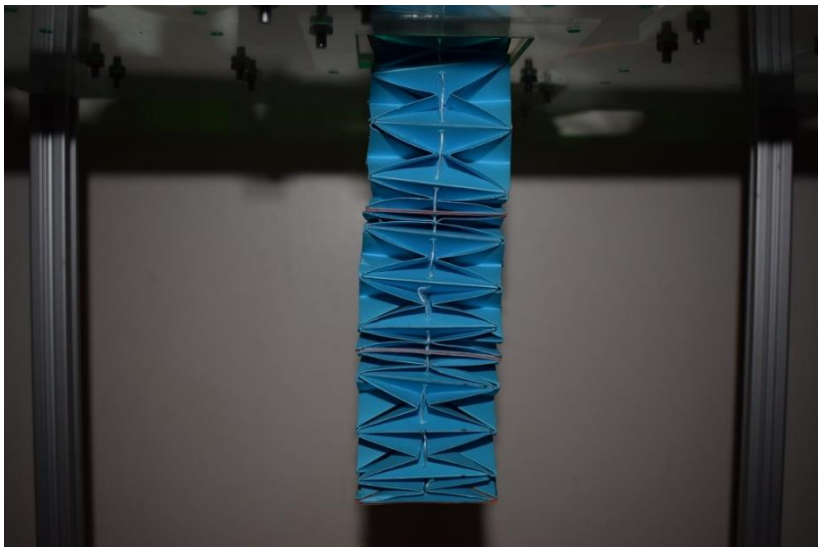

Figure 6.13 The final shape of OSM-Bot that contains three segments of OSM structure.

The actuation system consists of four actuators which are the servo motor type (MG 996R) with metal gear, and the Arduino based controller with a joystick to control and manipulate the OSM-Bot. Every servo motor has a pully with 76 mm diameter. These pullies are pulling strings when they rotate. Figure 6.14.

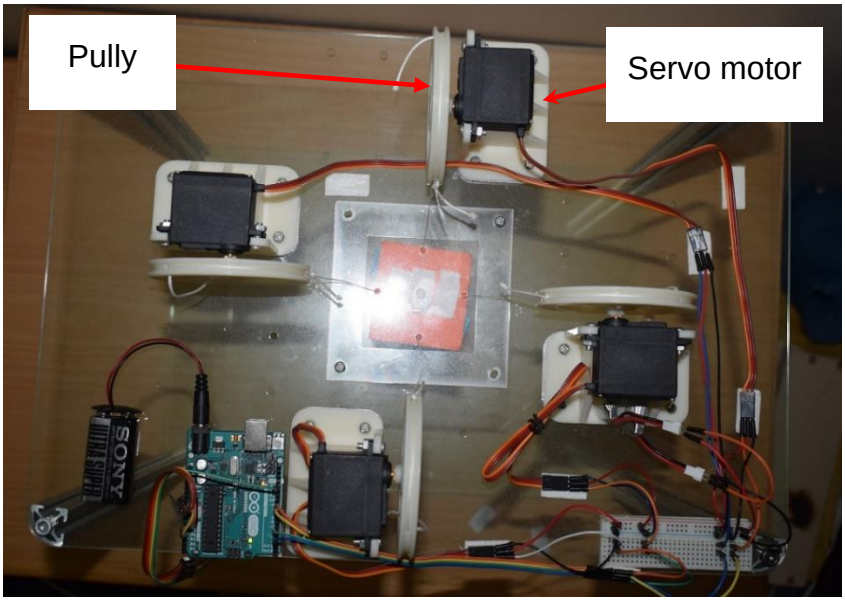

Figure 6.14 The control part of the OSM-Bot.

The bending motions of the OSM-Bot depend on the length of the string on each side of the structure. When the strings do not exert tensile forces on the distal end, and the Z_i axis is colinear with Z_b axis, the OSM-Bot is in its home configuration. By assuming the length of the strings in this home configuration is equal, and it is called Lo, which is also equal to the length of the arm. The bending motion happens when the effective length of each string reduces to Li (Li<Lo), and that occurs when the strings are wound by rotating the pulleys. In this case, the distance between each pair of unit cells is derived as:

$$\boldsymbol{l_i = \frac{L_i}{n}} \qquad \textbf{6-1}$$

Where n is the number of unit cells in each side which is n =12 in the present structure. The angle α_b can be calculated from l_i and that leads to calculating all the parameters of the unit cell of the origami ball that forms the OSM-Bot.

The resistance of paper and the gravity are used to return the robot to its home configuration when the tensile forces are released. See Figure 6.15. The bending motions of the OSM-Bot were evaluated in an experimental test. The four

actuated sides of origami structure have two typical working phases including the bending motion and axial contraction. These phases are enabled by three types of actuation process which are; one string in tension provide tensile force to make bending motion in one side; two string in tension provide tensile force to make a bend in motion in combined axis direction; four strings in tension proved tensile forces to make a pure contraction. See Table 6.1

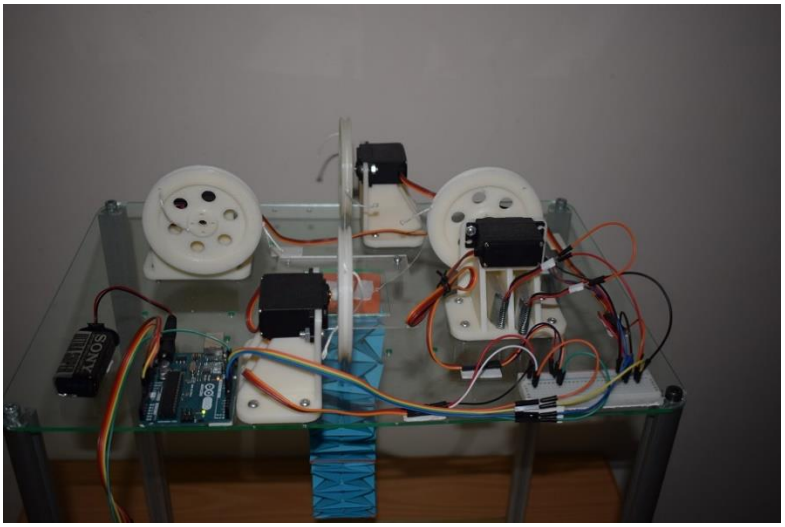

Figure 6.15 The shape of OSM-Bot at its home configuration.

Table 6.1 Working phases of the OSM-Bot.

Working phases	Tensile force(s)	Length of strings			
		L_1	L_2	L_3	L_4
Bending motion	One string in tension	$<L_O$	$>L_O$	$>L_O$	$>L_O$
		$>L_O$	$<L_O$	$>L_O$	$>L_O$
		$>L_O$	$>L_O$	$<L_O$	$>L_O$
		$>L_O$	$>L_O$	$>L_O$	$<L_O$
	Two string in tension	$<L_O$	$<L_O$	$>L_O$	$>L_O$
		$>L_O$	$<L_O$	$<L_O$	$>L_O$
		$>L_O$	$>L_O$	$<L_O$	$<L_O$
		$<L_O$	$>L_O$	$>L_O$	$<L_O$
Pure contraction	Four strings in tension	$L_1 = L_2 = L_3 = L_4 < L_O$			

Figure 6.16 shows the OSM-Bot when it is driven by only one string which provides a tensile force to bend the robot in one direction. The experiment shows that one string in tension leads to bending motion in a normal plane that contains the path of the string in tension and the maximum bending angle is almost 180^{o}. Figure 6.17 shows the OSM-Bot when it is driven by two strings which provide tensile forces to bend the robot in a normal plane that lies in the middle between two strings paths and make an angle of 45^{o} with them.

The experiment result proves the ability of manipulation for this novel origami robot which can provide mixed contraction and bending motion. These types of motion and characteristics of the OSM-Bot make it a potential solution for many applications cases such as whole arm manipulation, snake, and worm robots for locomotion.

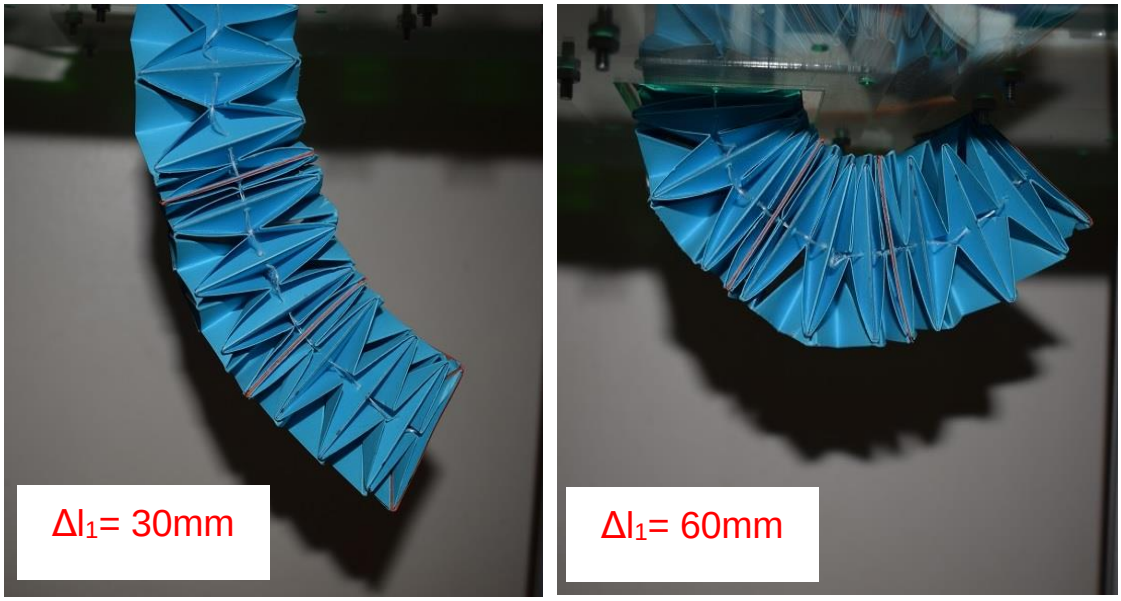

Figure 6.16 Bending motion generated by one tensile force.

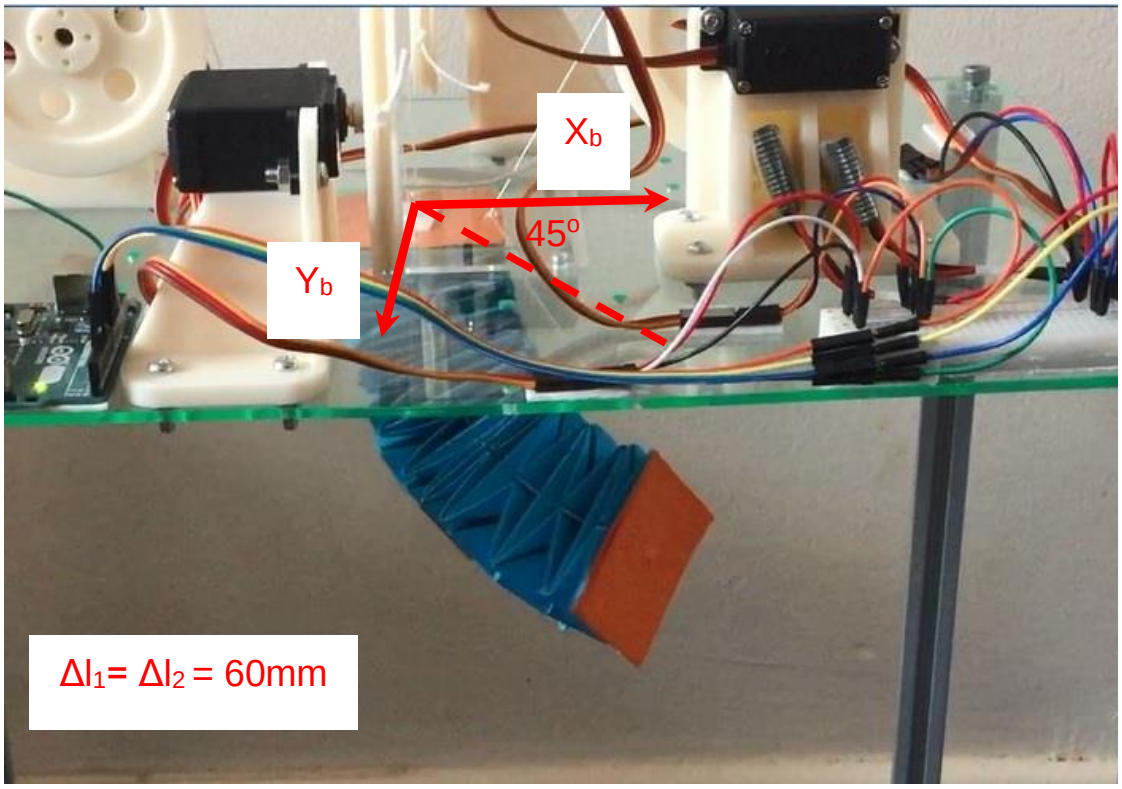

Figure 6.17 Bending motion generated by two tensile forces.

6.3.2 Fabrication of OSM-BOT using Acrylic and Kapton

Acrylic with 1 mm thickness was used to fabricate the faces of the origami structure that form the OSM-Bot. A laser cutting machine was used to cut the acrylic into a precise shape. After that, two layers of Kapton are used on the top and bottom of the acrylic faces to hold together all the structure. 4 mm gaps between faces that contain two layers of Kapton represent the fluctuation hinges, see Figure 6.18. The figure shows the steps in the fabrication of the sides of the OSM-Bot segment and the final shape of the OSM-Bot arm. The SK75 Dyneema Rope with 1 mm in diameter is used to transmit the tensile force from actuators.

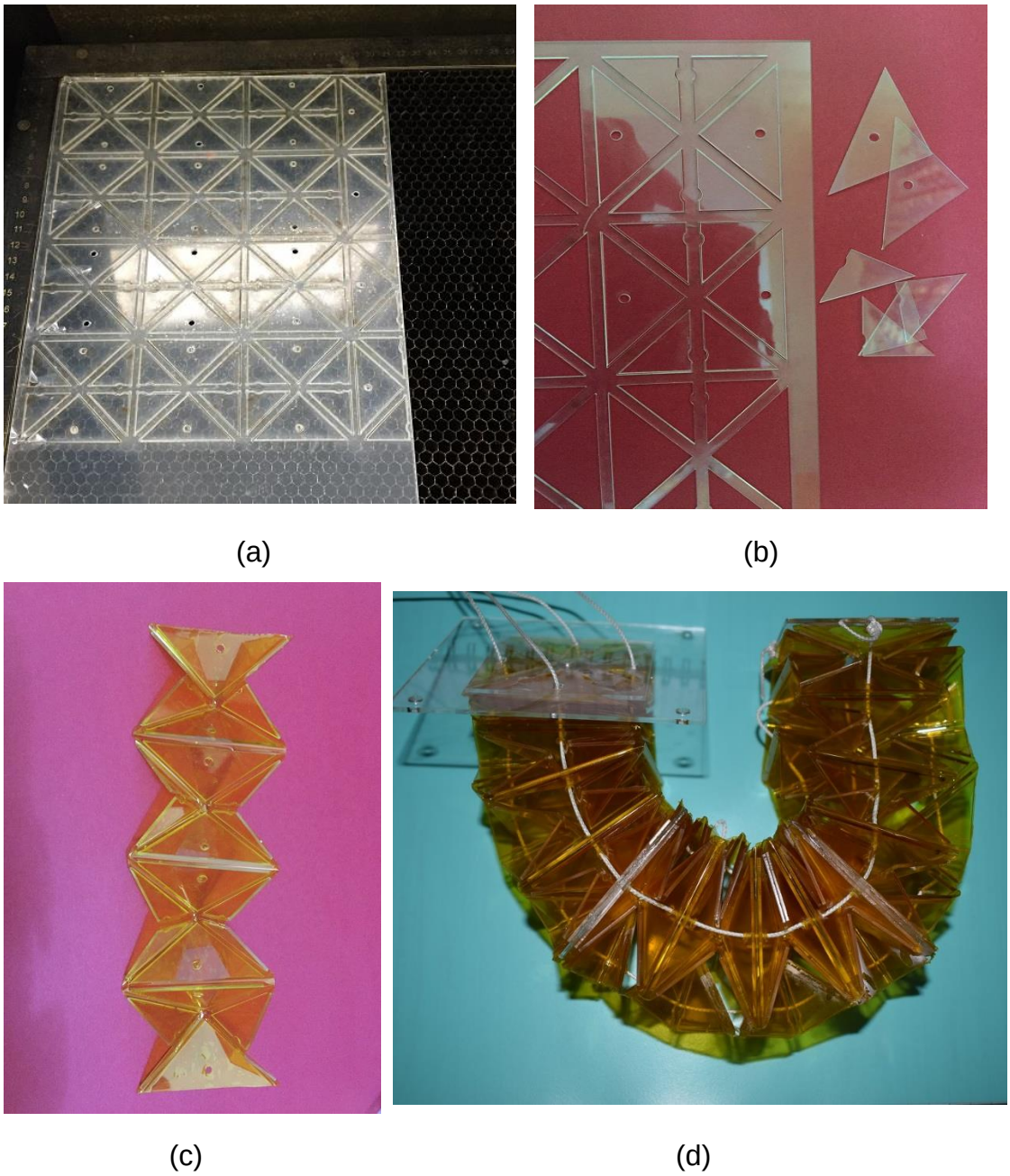

Figure 6.18 The steps of fabrication the sides of OSM-Bot segment and the final shape of OSM-Bot arm. (a) laser cutting of the acrylic sheet. (b) cut pieces placed on a Kapton sheet. (c) four cells side. (d) final shape of OSM-Bot.

To calculate the force required to manipulate the acrylic Kapton OSM-Bot; first, the weight of the structure should be calculated. The structure contains 48 unit cells of origami ball with 55X55 mm dimensions and three bases with 60X60 mm dimensions. The volume of the whole acrylic material was calculated to be equal to 130 cm^3. By knowing the density of acrylic, which is ρ_a =1.19 g/cm^3, the weight is determined as $W_a = \rho_a \times V_a$ = 155 g. By adding the weight and resistance of

Kapton, the force required to manipulate acrylic-Kapton OSM-Bot Would be approximately 2.5-3.5 N.

When the acrylic-Kapton OSM-Bot is tested in the same way as in the previous section 6.3.1, the structure fails to return to its home configuration, see Figure 6.19. The reason for failure is that the resistance and stiffness of the Kapton is not enough to hold the weight of the structure. Therefore, it is required to add a high stiffness material such as springs or metal rod to provide the stiffness that can return this structure to its home configuration.

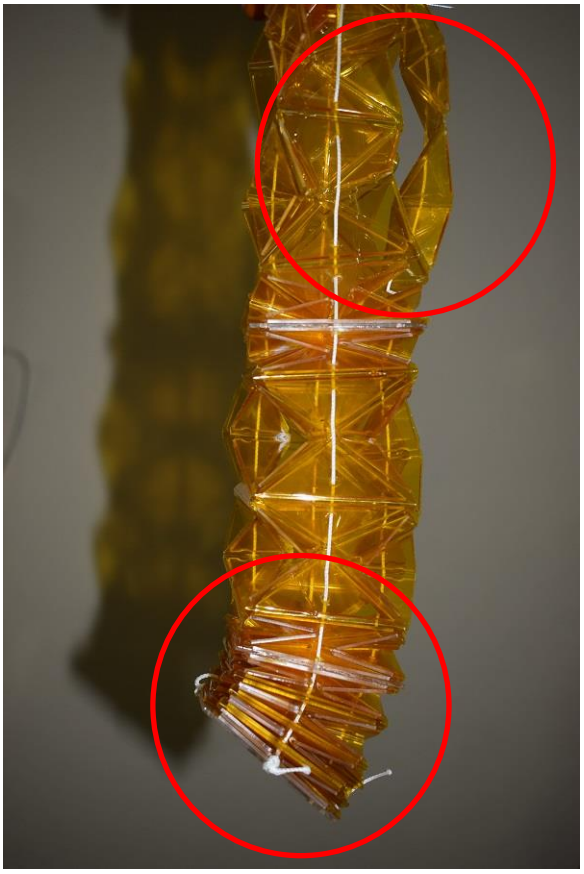

Figure 6.19 The acrylic-Kapton OSM-Bot during the test.

6.3.3 The Ability to Fabricate the OSM-BOT using a 3D Printer

The OSM-Bot consists of three segments of the origami structure. Every segment has four sides, and every side has four unit cells of the origami ball. It is required to design the structure that has 48 unit cells to fabricate the OSM-Bot

using a 3D printer. Every unit cell should be printed using the multi-material technique as was explained in section 6.2.1, see Figure 6.6.

The first step to examine the fabrication of the OSM-Bot using a 3D printer is to calculate the weight of the structure. The structure contains Vero material with density 1.18 g/cm^3 and Tango plus with density 1.17 g/cm^3. The Vero volume is calculated by determining the volume of faces in all 48 unit cells and adding them to the volume of the three bases. The volume of Vero material is equal to 195 cm^3, and the volume of Tango material is equal to 70 cm^3. The weight can be calculated from multiplying the density by volume. The overall weight of OSM-Bot is 312 g =3.12N.

The resistance of Tango plus material in the fluctuation hinges should be considered to determine the overall force required to manipulate the OSM-Bot. From figure 4.15 and by using the approximate angle of folding as 80^o , the force required to fold all fluctuation hinges can be determined as 17-20 N. by adding this force to the weight, the overall force required to manipulate the structure will be between 20-23N. However, the maximum load that is calculated for the 3D printed chain is equal to 8.3N, see figure 5.12. This mean that the 3D printed structure OSM-Bot with a 3D printed chain which worked as a force transmission can fail during operation (especially during the one side bend operation). Furthermore, the weight and the forces required to manipulate the OSM-Bot increases the strain at the base unit cell (The first unit cell in upper segments) and that leads to an increase in the likelihood of fatigue failure in the fluctuation hinges of these unit cells.

6.4 Conclusions

The chapter describes the design and fabrication of origami structures. A self-folding unit cell of Origami ball is fabricated by using three approaches. The first approach is to fabricate manually by using card paper and a thin sheet of nylon. This paper unit cell is actuated with BSW actuators and is activated by uniform heating. The self-folding unit cell folds smoothly in just 3 seconds. The second unit cell, which is fabricated by using acrylic and Kapton gives the same result.

The third approach to fabrication of the self-folding structure is by 3D printing with a multi-material technique. The samples made by 3D printing had many issues in the transformation section at a hinge line. The issues are at the transition between hard (Vero) material and the soft material during printing.

These issues are solved when using the soft material Tango Plus flx930 as a pad under the Vero faces. A self-folding cube was fabricated by using this 3D printing approach. The cube was activated by using five BSW actuators with uniform heating activation. The cube operates a stable folding process within 19 seconds.

The fabrication of the OSM-Bot is illustrated in this chapter. It is fabricated using paper cards and actuated using the external actuation system that has four servo motors and Sk75 Dyneema rope for force transmission. The OSM-Bot shows the ability to be manipulated using contraction and bending motion in four directions. Two other ways to fabricate the OSM-Bot are investigated: the acrylic-Kapton with laser cutting approach, and the 3D printing approach. The two methods fail to build a stable OSM-Bot structure that could operate like the card paper origami structure.

Chapter 7 CONCLUSION AND FUTURE WORK

7.1 Assessment of research objectives

Five research objectives were outlined in section 1.3. This section identifies the extent to which they have been fulfilled during this study:

1.Explore the geometry of origami structures and their ability to operating tasks.

Chapter two reviewed research that examines the origami structure ability to self-folding and manipulation tasks. These researches contain self-folding robots that are inspired by the origami structure. Other research studied the ability to use the origami structure as a worm-like robot.

Chapter three investigated three types of origami structures: Miura origami, origami ball, and Twisted tower origami. The mathematical models of Miura origami and origami ball were derived. And their effective angles were calculated. The ability of self-folding for these structures was studied, and the result that was illustrated found that the unit cell of origami ball and Miura origami can be used as a self-folding structure.

In chapter six, the self-folding unit cell of origami ball is fabricated and examined. The result shows a stable and smoothly self-folding process.

2.Explore the material properties of 3D printed structures.

In chapter four, the use of 3D printed material as a hinge was investigated. The Tango Plus flx930 was tested to use in a flexure hinge. The result of the tensile test and fatigue test proved that the Tango Plus flx930 could be used in a flexure hinge with an appropriate limit of working life. The equation that calculated the

force required to fold a hinge made from Tango Plus was obtained from the result of the bending test.

In chapter five, the chain made with Vero material was tested as a force transmission tool for an external actuation system for a 3D printed structure. The tensile test provides a result less than the expected and that leads to excluding the use of Vero chain as a force transmission tool.

The 3D printed multi-materials technique was used to print a unit cell of origami ball and cube in chapter six. This technique was investigated and resulted in many failures before a new hinge design was created that worked well. The new design used a Tango plus pad under the Vero faces. This type of hinge gave a suitable result when it was tested.

3.Investigate actuation systems for folding structures.

Chapter five investigated two actuation systems: external and embedded actuation system. The external actuation system was used in a folding structure that is used for manipulation, such as a robot arm. This type of system required force transmission tools. In the same chapter, the SK75 Dyneema rope was tested, and the result shows a very high breaking point. That is mean, this rope is a suitable choice to use as a transmission tool for the external actuation system.

Another type of force transmission was tested in chapter five, which is the 3D printed chain. This chain does not provide a suitable tensile strength when it was tested, and it could not use as a force transmission tool. The embedded actuation system was studied, and the use of smart material as actuators was investigated. The smart material that was tested to use as an actuator was SMW. The result shows long activation time but with suitable force provide. This result made the SMW be a proper actuator that could be used in a self-folding structure.

4. Explore the behaviour of the shape memory alloy(SMA) actuators.

As it was explained in the previous point, the SMW was tested in chapter five. The test was used to calculate the activation temperature and the force provided by SMW actuators. The result shows that the activation temperature between (50-79^{o}C) and the providing force depends on the diameter of the SMW. Two types of actuators were used BSW and TSW. These two types provide the same force for equal diameters when they are tested.

5. Design and fabricate an origami robot arm.

A new and novel type of origami structure for manipulation was created and explained in chapter three. This structure (OSM-Bot) has great bendability and soft reaction to any disturbing forces. Its structure depends on the behaviour of the unit cell of the origami ball, which is considered to be the element that created the OSM-Bot.

In chapter six, the OSM-Bot was fabricated and tested. It was controlled using an external actuation system which consists of servo motors and force transmission ropes. The OSM-Bot provides a great ability to bend as well as to contract, and it has four DOF.

7.2 Conclusion

The fabrication of an origami folding robot requires the study of different aspects. The first aspect of investigated is the origami structure. After many types of origami structure were investigated, the best one to be used in a self-folding structure is the Tessellation origami. These types of origami have excellent performance and properties such as low bend stiffness, shape morphing, and high ability of contraction.

The unit cell of the origami ball can build a new type of structures that has low bend stiffness. These structures could be used to construct a folding arm robot.

Modular origami could use to build a low bend stiffness structure but could not apply in the application of the self-folding robot. The reason is that the self-folding structure required a continues sheet origami pattern.

The material is the second thing that is required to study for fabrication folding robots. The essential part of the origami structure is the hinge. Therefore, the material that forms the hinge must be carefully selected and tested. The 3D printed Tango Plus flx930 provide a suitable tensile force and fatigue limit to be used as a flexure hinge. The fabrication of the hinge using soft and hard material shows many issues in the transformation lines when it is printed. The continues pad of Tango Plus flx930 under Vero's faces reduce the failure. And prevent the cracks and gaps from appearing in the transformation line. Furthermore, putting an overlap printing limit reduce the gaps in the transformation line.

The laminate layer approach could be used to build a flexure hinge when used acrylic and Kapton material. The tensile and fatigue limit of Kapton is higher than the Tango Plus, but the stiffness is lower.

The actuation system is the third aspect that should study when fabrication of folding robots. The external actuation system is suitable for folding structure for manipulation, but it can become very complicated when used in a self-folding robot. The use of 3D printed chain for force transmission does not succeed. The designed Vero chain provide high flexibility but low tensile strength. Furthermore, the action system of self-folding structure used the embedded smart material actuators the BSW, and TSW actuators provide the same bend force for the equal diameters. The forces that are supplied by BSW and TSW actuators could not operate a reverse folding process.

The self-folding origami cube has been printed using Tango Plus and Vero material. The cube shows a smoothly folding process, but it is still slow because the embedded BSW actuators required a long time for activation under uniform heating. The OSM-Bot provide high manipulation ability. And the four servo motor actuators give high response movement and more occurrent position. Furthermore, The low bending stiffness makes OSM-Bot reach to all most 180^{o} bend angle.

7.3 Future work

This research has provided a starting point for research into the fabrication of origami folding robots. It is required long development to reach an origami self-folding and high manipulation robot that could carry out tasks. All design and fabrication aspects that are mentioned in the 7.2 section are required to have more work and development.

The origami structures require more investigation to create other types of origami structure. The researchers can compare between two or more unit cells of different kinds of origami to create a structure that has all the features of these unit cells.

The use of the 3D printer approach requires the investigation of more materials. Furthermore, the multi-material technique requires to develop by using a new type of design or adding third material to reduce the ability of failure on the transformation line. The option of embedding the actuators during the 3D printed process should be investigated.

The self-folding structure required faster actuators than the SMW or SMP. New types of smart materials can be used to reach high response folding. The OSM-Bot required more improvements such as the strength of structure and accuracy of movement. The essential improving that is required is the task operation. Furthermore, other material should be used to fabricate OSM-Bot to make it have higher stiffness. The acrylic-Kapton model of OSM-Bot required to test many types of mechanisms that provide stiffness to the structure. Change its design to reach a high axial stiffness with low bend stiffness structure.

The new type of printed chain or string can be developed to fabricate a print to go type of OSM-Bot. The 3D printed OSM-Bot can be studied and obtain a new structure that could be print with their force transmission tools. The reaching to print to go version of OSM-Bot could lead to huge progress in the origami folding robot fields and 3D printing fabrication approach.

Future work is required to control the OSM-Bot arm so that a given end-effector position can be obtained with what precision and repeatability. Initially, the forward kinematics of the robot could be investigated to determine string length to obtain a given end -effector position. Investigate transmission system that can be 3D printed at a hinge with a local motor placed at each hinge.

List of References

[1] A. Wolf *et al.*, ‘A mobile hyper redundant mechanism for search and rescue tasks’, *Proc. 2003 IEEE/RSJ Int. Conf. Intell. Robot. Syst. (IROS 2003) (Cat. No.03CH37453)*, vol. 3, pp. 2889–2895, 2003.

[2] J. Davey, J. Sastra, M. Piccoli, and M. Yim, ‘ModLock: A manual connector for reconfigurable modular robots’, *IEEE Int. Conf. Intell. Robot. Syst.*, pp. 3217–3222, 2012.

[3] C. D. Onal, R. J. Wood, and D. Rus, ‘An origami-inspired approach to worm robots’, *IEEE/ASME Trans. Mechatronics*, vol. 18, no. 2, pp. 430–438, 2013.

[4] S. Felton, M. Tolley, E. Demaine, D. Rus, and R. Wood, ‘A method for building self-folding machines’, *Science (80-.).*, vol. 345, no. 6197, pp. 644–646, 2014.

[5] L. Mahadevan and S. Rica, ‘Self-organized origami’, *Science (80-.).*, 2005.

[6] K. Saito, A. Tsukahara, and Y. Okabe, ‘Designing of self-deploying origami structures using geometrically misaligned crease patterns’, *Proc. R. Soc. A Math. Phys. Eng. Sci.*, vol. 472, no. 2185, 2016.

[7] C. M. Dobson, ‘Protein folding and misfolding’, *Nature*. 2003.

[8] J. H. Na *et al.*, ‘Programming reversibly self-folding origami with micropatterned photo-crosslinkable polymer trilayers’, *Adv. Mater.*, vol. 27, no. 1, pp. 79–85, 2015.

[9] J. Casper and R. R. Murphy, ‘Human-robot interactions during the robot-assisted urban search and rescue response at the World Trade Center’, *IEEE Trans. Syst. Man, Cybern. Part B Cybern.*, vol. 33, no. 3, pp. 367–385, 2003.

[10] B. Shah and H. Choset, ‘Survey on Urban Search and Rescue Robots’, *J. Robot. Soc. Japan*, vol. 22, no. 5, pp. 582–586, 2004.

[11] Z. Wang, W. Zhelong, and Z. Wang, ‘Design study of an earthquake rescue robot’, 2004.

[12] B. M. Yamauchi, ‘PackBot: a versatile platform for military robotics’, *Def. Secur.*, pp. 228–237, 2004.

[13] W. Schoor, M. Förster, and A. Radetzky, ‘Realistic training simulations of explosive ordnance disposal & improvised explosive device disposal robots’, *IEEE Int. Conf. Ind. Informatics*, vol. 49, no. 0, pp. 875–880, 2012.

[14] S. A. A. Moosavian, H. Semsarilar, and A. Kalantari, ‘Design and manufacturing of a mobile rescue robot’, *IEEE Int. Conf. Intell. Robot. Syst.*, no. NOVEMBER, pp. 3982–3987, 2006.

[15] S. Murata, E. Yoshida, A. Kamimura, H. Kurokawa, K. Tomita, and S. Kokaji, ‘M-TRAN : Self-Reconfigurable Modular’, vol. 7, no. 4, pp. 431–441, 2002.

[16] A. Castano, A. Behar, and P. M. Will, ‘The Conro modules for reconfigurable robots’, *IEEE/ASME Trans. Mechatronics*, vol. 7, no. 4, pp. 403–409, 2002.

[17] M. W. Jorgensen, E. H. Ostergaard, and H. H. Lund, ‘Modular ATRON: modules for a self-reconfigurable robot’, *2004 IEEE/RSJ Int. Conf. Intell. Robot. Syst. (IEEE Cat. No.04CH37566)*, vol. 2, pp. 2068–2073, 2004.

[18] E. H. Østergaard, K. Kassow, R. Beck, and H. H. Lund, ‘Design of the ATRON lattice-based self-reconfigurable robot’, *Auton. Robots*, vol. 21, no. 2, pp. 165–183, 2006.

[19] M. Yim, D. G. Duff, and K. D. Roufas, ‘PolyBot: a modular reconfigurable robot’, *Proc. 2000 ICRA. Millenn. Conf. IEEE Int. Conf. Robot. Autom. Symp. Proc. (Cat. No.00CH37065)*, vol. 1, no. April, pp. 514–520, 2000.

[20] H. Kurokawa, K. Tomita, A. Kamimura, S. Kokaji, T. Hasuo, and S. Murata, ‘Distributed self-reconfiguration of M-TRAN III modular robotic system’, *Int. J. Rob. Res.*, vol. 27, no. 3–4, pp. 373–386, 2008.

[21] B. Salemi, M. Moll, W. Shen, and M. Rey, ‘SUPERBOT : A Deployable , Multi-Functional , and Modular Self-Reconfigurable Robotic System’, pp. 3636–3641, 2006.

[22] J. Zhao, X. Cui, Y. Zhu, and S. Tang, ‘A new self-reconfigurable modular robotic system UBot: Multi-mode locomotion and Self-reconfiguration’, *Proc. - IEEE Int. Conf. Robot. Autom.*, vol. 150080, no. 2, pp. 1020–1025, 2011.

[23] F. Hou and W. M. Shen, ‘Graph-based optimal reconfiguration planning for self-reconfigurable robots’, *Rob. Auton. Syst.*, vol. 62, no. 7, pp. 1047–1059, 2014.

[24] C. Wright *et al.*, ‘Design of a modular snake robot’, *IEEE Int. Conf. Intell. Robot. Syst.*, pp. 2609–2614, 2007.

[25] C. Wright *et al.*, ‘Design and Architecture of the Unified Modular Snake Robot’, *IEEE Int. Conf. Robot. Autom.*, pp. 4347–4354, 2012.

[26] K. Suzuki, A. Nakano, G. Endo, and S. Hirose, ‘Development of multi-wheeled snake-like rescue robots with active elastic trunk’, *IEEE Int. Conf. Intell. Robot. Syst.*, pp. 4602–4607, 2012.

[27] L. Pfotzer, S. Ruehl, G. Heppner, A. Roennau, and R. Dillmann, ‘KAIRO 3: A modular reconfigurable robot for search and rescue field missions’, *2014 IEEE Int. Conf. Robot. Biomimetics, IEEE ROBIO 2014*, pp. 205–210, 2014.

[28] H. Miyanaka *et al.*, ‘Development of an unit type robot “KOHGA2” with stuck avoidance ability’, *Proc. - IEEE Int. Conf. Robot. Autom.*, no. April, pp. 3877–3882, 2007.

[29] J. Borenstein, M. Hansen, and A. Borrell, ‘The OmniTread OT-4 serpentine robot - Design and performance’, *J. F. Robot.*, 2007.

[30] P. Chavan, M. Murugan, E. V. V. Unnikkannan, A. Singh, and P. Phadatare, ‘Modular snake robot with mapping and navigation: Urban search and rescue (USAR) robot’, *Proc. - 1st Int. Conf. Comput. Commun. Control Autom. ICCUBEA 2015*, pp. 537–541, 2015.

[31] T. Karakurt, A. Durdu, and N. Yilmaz, ‘Design of Six Legged Spider Robot and Evolving Walking Algorithms’, *Int. J. Mach. Learn. Comput.*, vol. 5, no. 2, pp. 96–100, 2015.

[32] K. A. . R.-S. Davies A., ‘A Reconfigurable USAR Robot Designed for Traversing Complex 3D Terrain’, *22nd Can. Congr. Appl. Mech. 2009 (CANCAM 2009)*, no. JUNE 2009, p. 339 (1 Vol), 2009.

[33] M. Rahmani, ‘Search and Rescue using Swarm Robots’, *Submitt. Publ.*, pp. 1–5.

[34] A. Din, M. Jabeen, K. Zia, A. Khalid, and D. K. Saini, ‘Behavior-based swarm robotic search and rescue using fuzzy controller’, *Comput. Electr. Eng.*, vol. 70, pp. 53–65, Aug. 2018.

[35] B. Yang, Y. Ding, Y. Jin, and K. Hao, ‘Self-organized swarm robot for target search and trapping inspired by bacterial chemotaxis’, *Rob. Auton. Syst.*, vol. 72, pp. 83–92, Oct. 2015.

[36] C. K. Pang, A. Kumar, C. H. Goh, and C. V. Le, ‘Nano-satellite swarm for SAR applications: design and robust scheduling’, *IEEE Trans. Aerosp. Electron. Syst.*, vol. 51, no. 2, pp. 853–865, Apr. 2015.

[37] A. S. Kumar, G. Manikutty, R. R. Bhavani, and M. S. Couceiro, ‘Search and rescue operations using robotic darwinian particle swarm optimization’, in *2017 International Conference on Advances in Computing, Communications and Informatics (ICACCI)*, 2017, pp. 1839–1843.

[38] M. Bakhshipour, M. Jabbari Ghadi, and F. Namdari, ‘Swarm robotics search & rescue: A novel artificial intelligence-inspired optimization approach’, *Appl. Soft Comput.*, vol. 57, pp. 708–726, Aug. 2017.

[39] D. B. Camarillo, T. M. Krummel, and J. K. Salisbury, ‘Robotic technology in surgery: Past, present, and future’, *Am. J. Surg.*, 2004.

[40] G. S. Guthart and J. K. Salisbury, ‘The Intuitive/sup TM/ telesurgery system: overview and application’, *Proc. 2000 ICRA. Millenn. Conf. IEEE Int. Conf. Robot. Autom. Symp. Proc. (Cat. No.00CH37065)*, vol. 1, pp. 618–621, 2000.

[41] P. Gomes, ‘Surgical robotics: Reviewing the past, analysing the present, imagining the future’, *Robotics and Computer-Integrated Manufacturing*. 2011.

[42] D.-Y. Lee, J.-S. Kim, S.-R. Kim, J.-J. Park, and K.-J. Cho, ‘Design of deformable-wheeled robot based on origami structure with shape memory alloy coil spring’, *2013 10th Int. Conf. Ubiquitous Robot. Ambient Intell.*, no. 2009, pp. 120–120, 2013.

[43] D. Y. Lee, J. S. Kim, J. J. Park, S. R. Kim, and K. J. Cho, ‘Fabrication of origami wheel using pattern embedded fabric and its application to a

deformable mobile robot', *Proc. - IEEE Int. Conf. Robot. Autom.*, p. 2565, 2014.

[44] E. Vander Hoff, D. Jeong, and K. Lee, 'OrigamiBot-I: A thread-actuated origami robot for manipulation and locomotion', *IEEE Int. Conf. Intell. Robot. Syst.*, no. Iros, pp. 1421–1426, 2014.

[45] K. Zhang and C. Qiu, 'Helical Kiragami-inspired Centimeter-scale Worm Robot with Shape-memory-alloy Actuators', in *2014 ASME International Design Engineering Technical Conferences & Computers & Information in Engineering Conference*, 2014.

[46] M. Agheli, S. G. Faal, F. Chen, H. Gong, and C. D. Onal, 'Design and fabrication of a foldable hexapod robot towards experimental swarm applications', in *Proceedings - IEEE International Conference on Robotics and Automation*, 2014.

[47] A. M. Mehta and D. Rus, 'An end-to-end system for designing mechanical structures for print-and-fold robots', *Proc. - IEEE Int. Conf. Robot. Autom.*, pp. 1460–1465, 2014.

[48] A. Mehta *et al.*, 'A design environment for the rapid specification and fabrication of printable robots', *Springer Tracts Adv. Robot.*, vol. 109, pp. 435–449, 2016.

[49] D. J. Hartl and D. C. Lagoudas, 'Thermomechanical Characterization of Shape Memory Alloy Materials', in *Shape Memory Alloys*, 2008.

[50] J. Koh, S. Kim, and K. Cho, 'Self-Folding Origami Using Torsion Shape Memory Alloy Wire Actuators', *Vol. 5B 38th Mech. Robot. Conf.*, no. April 2016, p. V05BT08A043, 2014.

[51] E. A. Peraza-Hernandez, D. J. Hartl, R. J. Malak, and D. C. Lagoudas, 'Origami-inspired active structures: A synthesis and review', *Smart Mater. Struct.*, vol. 23, no. 9, 2014.

[52] L. Li, Q. Li, and F. Zhang, 'Applications of SMA Bundles in Practical Concrete Structures', in *Shape Memory Alloys - Processing, Characterization and Applications*, 2013.

[53] W. Gao, K. Huo, J. S. Seehra, K. Ramani, and R. J. Cipra, 'HexaMorph: A reconfigurable and foldable hexapod robot inspired by origami', *IEEE Int. Conf. Intell. Robot. Syst.*, no. Iros, pp. 4598–4604, 2014.

[54] J. K. Paik, B. An, D. Rus, and R. J. Wood, 'Robotic origamis: self-morphing modular robots', *Proc. 2nd Int. Conf. Morphol. Comput.*, pp. 29–31, 2011.

[55] E. Hawkes *et al.*, 'Programmable matter by folding', *Proc. Natl. Acad. Sci.*, vol. 107, no. 28, pp. 12441–12445, 2010.

[56] B. An and D. Rus, 'Designing and programming self-folding sheets', *Rob. Auton. Syst.*, vol. 62, no. 7, pp. 976–1001, 2014.

[57] C. D. Onal, R. J. Wood, and D. Rus, 'Towards printable robotics: Origami-inspired planar fabrication of three-dimensional mechanisms', *Proc. - IEEE Int. Conf. Robot. Autom.*, pp. 4608–4613, 2011.

[58] A. Firouzeh, Y. Sun, H. Lee, and J. Paik, ‘Sensor and actuator integrated low-profile robotic origami’, *IEEE Int. Conf. Intell. Robot. Syst.*, pp. 4937–4944, 2013.

[59] A. Firouzeh and J. Paik, ‘Robogami: A Fully Integrated Low-Profile Robotic Origami’, *J. Mech. Robot.*, vol. 7, no. 2, p. 021009, 2015.

[60] M. T. Tolley *et al.*, ‘Self-folding shape memory laminates for automated fabrication’, *IEEE Int. Conf. Intell. Robot. Syst.*, pp. 4931–4936, 2013.

[61] S. Miyashita and D. Rus, ‘Multi-Crease Self-Folding by Uniform Heating Self-Folding Method’, *Ecal 2013*, no. 1, pp. 955–956, 2013.

[62] M. T. Tolley, S. M. Felton, S. Miyashita, D. Aukes, D. Rus, and R. J. Wood, ‘Self-folding origami: Shape memory composites activated by uniform heating’, *Smart Mater. Struct.*, vol. 23, no. 9, 2014.

[63] S. M. Felton, M. T. Tolley, C. D. Onal, D. Rus, and R. J. Wood, ‘Robot self-assembly by folding: A printed inchworm robot’, *Proc. - IEEE Int. Conf. Robot. Autom.*, pp. 277–282, 2013.

[64] S. Miyashita, S. Guitron, M. Ludersdorfer, C. R. Sung, and D. Rus, ‘An untethered miniature origami robot that self-folds, walks, swims, and degrades’, in *2015 IEEE International Conference on Robotics and Automation (ICRA)*, 2015, vol. 2015-June, no. June, pp. 1490–1496.

[65] S. Miyashita, S. Guitron, S. Li, and D. Rus, ‘Robotic metamorphosis by origami exoskeletons’, *Sci. Robot.*, vol. 2, no. 10, p. eaao4369, Sep. 2017.

[66] A. Kasem, F. Ghourabi, and T. Ida, ‘Origami axioms and circle extension’, 2011.

[67] R. J. Lang, ‘Huzita-justin axioms’. 2004.

[68] R. Alperin, ‘One-, Two- and Multi-Fold Origami Axioms’, in *Origami 4*, 2011.

[69] C. Lv, D. Krishnaraju, G. Konjevod, H. Yu, and H. Jiang, ‘Origami based mechanical metamaterials’, *Sci. Rep.*, vol. 4, 2014.

[70] M. Schenk and S. D. Guest, ‘Geometry of Miura-folded metamaterials’, *Proc. Natl. Acad. Sci.*, vol. 110, no. 9, pp. 3276–3281, 2013.

[71] Y. Wang and K. Lee, ‘3D-printed semi-soft mechanisms inspired by origami twisted tower’, *2017 NASA/ESA Conf. Adapt. Hardw. Syst. AHS 2017*, no. October, pp. 161–166, 2017.

[72] P. Badagavi, V. Pai, and A. Chinta, ‘Use of Origami in Space Science and various other fields of science’, in *2017 2nd IEEE International Conference on Recent Trends in Electronics, Information & Communication Technology (RTEICT)*, 2017, pp. 628–632.

[73] N. Lobontiu, J. S. N. Paine, E. Garcia, and M. Goldfarb, ‘Corner-Filleted Flexure Hinges’, *J. Mech. Des.*, vol. 123, no. 3, p. 346, 2001.

[74] C. A. Ugural, *Mechanics of materials*. John Wiley & Sons, Inc., 2008.

[75] ‘No Title’. [Online]. Available: http://www.stratasys.com.

[76] J. T. Bauman, ‘Fatigue, stress, and strain of rubber components: a guide for design engineers’, p. 214, 2008.

[77] ‘www.dupont.com’.

[78] A. Long, M. Lyon, and G. Lyon, ‘Industrial rope access - Investigation into items of personal protective equipment CRR 364/2001’, 2001.

[79] C. Liang and C. A. Rogers, ‘One-Dimensional Thermomechanical Constitutive Relations for Shape Memory Materials’, *J. Intell. Mater. Syst. Struct.*, vol. 1, no. 2, pp. 207–234, 1990.

[80] K. Tanaka, ‘(delaey, krishnan’, vol. 2, pp. 59–72, 1986.

[81] S. An, J. Ryu, M. Cho, and K. Cho, ‘Engineering design framework for a shape memory alloy coil spring actuator using a static two-state model’, vol. 055009, 2012.

[82] ‘http://www.singletact.com/’.

Appendix A

Paper published

This section contains published work from this thesis:

Abtan, A. A., Richardson, R. C., & Thomas, B. (2016, October). Analyzing the 3D printed material Tango plus FLX930 for using in self-folding structure. In 2016 International Conference for Students on Applied Engineering (ICSAE) (pp. 114-118). IEEE.

Analyzing the 3D Printed Material Tango Plus FLX930 for Using in Self-Folding Structure

Akeel A. Abtan
E-mail:
mnaaabt@leeds.ac.uk

Robert C. Richardson
E-mail:
R.C.Richardson@leeds.ac.uk

Briony Thomas
E-mail:
B.G.Thomas@leeds.ac.uk

School of Mechanical Engineering
University of Leeds
Leeds, UK.

***Abstract*— Self-folding is the ability of the structure to fold and/or unfold without human intervention or any application of external manipulation. It is known that the structure of folding object consists of two essential parts. These parts are the faces and the creases.**

In this paper, it is assumed that the faces could be built by using solid materials, and the crease lines can be built using soft material which provides a high bent ability. Furthermore, these two materials should be combined built without using any connections between them. Fortunately, the 3D printer provides this capability. It can print two types of different materials at the same time for the same structure. Therefore, a 3D printer is chosen to fabricate a folding structure using two types of material. These types are the Vero for solid faces and Tango plus FLX930 for the soft creases lines. The soft material at hinge part (creases lines) subjected to the load directly when the structure folds. It should have a clear view of the mechanical properties of this material. Therefore, several mechanical tests for Tango FLX930 material are operated to calculate its mechanical properties and find the force that required to fold it.

Keywords*— *Self-Folding Structure; 3D printer; Tango Plus.

I. Introduction

The self-folding structure gives the opportunity to manufacture many types of robots as a plane sheet. This sheet can fold itself during the task operation. The folding robots are inspired from the "origami" which is the Japanese's word that means the art of folding papers. In the last few years, some researchers consider the origami robots and self-folding sheet to be potential solutions for the applications that require a morphing structure [1], [2]. The ambition of these researchers is to reach the design of robot with a high degree of freedom which is simple manufacturing and inexpensive. In addition, it can be self-folding, and self-assembly and it can be used to operate a minimally invasion task in surgery or search and rescue mission because it is folded from a 2D sheet into a 3D structure.

However, there are no real applications of folding robots in search and rescue field except the two papers by Lee that present a prototype of rescue robots using origami wheels. Lee designed two robots with deformable wheels using the origami magic ball pattern to fabricate the wheels [3],[4]. The two robots using a folding structure to fabricate a simple part of the robot, but the unique characteristics of folding open the future to many unexpected designs that can be adopted in many robotic fields.

The two major categories of folding material depending on the folding process which are the manual folding and self-folding robots. These two categories depend on the same steps to fabricate the folding robots which are: (1) planner and design the pattern, (2) select materials and fabrication procedure, and (3) choose the actuators that operate the motion or locomotion in manual folding robots or operate the self-folding and locomotion in the self-folding robots. The researchers focus on how to fabricate simple,

cheap and fast fabrication robots by using a folding approach. While in self-folding, the researchers focus on morphing the 2D sheet into 3D structure at the operation task or how can build reconfiguration robots by using folding approach.

Some researchers build a printable robot using paper and folding it manually [5], [6]. Other researchers developed a self-folding hinges by using multilayer laminate which consist of shape memory polymer SMP, paper or plastic sheet, and resistive circuits [7]. They used an outer layer of SMP from two sides. This self-folding technique shows the capability of creating complex geometries. They fabricated a printed inchworm robot [8] by using this self-folding approach. Recently, they developed a crawling robot that folds itself by using five layers. These layers are two outer SMP layers, two paper layers and the middle layer of the copper-polyimide [2].

This paper focuses on the material that could build a folding structure. It is assumed that the folding structure could be easily fabricated using the 3D printer. The 3D printer can print a sheet with solid faces and soft material for the hinges. Therefore, it is chosen the Vero material to be the solid faces and Tango Plus FLX930 to be the soft material. For that reason, the Tango Plus FLX930 should be analyzed to calculate its mechanical behavior such as tensile, bending, and fatigue.

II. Origami and Folding Structure

All folding structures are inspired from origami which is the art of paper folding. The essential difference is that the folding structure could be made from any material, while the paper is the major material for origami structure. However, all the structural design of any folder structure can be obtained by using the principals of origami design pattern.

The creases are the singularity part in folding structure and should build from soft material. The *creases* are the locations of localized folds of the sheet. Every crease can be folded either convex (*mountain*) or concave (*valley*). The *vertices* are the endpoints of the crease lines. The *faces* are the closed areas that bounded by the creases and it should be built from hard material. All the creases with its mountain and valley assignments make up the *crease pattern*. These concepts are shown in Fig. 1. The Vero is chosen for solid faces and Tango plus FLX930 is chosen for the soft creases lines to fabricate the folding structure using 3D printer.

The Tessellation origami is the appropriate type of origami shape to produce the folding robot because this type has a high flexibility and can be reconfigurable after folding. These two properties are very important to the functionality of robots. Furthermore, the crease patterns of this type consist a similar element that can repeat forever to form structures on any scale. This property makes it easy to put actuation procedure for one element and repeat it for all other elements. The best examples of Tessellation origami are origami magic ball. The major features which provide by this design is that, the magic ball can contract and expand in all directions See Fig. 2.

One element of magic ball structure was printed by using 3D printer see Fig. 3. The element has a square shape with 20 mm length and 1mm thickness. The creases lines have width of 2mm which are made from Tango Plus FLX 930. The strain in the creases is analyzed before these dimensions are chosen.

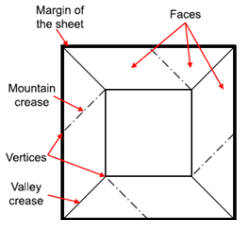

Fig. 1. Crease pattern illustrating various origami concepts.

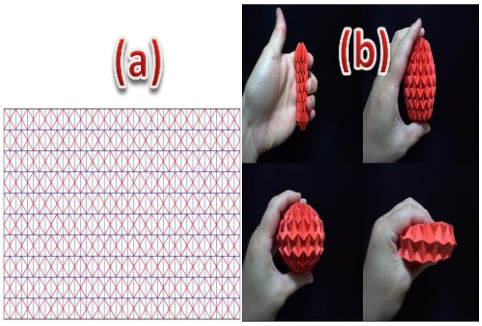

Fig. 2. (a) Crease patterns of Magic Ball, (b) Origami Magic Ball after folding [9].

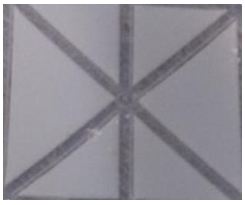

Fig. 3. One element from the magic ball pattern Manufacturing by 3D printer

III. Strain in the creases

All the deformation for any origami structures occurs on the crease line. Whatever it is a mountain or valley crease. We should have a clear description of this area to achieve a correct design. When the crease line is analyzed for any

material (not just paper), it should be assumed that the crease line work as a hinge connected other solid material. This hinge has two effective dimensions which are the width b and the thickness t. Every crease has a radius of curvature R and folding angle θi when it is bent. From these parameters, the strain ε at any point on the edge can be calculated as:

$$\varepsilon = \frac{\Delta l}{l} = \frac{r\theta_i - b}{b} \qquad (1)$$

Where r is the variable radius and its value: ($R \leq r \leq R + t$) and l is the length.

By assuming that the maximum fold occurs when the two inner sides of a hinge attached, see Fig. 4. In this special case, the radius assumed to be equal to the thickness and the maximum strain on the outer surface of the hinge can be calculated as:

$$\varepsilon_{max} = \frac{t \times \pi}{b} \qquad (2)$$

It can be seen from equation (2) that the maximum strain on the creases tip directly proportional to the thickness and inversely proportional to the width. For example, if there is a square hinge (i.e. b=t) the maximum strain is π. Therefore, the mechanical tests should be operated for the Tango Plus FLX930 material to ensure that the maximum strain does not exceed by tension, bending and fatigue.

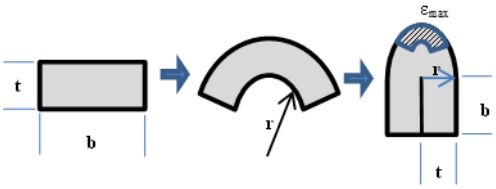

Fig. 4. Simple sketch of a hinge with width b, and thickness t. Starting from flat shape until it is completely fold.

IV. Mechanical Tests and Results

Mechanical properties can demonstrate the behavior of the materials and give the answer of the question for using this material for fabrication crease lines in folding robots or not. Our case requires several mechanical tests such as tensile test, bending test and fatigue test for the Tango Plus flx930 material. These three tests can show the results for the tensile strength limit, fatigue limit and the forces require to fold different thickness sheets into many folding angles.

A. Tensile Test

Although, the tensile test is a traditional mechanical test and there are many standards which show the modulus of elasticity and the tensile strength of different materials, there is lack information about tensile strength for elastomer materials especially for the materials using 3D printer.

Moreover, it is very hard to calculate the modulus of elasticity for elastomer materials analytically, because of many issues such as large deformation response, and non-linearity of the stress-strain curve [10]. Therefore, every new elastomer material should have a particular tensile test to indicate their properties. Although, some elastomer properties depend on time due to the hysteresis effect, this test can give us suitable induction for these properties.

The tensile test was operated three times for three specimens which have the same shape. The specimen has a cylindrical shape with effective length and area (37.7mm, 39.92 mm2) respectively. All specimens were printed on an Object-1000 3D printer in "digital material" mode. The final specimen shape can be seen in the Fig. 5.

The test velocity was set at 60 mm/min. After that, the test was operated which took almost two minutes for every specimen. The stress-strain curve can be calculated from the data of load-displacement which was collected from the tensile test machine. It can be determined by using traditional equations of stress σ and strain which are:

$$\sigma = \frac{F}{A_e} \qquad (3)$$

$$\varepsilon = \frac{\Delta L}{L_e} \qquad (4)$$

Where, A_e and L_e are the effective area and length.

The stress-strain curve can be seen in the Fig. 6. This figure shows the stress-strain curve for the three specimens, and it is clear that the tensile strength of the first specimen equal to 0.68 Mpa and the maximum elongation is 260%. For all specimens, the tensile strength range is between 0.63-0.68 Mpa and the maximum elongation range is between 250-260% and that is nearly the standard that given for this material.

Fig. 5. The tensile test specimen made from Tango Plus flx930.

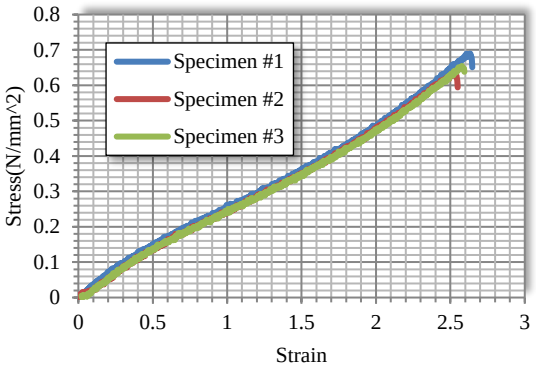

Fig. 6. The stress-strain curve for Tango Plus flx930.

B. Bending Test

The important useful information, which is required from the material behavior, is the amount of force that could fold the sheet made from this material. Therefore, this test can find the amount of force which required folding different thickness beams into a range of folding angles.

Flat specimens are used for this test which have a beam shape. The dimensions of these specimens are 40mm length and 10mm width with three different thicknesses which are 3mm, 5mm, and 7mm. In addition, two types of specimens are used for the 5mm thickness; the first one is completely flat, and the other one has a notch on both sides in the middle with 1mm radius, see Fig. 7. The reason for using these specimens is to find the relation between the thickness and the folding force. Furthermore, these specimens can show the effect of the notch on the folding force. The machine, which was used for this test, is the tensile machine with the graspers of three-point bending test. These graspers used to calculate the material resistant to bending damage. We change the middle rod of this grasper, which is 6mm thick, with the smaller wire, which is 1mm in diameter, to make the folding angle sharp and to reach a smaller radius of curvature for the folding specimen. The test machine requires the speed of test and the final displacement to stop. For our situation, we used the speed of test 60 mm/min and the final displacement 20mm.

When the folding angles are calculated, it is found that there are drooping in load after the angles 105°, 120°, 125° and 135° for the thickness 3mm, 5mm with a notch, 5mm and 7mm respectively. This drooping in load due to the slipping of specimens from grasper rod sides when reaching these angles.

Therefore, the relationship between the folding angles and loads is drawn as it is seen in the Fig. 8, and canceled the slipping zone.

It can be seen from the Fig. 8 that the load increase when the thickness increase, but in the same behavior and that is clear from the slopes of the curves. Furthermore, it can be seen that the result for the specimen 3 (5mm thickness with notch) does not decrease the load a lot. Although, it has a 3mm thickness between the notches, its load does not reach the load of specimen 1 (3mm thickness).

C. Fatigue test

The fatigue life limited is very active parameter when the material is used in an operation that have a dynamic load. In origami structure, the material in the hinge subjected to repeated load which is produced by folding and unfolding process. Therefore, the fatigue limit for the Tango Plus FLX930 should be calculated by using the fatigue test. Especially, when there is lack information for the fatigue life of the 3D printed materials. The fatigue test was operated for three specimens with three different elongation magnitude (30%, 60% and 100%). The specimens were designed according to the ASTM standard ASTM D4482-11, 2011. The final specimen shape that printed on an object-1000 3D printer can be seen in the Fig. 9.

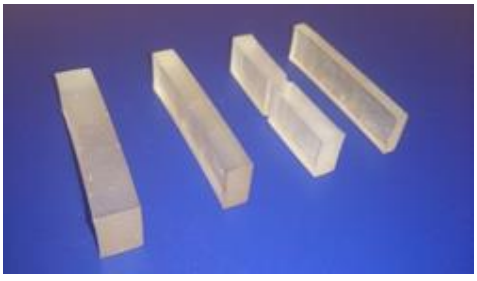

Fig. 7. The bending test specimens made from Tango Plus flx930.

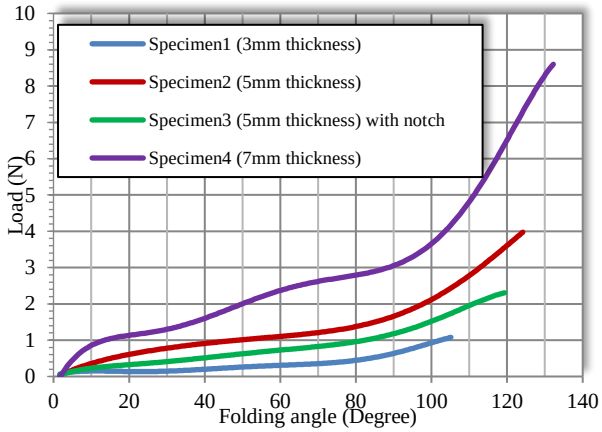

Fig. 8. The folding angles -loads curves for different thickness specimens.

Fig. 9. The fatigue test specimen made from Tango Plus flx930.

The test was operated three times for three specimens with different elongation (i.e., the elongation is the maximum extension input to the machine). The loading and relaxation cycle was taken from the ASTM standard. This standard specified a testing frequency of 1.7 Hz. The results taken from fatigue machine are (6992 cycles, 3640 cycles and 1861 cycles) for the strains (0.32, 0.6, and 1) respectively. From these results it can obtain the equation of fatigue life:

$$N = \left(\frac{\varepsilon_a}{\varepsilon_o}\right)^k \qquad (5)$$

Where N is the fatigue life in a number of cycles, ε_a is the actual strain and ε_o & k are the constants of the equation. In our case, we can calculate the constants as (ε_o=732 and k= -1.14). Therefore, the equation of fatigue life for the Tango Plus FLX930 will be:

$$N = \left(\frac{\varepsilon_a}{732}\right)^{-1.14} \qquad (6)$$

Furthermore, it can obtain the ε-N curve from the results which represent the strain vs fatigue life for the Tango Plus FLX930. See Fig. 10.

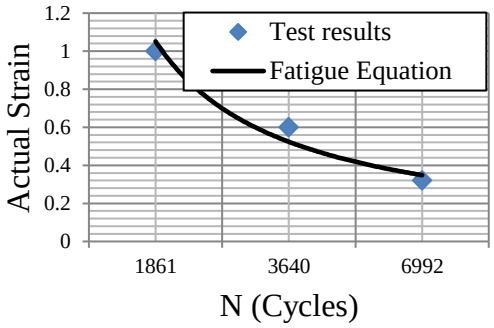

Fig. 10. ε-N curve for the Tango Plus FLX930.

V. Conclusions

In this paper, it is assumed that the folding structure can be printed on the 3D printer using the Vero material for surfaces and Tango Plus FLX930 for the hinges. The strain and stress can be determined in these hinges by assuming them as a beam and using mechanical principles equations. However, the mechanical properties of the material at that hinge must be calculated by mechanical tests.

The mechanical tests for Tango plus improve that this material can be used as a hinge for the folding structure. Furthermore, it has a high range of elongations that can give the folding structure more flexibility. The fatigue limit is calculated, and it is shown that this material can be used in high dynamic load with the strain limit 0.226. In addition, the bending test gives the data that could used to calculate the force required for folding this material into different folding angles.

References

[1] Onal, C.D., Wood, R.J. and Rus, D. "An origami-inspired approach to worm robots". Mechatronics, IEEE/ASME Transactions on. 2013, vol. 18, No. 2, pp.430-438.

[2] Felton, S., Tolley, M., Demaine, E., Rus, D. and Wood, R. "A method for building self-folding machines". Science. 2014, vol. 345, No. 6197, pp.644-646.

[3] Lee, D.-Y., Kim, J.-S., Kim, S.-R., Park, J.-J. and Cho, K.-J. "Design of deformable-wheeled robot based on origami structure with shape memory alloy coil spring". In: Ubiquitous Robots and Ambient Intelligence (URAI), 2013 10th International Conference on: IEEE, 2013, pp.120-120.

[4] Lee, D.-Y., Kim, J.-S., Park, J.-J., Kim, S.-R. and Cho, K.-J. "Fabrication of origami wheel using pattern embedded fabric and its application to a deformable

mobile robot". In: Robotics and Automation (ICRA), 2014 IEEE International Conference on: IEEE, 2014, pp.2565-2565.

[5] Hoff, E.V., Jeong, D. and Lee, K. OrigamiBot-I: "A thread-actuated origami robot for manipulation and locomotion". In: Intelligent Robots and Systems (IROS 2014), 2014 IEEE/RSJ International Conference on: IEEE, 2014, pp.1421-1426.

[6] Zhang, K., Qiu, C. and Dai, J.S." Helical Kirigami-Inspired Centimeter-Scale Worm Robot With Shape-Memory-Alloy Actuators". In: ASME 2014 International Design Engineering Technical Conferences and Computers and Information in Engineering Conference: American Society of Mechanical Engineers, 2014, pp.V05BT08A039-V005BT008A039.

[7] Felton, S.M., Tolley, M.T., Onal, C.D., Rus, D. and Wood, R.J. "Robot self-assembly by folding: A printed inchworm robot". In: Robotics and Automation (ICRA), 2013 IEEE International Conference on: IEEE, 2013, pp.277-282.

[8] Felton, S.M., Tolley, M.T., Shin, B., Onal, C.D., Demaine, E.D., Rus, D. and Wood, R.J. "Self-folding with shape memory composites". Soft Matter. 2013, vol. 9, No. 32, pp.7688-7694.

[9] https://www.flickr.com/photos/26201012@N02/5411813561

[10] Judson, T.B. "Rubber Stress-Strain Behavior. In: Fatigue, Stress, and Strain of Rubber Components". Carl Hanser Verlag GmbH & Co. KG, 2008, pp.9-18